2021

The Rational Synthesis of Lanthanum Manganite Nanomaterials for Magnetic Refrigeration Applications

Caitlin Hunt
Virginia Commonwealth University

The Rational Synthesis of Lanthanum Manganite Nanomaterials for Magnetic Refrigeration Applications

A dissertation submitted in partial fulfillment of the requirements for the degree of Doctor of Philosophy at Virginia Commonwealth University.

By

Caitlin Sierra Marie Hunt

B.S., Boise State University, 2017

Director: Everett E. Carpenter,

Professor of Chemistry

Virginia Commonwealth University

Richmond, Virginia

May 2021

Acknowledgements

This work would not have been possible without the help and support of a multitude of people. Endless appreciation goes to Dr. Carpenter for giving me direction and guidance throughout this project. He has helped me to not only complete this work but also learn to be a competent and confident researcher. I am deeply indebted to Dr. Barua her mentorship and guidance, along with the rest of my committee and the VCU Chemistry Department.

This work and my growth as a person have only been possible through the unconditional love and support of many individuals. My mother deserves more gratitude than I could ever hope to express for nurturing my love for learning over my entire life, modeling how to be a lifelong learner, and most importantly, demonstrating what it means to be a woman of character. Each of my seven siblings – Kenny, Nicholas, Kimberly, Tyra, Kristen, Christopher, and Riley – have provided endless encouragement, accountability, distraction (both needed and unneeded), and care. I would not be who or where I am without you. Finally, thank you to my friends – especially Meg Thornton, Alex Richards, Jeff Noble, Eve Nicholson, Jess Christian, and Cassie McGill – for being willing to laugh with me (and at me), encourage me, and support me.

To all, your fingerprints cover my life in a beautiful way and for that I offer the sincerest of thanks.

Contents

List of Figures

List of Tables

Abbreviations and Symbols

ΔS	Magnetic Entropy Change
ΔT_{ad}	Adiabatic Temperature Change
ΔT_{FWHM}	Full Width at Half Maximum of ΔS Curve – Working Temperature Range
μH	Applied Magnetic Field
C_p	Magnetic Heat Capacity
CA	Citric Acid
COP	Coefficient of Performance
DSC	Differential Scanning Calorimetry
FC	Field Cooled
H	Magnetic Field
HCFC	Hydrochlorofluorocarbon
ICDD	International Center for Diffraction Data
IEA	International Energy Agency
IR	Infrared Spectroscopy
LA-ICP-MS	Laser Ablation – Inductively Coupled Plasma – Mass Spectrometry
LBMO	Lanthanum Barium Manganese Oxide
LCMO	Lanthanum Calcium Manganese Oxide
LSMO	Lanthanum Strontium Manganese Oxide
M	Magnetic Moment
MCE	Magnetocaloric Effect
M_s	Magnetization Saturation
Oe	Oersted
SEM	Scanning Electron Microscopy
RCP	Relative Cooling Potential
T_b	Blocking Temperature
T_{bif}	Bifurcation temperature of FC and ZFC curves
T_c	Curie Temperature
TEM	Transmission Electron Microscopy
TGA	Thermal Gravimetric Analysis
VCRS	Vapor-Condenser Refrigeration System
VSM	Vibrating Sample Magnetometry
XPS	X-Ray Photoelectron Spectroscopy
XRD	X-Ray Diffraction
ZFC	Zero Field Cooled

Abstract

THE RATIONAL SYNTEHSIS OF LANTHANUM MANGANITE NANOPARTICLES FOR MAGNETIC REFRIGERATION APPLICATIONS

By Caitlin Sierra Marie Hunt

A dissertation submitted in partial fulfillment of the requirements for the degree of Doctor of Philosophy at Virginia Commonwealth University.

Virginia Commonwealth University, 2021

Director: Dr. Everett E. Carpenter

Professor of Chemistry

Refrigeration systems for the cooling of commercial and residential buildings are a major drain on energy resources and source of greenhouse gas emissions. Magnetic refrigeration, which employs the magnetocaloric effect, has the potential to mitigate the energy drain and greenhouse gas emissions for air conditioning. In order to commercialize magnetic refrigerators, a material with a high magnetic entropy change, ΔS, near room temperature which is simple and inexpensive to create is needed.[1] Current options for this solid refrigerant are either expensive, difficult to synthesize, or have a ΔS or T_c (the Curie Temperature, where ΔS is maximized) below room temperature. Lanthanum manganite nanomaterials ($La_xA_{1-x}MnO_3$, where A = Ca^{2+}, Sr^{2+}, Na^{+}, Ba^{2+}, etc) exhibit promise as efficient, inexpensive solid refrigerants.[2]

In lanthanum manganites the magnetocaloric properties arise from the Zener double exchange interactions between the Mn ions across the Mn-O-Mn bond. The magnetic properties, namely T_c and ΔS, can therefore be tuned by altering the ratio of Mn^{3+} to Mn^{4+} and the Mn-O-Mn bond distances and angles through the introduction of various metals at the a-site.[3] By entering the nanoscale, crystallite size effects

also become a point of control for both T_c and ΔS. The purpose of this work was to examine each of these three areas as independently as possible in the $La_{0.60}Ca_{0.40}MnO_3$ material, to optimize the Pechini sol-gel synthesis of these materials, and to apply those findings to $La_{0.75}Ca_{0.25}MO_3$ materials.

The Mn-O-Mn bond distances and angles were altered by introducing a-site cation size disorder through substitution of Sr^{2+} in place of Ca^{2+} in the $La_{0.60}Ca_{0.40-x}Sr_xMnO_3$ crystal lattice. As Sr^{2+} was introduced the lattice parameters increased and crystallite size decreased. The lattice distortion created a 73% decrease in ΔS – from 5.6 J/kgK to 1.5 J/kgK.[4] Any T_c affects were offset by the decreasing crystallite size. By contrast, introducing Na^+ into the lattice in place of Ca^{2+} did not alter the lattice parameters of $La_{0.60}Ca_{0.4-x}Na_xMnO_3$ materials or the resultant crystallite sizes, but did increase the amount of Mn^{4+} and decrease the amount of Mn^{3+}. The T_c values increased dramatically, however, from 265K to 333K, and ΔS saw a 33% decrease from 4.1 J/kgK to 2.8 J/kgK.[5] This implies that Mn-O-Mn bond distances and angles are primarily responsible for ΔS, while Mn oxidation states are primarily responsible for T_c. Work done to optimize the synthesis parameters revealed that larger crystallites are ideal as well as the optimal synthesis parameters to achieve the largest crystallite sizes.[6] These findings were successfully applied to $La_{0.75}Ca_{0.25}MnO_3$ materials and the T_c value was increased from 200K, shown in the literature, to 280K.[7]

Through this work, multiple materials with viable magnetic properties were created. These include $La_{0.60}Ca_{0.28}Na_{0.12}MnO_3$ and both the $La_{0.75}Ca_{0.25}MnO_3$ and $La_{0.60}Ca_{0.40}MnO_3$ materials created with the optimized synthesis method. In addition, the understanding of how affecting the Zener double exchange interactions through both Mn-O-Mn bond distances and angles and the Mn oxidation states changes the magnetic properties of lanthanum manganites was improved. By creating nanoscale LCMO nanomaterials with this new understanding, materials ready for practical testing in prototype magnetic refrigerators can be inexpensively and reliably developed.

1 Introduction

1.1 Overview

Refrigeration systems used in cooling of commercial and residential buildings contribute 700 million metric tons of CO_2 globally every year (~10% of all greenhouse gas emissions) and are responsible for nearly 15% of total energy consumption worldwide; total localized energy consumption in peak areas and times can reach as high as 70%.[8] According to a 2018 report on cooling prepared by the International Energy Agency (IEA), in the hottest regions of the world only ~8% of the 2.8 billion residents currently own AC units. This percentage will increase with their rapidly developing economies, leading to a substantial increase in total energy drain and CO_2 emissions.[9–11] In a 2013 report the IEA stated that in order to have an appreciable impact on the sustainability of commercial and residential cooling, the efficiency of refrigeration systems needs to see at least a 30% increase.[8,10]

The efficiency of a refrigeration system is defined as the ratio between the Coefficient of Performance, COP, for the refrigerator and the COP for the Carnot cycle, which is the theoretical ideal thermodynamic cycle. COP is calculated to be the ratio of the temperature on the cold side of the system, T_{cold}, to the difference in temperature between the hot and cold side, T_{cold}-T_{hot}: $COP = \frac{T_{cold}}{T_{hot} - T_{cold}}$.[12,13] Current air conditioning systems are Vapor-Compression Refrigeration Systems (VCRSs). The evaporator and condenser in VCRSs are energy intensive and inefficient components. Attempts to combat this inefficiency have been made by such means as addition of a fan to move air across the refrigerant and the optimization of the fan's speed,[11] addition of components which reduce the irreversibility of the expansion step,[14] and the

integration of nighttime radiative cooling,[15] photovoltaic cooling, or a combination thereof.[16] Even with such modifications the efficiency is still maximized at only ~45% of the Carnot cycle; the market average efficiency is far lower.[17] In addition to inefficient components, the VCRS requires the use of the environmentally hostile hydrochlorofluorocarbons (HCFCs) as liquid refrigerants. In accordance with the Montreal Protocol imposing a phase-out schedule for HCFCs, all transport, usage and production will be banned by January of 2030, imposing a timeline on the development of an alternative means of cooling.[18]

Rather than refining this energy-intensive and inefficient system and adapting it to function without HCFCs, it can instead be replaced with a solid-state refrigeration system. The first potential solid-state refrigeration system is a thermoelectric system relying on the Peltier effect, wherein thermal energy is absorbed or released as current moves from a low energy state in a p-type semiconductor material to a higher energy state in an n-type semiconductor material at a p-n junction, or vice versa.[19] Dependent on the energy being absorbed or released, which is controlled by the direction of the applied current, the system can be used for either heating or cooling. Although this eliminates the need for the evaporator, condenser, and HCFC, the efficiency of a thermoelectric refrigeration system is even lower than a VCRS. Because the conversion of current to heat in a thermoelectric is only about 5% efficient, a thermoelectric cooling system can only reach about 25% of a vapor-condensor system's efficiency.[19]

1.2 Magnetocaloric Effect

Magnetic refrigeration is the second potential solid-state alternative. In this system, a magnetocaloric material undergoes an adiabatic temperature increase when placed in a

magnetic field and an adiabatic temperature decrease when that field is subsequently removed (**Figure 1.1**).[13,20–23] The temperature increase is a result of lattice vibrations increasing to counter a decrease in magnetic entropy when the magnetic spin states align with the field, and the decrease is the result of a decrease in lattice vibrations when those spin states randomize again. This is known as the magnetocaloric effect (MCE). Whereas vapor-condenser refrigeration systems reach a maximum of 45% of the theoretical ideal thermodynamic cycle, early gadolinium-based magnetic refrigeration systems reached up to 60% of the theoretical limit.[13,21,24]

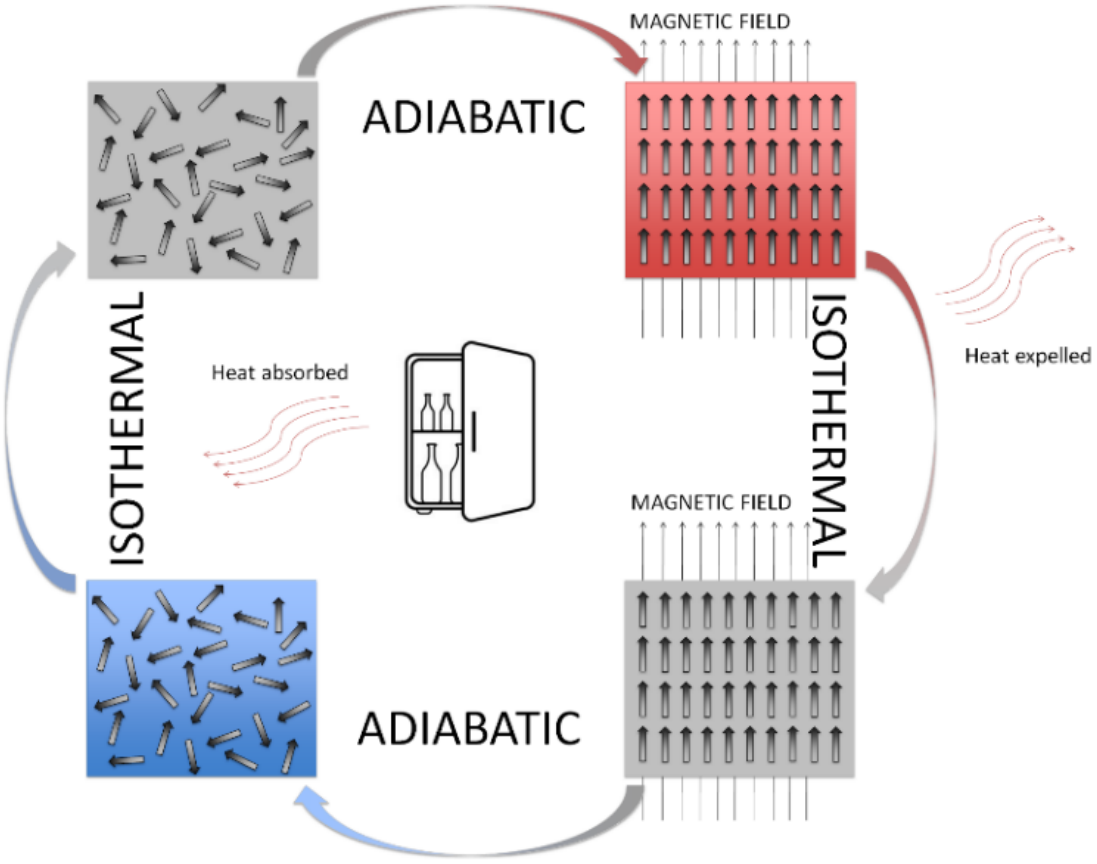

Figure 1.1 *Diagram demonstrating the magnetocaloric effect as it relates to applications in a magnetic refrigeration cycle.*

The adiabatic temperature change observed in a magnetocaloric cycle is dependent on the entropy change instigated by the manipulation of the magnetic field.[24] Although magnetic entropy change cannot be measured directly, it can be determined indirectly through the measurement of the material's thermal response to an applied magnetic field using Maxwell's Relations, as stated in Equation 1:

$$\Delta S_m(\Delta H) = \int_{H_1}^{H_2} \left(\frac{\delta M)}{\delta T}\right)_H dH \quad (1)$$

where M is the measured magnetization, T is temperature, and ΔH is the change in the applied magnetic field (**Figure 1.2**).[22,23] In addition to comparing ΔS_m in discussions of magnetocaloric materials, the Relative Cooling Potential, RCP, of materials is also often compared. RCP is calculated by multiplying the maximum of the MCE curve (the maximum ΔS) by the full width at half maximum (ΔT_{FWHM}), which is a measure of the working temperature range of the material.

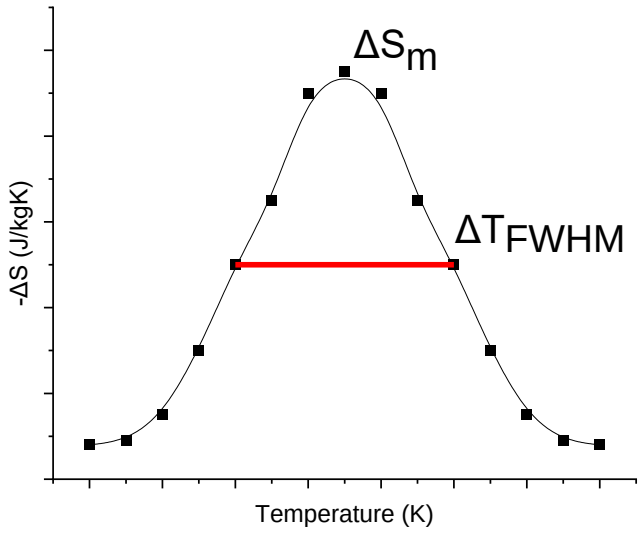

Figure 1.2 *MCE curve showing ΔS_m and the working temperature range, ΔT_{FWHM}.*

ΔS_m can also be determined from the magnetic heat capacity's dependence on the applied field as described by Equation 2:

$$\Delta S_m = \int_0^T \frac{C(T,H) - C(T,0)}{T} dT \quad (2)$$

where C(T, H) is the magnetic heat capacity measured at temperature T and field H.[22,23] The adiabatic temperature change of the material is related to the magnetic heat capacity and the material's thermal response to a magnetic field as shown in Equation 3.[22,23] While this is a more direct measure of a magnetocaloric material's potential for magnetic refrigeration than ΔS or RCP, magnetic heat capacity is a long and involved measurement to obtain so this value is not often used as a point of comparison for magnetocaloric materials.

$$\Delta T_{ad} = -\int_0^H \frac{T}{C_{P,H}} \left(\frac{\partial M}{\partial T}\right)_H dH \quad (3)$$

In order to maximize the adiabatic temperature change, and thus the cooling ability of the magnetocaloric material, the magnetic heat capacity must be minimized and the change in magnetic moment over a given temperature change – $(\delta M/\delta T)_H$ – must be maximized.[25] The Curie Temperature, T_c, of a material is the temperature where a ferromagnetic to paramagnetic magnetic phase transition occurs. When this transition occurs, the magnetic moment drops dramatically. At this temperature, then, $(\delta M/\delta T)_H$ and ΔS are maximized; it is therefore ideal for the T_c of a magnetocaloric material intended for magnetic refrigeration to be close to room temperature.[26,27] T_c, as well as T_b (where the ZFC curve is maximized), and T_{bif} (where the FC and ZFC curves bifurcate) can be determined using an MT curve, where magnetization is plotted as a

function of temperature (**Figure 1.3**). The difference between T_b and T_{bif} is indicative of the distribution of the domain sizes. The more disparate the two values are the larger the range between the smallest and the largest domain sizes.

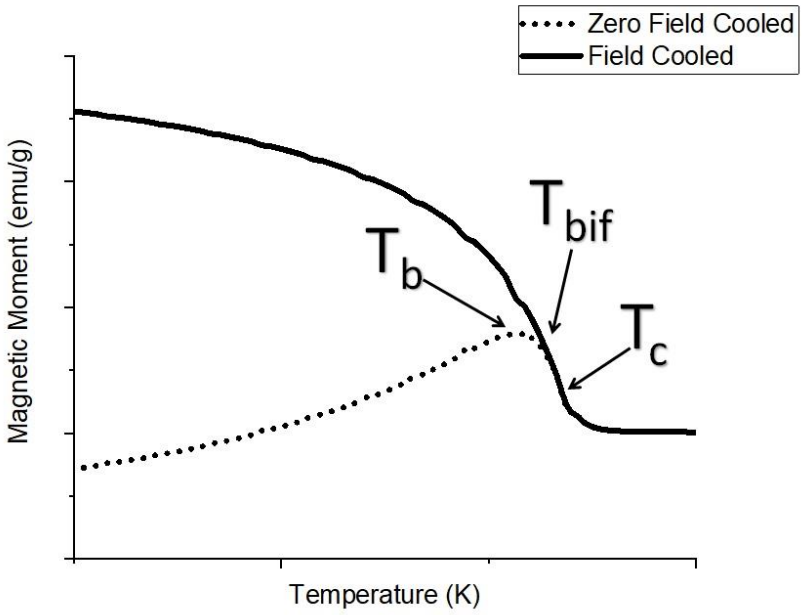

Figure 1.3 *Example Field Cooled and Zero Field Cooled MT curves with the points where T_b, T_{bif}, and T_c are determined labeled. The Zero Field Cooled curve is obtained by cooling the material in the absence of a magnetic field. To obtain the Field Cooled curve a magnetic field is applied (100 Oe in this work) before the material is cooled.*

Above the Curie Temperature the magnetic susceptibility, X, of a material is described by the Curie-Weiss Law (Equation 4). Magnetic susceptibility is a measure of how magnetized a material will become in a given magnetic field. A material which perfectly obeys the Curie-Weiss Law will show a perfectly linear curve above T_c in a plot of $1/\chi$ vs Temperature. A deviation from linear behavior, which appears as a downturn in the $1/\chi$ vs Temperature curve, implies the

presence of a magnetically disordered phase. This magnetically disordered phase is described in more detail in the section on Lanthanum Manganites below.[28]

$$\chi = \frac{C}{T - T_c} \tag{4}$$

It is also worth noting that in magnetic nanomaterials shape of the particles can alter the magnetic properties as a result of magnetic anisotropy.[29,30] The magnetic response of spherical particles, which have a symmetrical or roughly symmetrical shape, should be constant regardless of the orientation of the particles in the magnetic field. Shapes as cubes or irregular shapes, will have a slightly different response dependent on the incident direction of the magnetic field. The axis where more magnetic field is required to elicit a magnetic response is called an easy axis.[30,31] Although powder nanoparticle samples will have random orientations of all particles, averaging out the effect of anisotropy, the overall magnetic properties may be decreased compared to spherical particles where no easy axes exist; magnetic hysteresis also increases with increased anisotropy which negatively impacts applicability in magnetic refrigeration systems.[30]

1.3 Magnetocaloric Materials

An ideal solid refrigerant material in a magnetic refrigeration system would possess a range of attributes (**Figure 1.4**). Intuitively, a material needs to have the largest possible adiabatic temperature change, ΔT, in small magnetic field changes in order to maximize the cooling potential at fields that can be created in a commercialized system. As explained by Equation 3, this is accomplished through maximizing ΔS at a low applied magnetic field (μH) and minimizing C(T, H). The material must also have high thermal conductivity, allowing the heat generated to be passed efficiently between the solid refrigerant material and the heat transport medium.[13,32]

The ideal material would also have little thermal hysteresis in the M(H) curves to maximize reversibility. Because the material will need to undergo repeated hot-cold transitions over the life of the refrigeration system, it must be thermodynamically and chemically stable over the course of the cooling cycle and lifetime of the refrigeration system.[13,22,23,32] In addition, the monetary and environmental cost of sourcing the material's components and creating the material need to be comparable, if not better, than existing refrigeration systems. There are several classes of magnetocaloric materials which have the potential to satisfy these requirements and have shown particular promise as solid refrigerants.

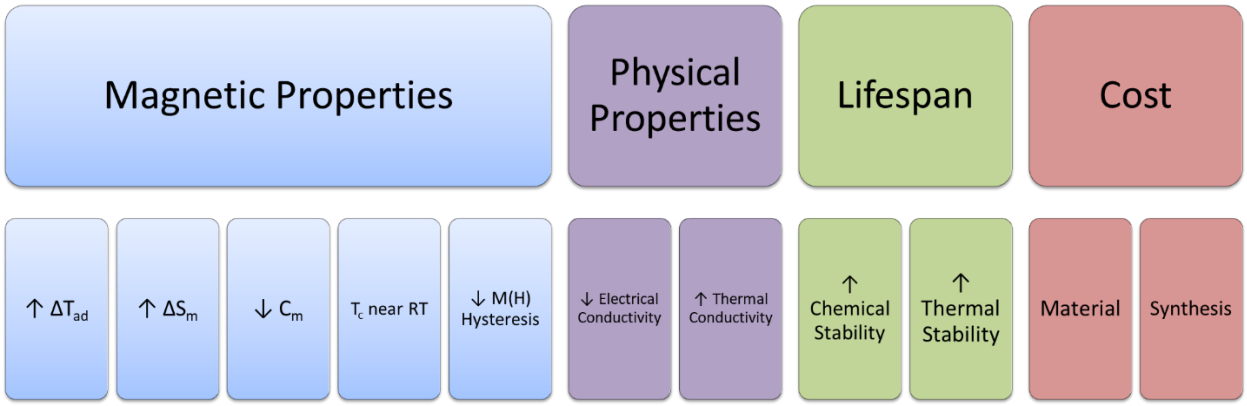

Figure 1.4 *Necessary attributes for an effective magnetocaloric material intended for use in a magnetic refrigerator system.*

1.3.1 Alloy Materials

Paramagnetic salts were first observed to have magnetocaloric properties by Warburg in 1881.[33,34] Using the paramagnetic salts for magnetic refrigeration was first described by Debye and Giauque in 1926, and the first cooling systems were created by Giauque and MacDougall in 1933.[2,33–35] All of this was done at temperatures below 20 K where the paramagnetic salts undergo their phase transition. In the 60's, it was discovered that rare earth elements were

magnetocaloric, with Gd having the largest ΔS near room temperature. Unfortunately, Gd is an expensive material and easily oxidizes,[20,26] making commercialization impractical. Other rare earths, though they have appreciable ΔS values and are slightly less expensive, have T_c values far below room temperature (though still higher than the paramagnetic salts studied initially). Despite their magnetocaloric properties, no rare earth elements are the safe, chemically stable, widely available, and inexpensive material needed to commercialize magnetic refrigeration.[36]

In order to address these problems with using rare earth elements in commercial refrigeration, several materials, such as Ni-Mn-Ga (Heusler) alloys, FeRh alloys, La-Fe-Si materials, and gadolinium silicides, have been explored (**Table 1.1**).[12,13,21,32] These all have appreciable ΔS values and a near room temperature T_c. Heusler alloys are compounds of the formula X_2YZ, where X and Y are transition metals and Z is a p-block element, with face-centered cubic structure. Heusler alloys have been demonstrated to possess maximum ΔS values of up to 144 J/kgK at μH=5T and T_c values tunable to room temperature. Gadolinium silicides of the formula $Gd_5(Si_xGe_{1-x})_4$ have been shown to have maximum ΔS values as high as 40 J/kgK at μH=5 T with T_c values tunable via the ratio of Si to Ge.[26] Bulk FeRh alloys have a body-centered cubic crystal structure, maximum ΔS of up to 9.7 J/kg K at μH=3 T, and a T_c tunable through the Fe to Rh ratio (**Figure 1.5**).[37,38] La-Fe-Si alloys of the formula $La(Fe_xSi_{1-x})_{13}$, with additional dopants taking the place of the Fe or Si in some materials, have maximum ΔS values of up to 12.5 J/kgK at μH=2 T. T_c in these alloys is tunable through varying the amount of hydrogen that has been absorbed to form hydrides.[39–41]

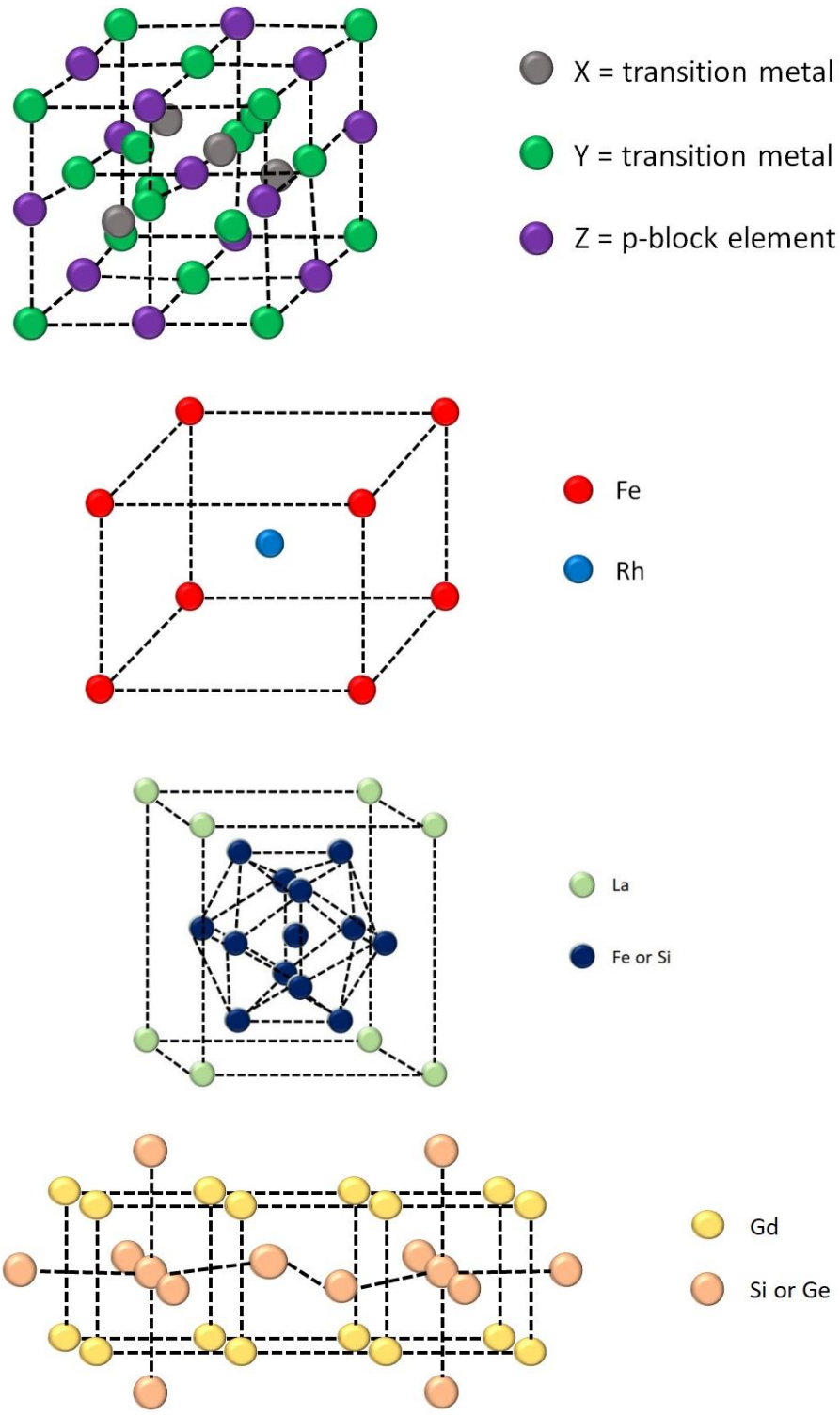

Figure 1.5 *Crystal structures for a variety of magnetocaloric materials.*

Although gadolinium silicides, FeRh, La-Fe-Si, and Heusler alloys demonstrate promising magnetic properties, these materials are generally produced through arc melting, solid phase reduction, or other more complex methods. These methods generally require a high temperature, multiple-day annealing step in an inert atmosphere to ensure a single, unoxidized phase is created.[27,42] Without this long high temperature step the extraneous phases significantly decrease the MCE of the resultant material.[13,42] A material with a simpler and inexpensive synthesis method which could be easily scaled up that doesn't depend on the scarce and expensive gadolinium or rhodium elements is needed in order to increase applicability for commercial use.[20,32]

Table 1.1 *Magnetocaloric materials created via arc melting and their figures of merit.*

Material	**T_c (K)**	**ΔS (J/kgK)**	**μH (T)**	**Ref.**
Gd	295	6.1	2	[43]
$Gd_5Si_{1.72}Ge_{2.28}$	246	40	5	[13]
$Ni_{49.5}Mn_{25.4}Ga_{25.1}$	177	90	1.3	[42]
$Fe_{50}Rh_{50}$	368	9.7	3	[37]
$La(Fe_{0.88}Si_{0.12})_{13}$	203	12.5	2	[39]

1.3.2 Lanthanum Manganites

Another promising group of materials is lanthanum manganites, derived from the perovskite $LaMnO_3$ and of the formula $La_xA_{1-x}MnO_3$ (**Figure 1.6**), which began to garner interest as potential magnetic refrigeration materials in the mid-90's.[44,45] They had previously been studied for their magnetoresistance properties when a sharp drop in magnetic moment at the Curie temperature (large $\Delta M/\Delta T$) suggested potential for a large magnetic entropy change. Initial studies pursuing manganites as an alternative demonstrated wide working temperature ranges, appreciable ΔS values, and tunable T_c values giving manganites promise as magnetic refrigerants.[44,46–48]

In the crystal structure, lanthanum can be substituted at the a-site for a wide range of ions (Ca^{2+}, Sr^{2+}, Ba^{2+}, Na^{+}, K^{+}, etc) in order to affect the magnetic properties of the material (

).[3,13,42,49] These properties arise from Zener double-exchange interactions between the Mn ions across the Mn-O-Mn bond (**Figure 1.7**), where electrons can pass back and forth between Mn e_g orbitals through the O^{2-} 2p orbitals.[50,51] The O^{2-} can pass one of its electrons to the Mn^{4+} orbital without a spin state change. The vacancy can then be filled with the electron in the Mn^{3+} orbital, once again without the spin state changing. This differs from super exchange, wherein no mismatch exists between the two Mn ion oxidation states so the electron must change spin states as it passes across the bond. Though super exchange also leads to a magnetic phase change the transition isn't as sharp and the resulting ΔS value is lower.[45,52,53]

Table 1.2 *Various doped and double-doped manganite materials with their synthesis methods and magnetocaloric figures of merit.*

Material	*Synthesis Method*	*Crystallite Size (nm)*	*T_c (K)*	*ΔS (J/kgK)*	*μH (T)*	*Ref.*
			LCMO			
$La_{0.80}Ca_{0.20}MnO_3$	Sol-gel	NR	230	5.5	1.5	[54]
$La_{0.75}Ca_{0.25}MnO_3$	Sol-gel	300	224	4.7	1.5	[55]
$La_{0.75}Ca_{0.25}MnO_3$	Sol-gel	120	177	2.0	1.5	[55]
$La_{0.67}Ca_{0.33}MnO_3$	Sol-gel	NR	257	4.3	1.5	[54]
$La_{0.55}Ca_{0.45}MnO_3$	Sol-gel	NR	234	2.0	1.5	[54]
$La_{0.60}Ca_{0.40}MnO_3$	Sol-gel	45	258	2.3	5	[56]
$La_{0.60}Ca_{0.40}MnO_3$	Sol-gel	70	269	3.5	5	[56]
$La_{0.60}Ca_{0.40}MnO_3$	Sol-gel	122	272	5.8	5	[56]
$La_{0.60}Ca_{0.40}MnO_3$	Sol-gel	223	270	8.3	5	[56]
			LSMO			
$La_{0.80}Sr_{0.20}MnO_3$	Ceramic	Bulk	305	7.9	7	[3]
$La_{0.75}Sr_{0.25}MnO_3$	Sol-gel	NR	340	1.50	1.5	[57]
$La_{0.67}Sr_{0.33}MnO_3$	Thin Film		348	1.69	5	[58]
			LNMO			
$La_{0.90}Na_{0.10}MnO_3$	Sol-gel	NR	218	1.53	1	[59]
$La_{0.80}Na_{0.20}MnO_3$	Sol-gel	NR	334	1.52	1	[59]
			Double-Doped			
$La_{0.75}Ca_{0.125}Sr_{0.125}MnO_3$	Sol-gel	NR	282	1.5	1.5	[57]
$La_{0.60}Ca_{0.20}Sr_{0.20}MnO_3$	Ceramic		337	1.96	1	[60]
$La_{0.60}Ca_{0.20}Na_{0.20}MnO_3$	Sol-gel		275	2.52	3	[61]

The perovskite has an MnO_6 octahedra which experiences Jahn-Teller distortion, wherein the symmetry and degeneracy of an orbital is broken by the compression or elongation of the bonds in the octahedra in order to decrease the overall energy and stabilize the molecule. As the Mn-O-Mn bond bends, JT distortion is enhanced, and the electronic bandwidth decreased.[62–65] This effects the energy levels of the orbitals involved in Zener double exchange and the subsequent magnetic properties. Due to the lattice distortion, there are three different Mn-O bond distances, referred to hereafter as Mn-O1, Mn-O2 (s), and Mn-O2 (l), and two different Mn-O-Mn bond angles, referred to as Mn-O1-Mn and Mn-O2-Mn.

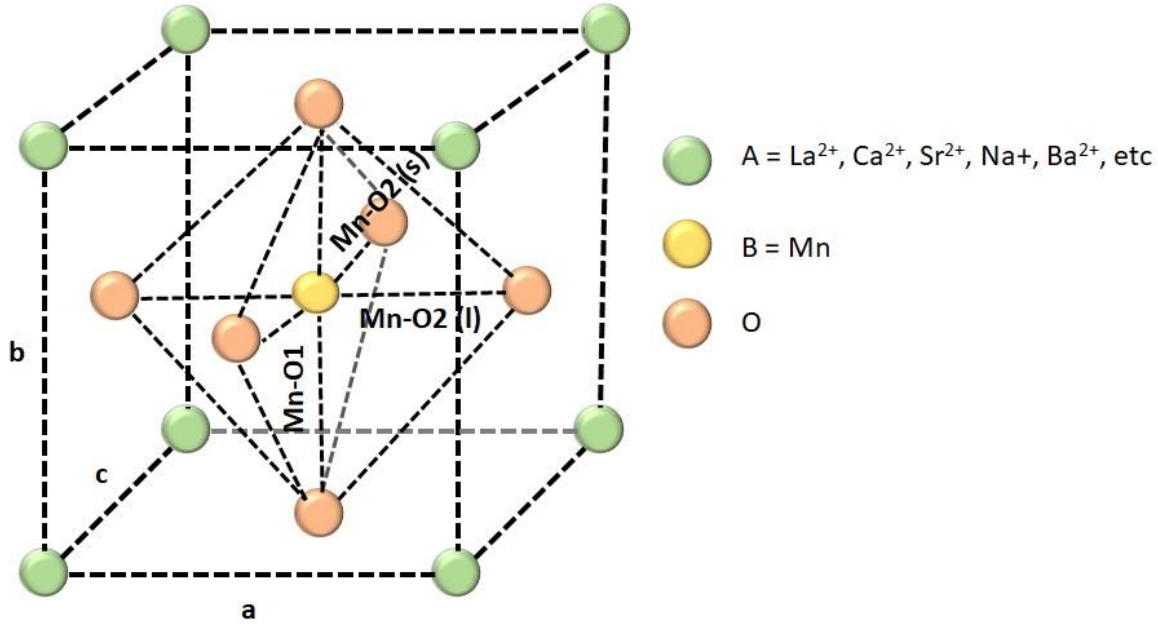

Figure 1.6 *A_xMnO_3 perovskite unit cell with lattice parameters and bonds labeled.*

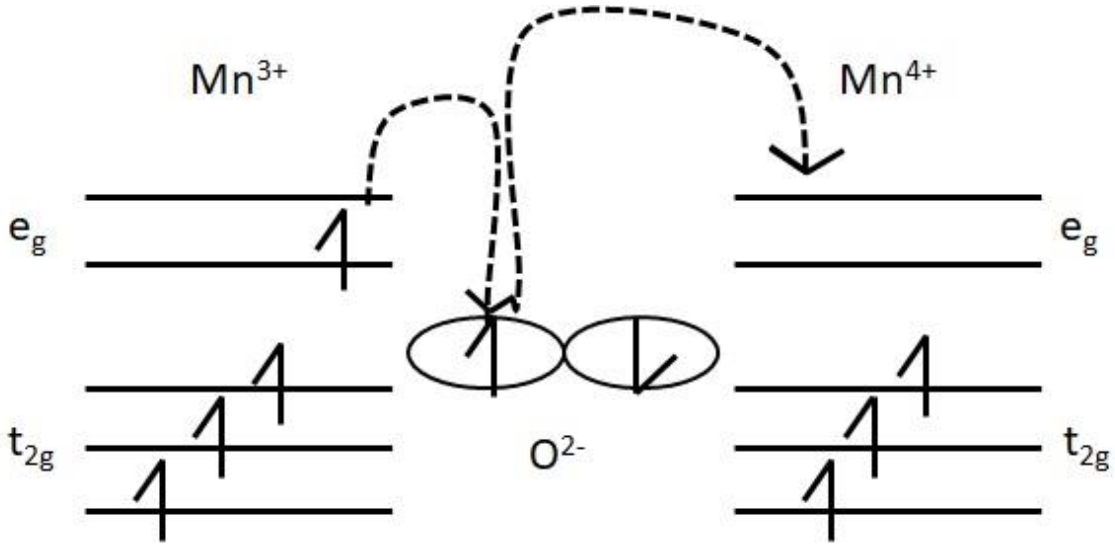

Figure 1.7 *Zener Double Exchange Mechanism.*

Because changing the energy requirements for Zener double exchange alters the magnetic properties, the MCE of lanthanum manganites can be affected by altering the Mn-O-Mn orbital overlaps through changing the Mn-O-Mn bond angles and distances as well as tuning the Mn ion oxidation states, namely the relative amount of Mn^{3+} versus Mn^{4+}.[3,49–51,65–67] Generally, ΔS increases as the average a-site radius decreases due to changing lattice parameters and orbital overlap.[13,57,61,68–73] The interactions between neighboring atoms in the crystal structure can also be affected by the coordination number of each atom. When a magnetic phase transition is occurring, as each spin state aligns with the magnetic field it influences its nearest neighbors and a cascade of alignment occurs. Thus, the Curie Temperature and ΔS are influenced by:

1) how close the neighbors are (influenced by the Mn-O-Mn bond distance and angle)[74–76]
2) the number of electrons available to exchange versus locations for them to exchange into (Mn ion oxidation states) [74–76]
3) the contribution of surface atoms and holes in the crystal lattice, which decreases the coordination number of involved Mn atoms by changing how many neighbors they have[74–76]

It has also been demonstrated that the magnetocaloric properties can be further tuned by entering the nanoscale, specifically allowing for the amount of hysteresis in the M(H) curve and the width of the MCE curve to be tuned with minimal change to the maximum ΔS or T_c values.[56,77–79] Because the magnetic properties of lanthanum manganites occur as a result of electron exchange across the Mn-O-Mn bond, which is dependent on orbital overlap and the way two manganese ions can interact, distortion of the lattice at the surface of the materials eliminates the magnetic properties there. This creates a magnetically disordered phase at the

surface of lanthanum manganites, particularly in smaller nanoparticles, called the Griffith's phase. The presence of this phase has been demonstrated to increase T_c, decrease the maximum ΔS, and increase the width of the MCE curve and the working temperature range. A plot of inverse magnetic susceptibility (χ) versus temperature which has a downturn deviating from the Curie Weiss Law confirms the presence of a Griffith's phase. (**Figure 1.8**).[28,80–85] The material should go from ferromagnetic to paramagnetic at T_c, which would lead to a straight line in the 1/χ plot above the Curie Temperature. When a magnetically disordered phase is present there exists a portion of the material which isn't paramagnetic above T_c, so perfectly paramagnetic behavior doesn't dominate until a higher temperature, T_G, when a straight line appears.[71,86–88]

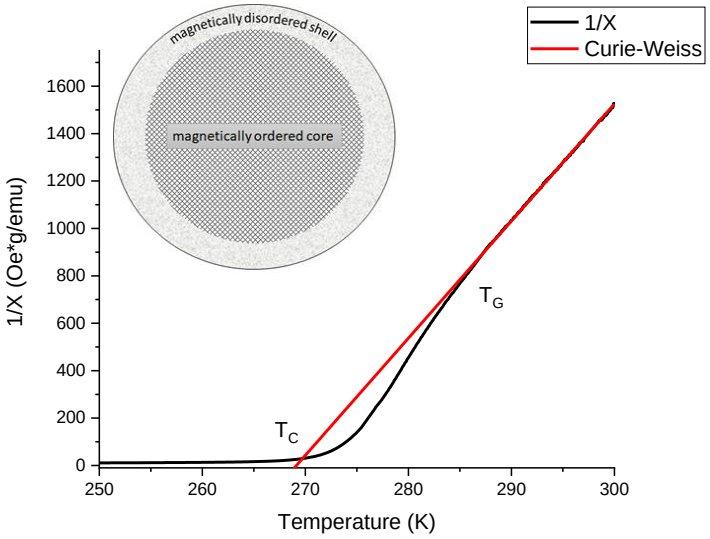

Figure 1.8 *A plot of the inverse magnetic susceptibility vs. temperature showing the Curie Temperature, T_c, and the Griffiths temperature, T_G. Between T_c and T_G the downturn in the plot is indicative of a deviation from paramagnetic behavior caused by the presence of a Griffith's phase. The inset is a pictorial representation of the magnetically disordered Griffith's phase surrounding the magnetically ordered core.*

Although they contain the rare earth metal lanthanum, lanthanum is significantly more abundant and less costly than the rare earths seen in the alloys discussed above. Additionally, the synthesis of manganites, particularly a sol-gel synthesis for creating nanoscale materials, is simpler and easier than the techniques mentioned above for other materials. The sol-gel synthesis of manganese oxides eliminates the need for high temperatures or an inert atmosphere and requires only environmentally friendly precursors.[3,13] Entering the nanoscale through a sol-gel synthesis has the added benefit of creating a more symmetrical MCE curve and a wider working temperature range.[3,42,51,66] Lanthanum manganite nanoparticles, therefore, hold unique promise for application in magnetic refrigeration as they have valuable and tunable magnetic properties and can be easily and inexpensively synthesized for commercialization.

1.4 Pechini Sol-Gel Synthesis

By using a sol-gel method as opposed to solid state reaction techniques to create lanthanum manganites the sintering temperature requirements are lowered and the potential for scale-up is increased. The Pechini sol-gel synthesis, patented in 1967 by Maggio Pechini, differs from a typical sol-gel synthesis in the use of metal nitrates, carbonates, or acetates dissolved with a chelating agent in an aqueous environment, as opposed to alkoxide precursors used in a typical sol-gel synthesis.[89–93] In the original Pechini method, α-hydroxycarboxylic acids were specified as the necessary chelating agent,[89] but others have since been shown effective to varying degrees.[91,91,94] Citric acid is the most commonly used acid as it can chelate cations that aren't monovalent and may otherwise be hydrolyzed in the aqueous solution.[91] The addition of a polyhydroxyl alcohol, most commonly Polyethylene Glycol (PEG), follows the addition of the citric acid, nitric acid, and metal precursors in order to promote gelation when heated to 100 °C.

Transesterification of the chelating agent and polyhydroxyl alcohol creates an organic matrix with the metal ions dispersed throughout ().

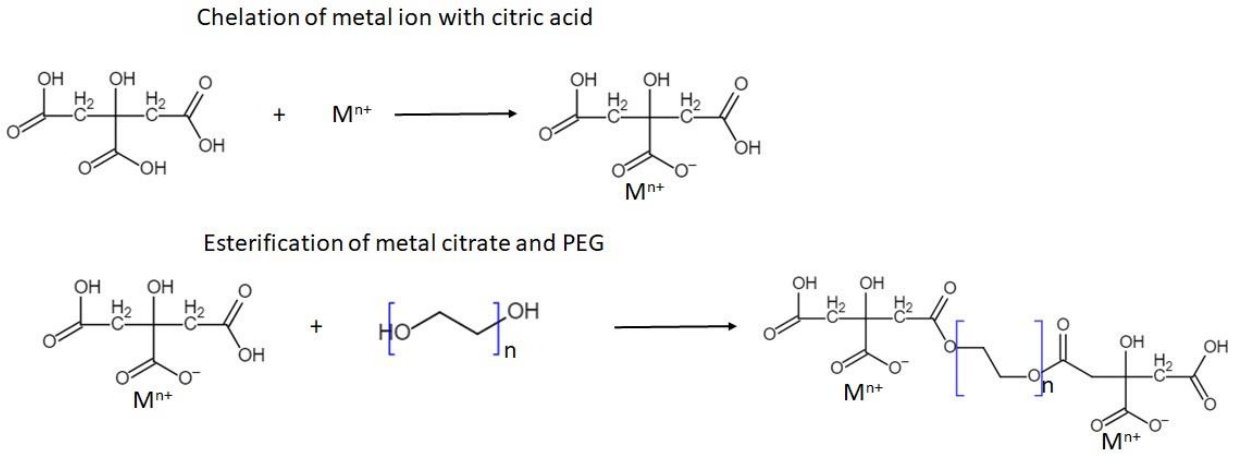

Figure 1.9 *Scheme of sol-gel synthesis chelation and esterification stages.*

Upon further heating to burn off the organic content a hard, homogeneous, polyester resin is created with the original stoichiometric amounts of the metal precursors preserved. The resin is then calcined to induce crystallization. The result is a nanocrystalline powder (**Figure 1.10**). Changes such as variations in the chelating agent, polyhydroxyl alcohol, and sintering temperature, and the elimination of the decomposition stage can all be found in the literature, though a systematic study of the effects of these changes has not been performed prior to this work.[89–91,94–96]

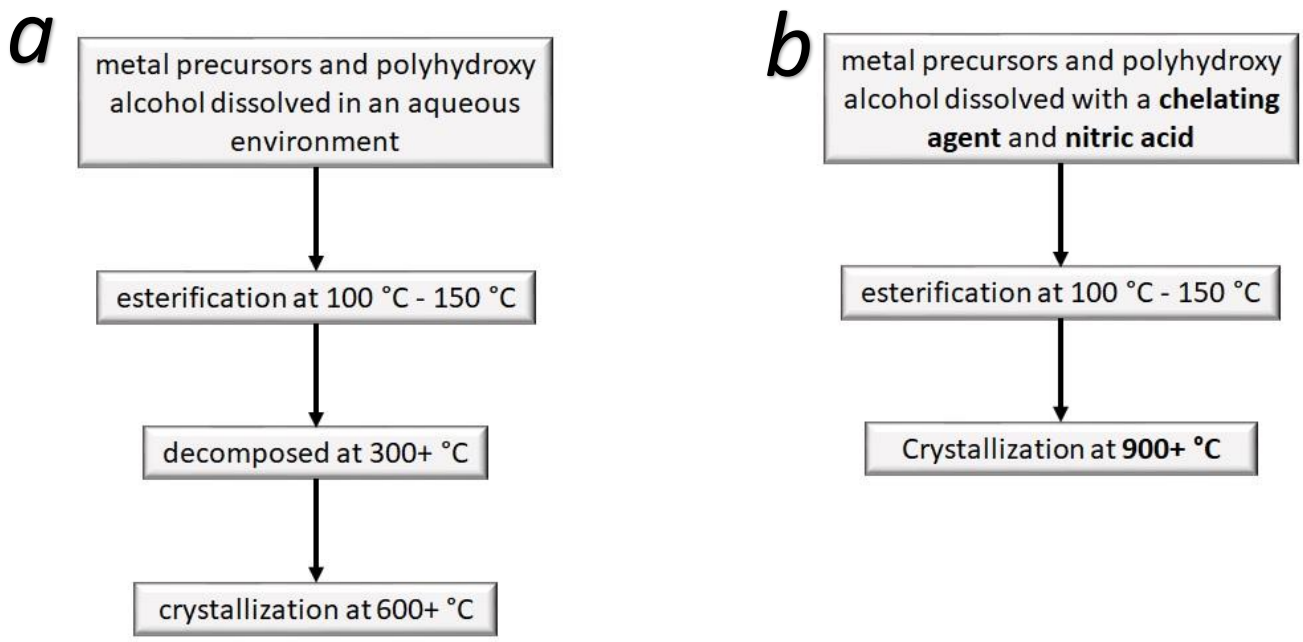

Figure 1.10 *Flowcharts showing the standard Pechini method (a), and the modified method used in this work (b). Notable differences are in bold.*

This method has been modified previously to include nitric acid in order to increase the acidity of the solution and promote better esterification.[56,95,97,98] In this work, the resin formation and/or decomposition stages have been omitted, which has been demonstrated advantageous to the magnetic properties of the resultant material.[4,56,97–100] An examination of an intermediary decomposition stage is carried out in Section 5.[7] Standard synthesis parameters used in this work were:

- citric acid at a concentration of 0.26 M
- PEG (MW 600) at a concentration of 0.08 M
- manganese (II) acetate tetrahydrate at a starting concentration of 1 M
- lanthanum (III) nitrate hexahydrate at starting concentration of 0.6 M

- calcium carbonate, sodium carbonate, strontium nitrate in stoichiometric amounts
- 10 mL of nitric acid
- prompt removal from heat after gelation
- sintered at 1000 °C for 10 hours and cooled slowly

1.5 Characterization Techniques

A wide variety of characterization techniques are necessary in order to characterize the synthesis itself, as well as the chemical composition, physical features, and magnetic behavior of the resultant materials.[101,102] The purpose of this section is to outline the characterization techniques used. Because some techniques are more ubiquitous than others some have been described more rigorously (**Table 1.3**).

Table 1.3 *Techniques employed in the presented work and their respective uses.*

TECHNIQUE	ADVANCED TECHNIQUE(S)	USE
X-RAY DIFFRACTION (XRD)	in-situ XRD Rietveld Refinement Scherrer Calculation	Phase determination, crystallite size, lattice parameters
VIBRATING SAMPLE MAGNETOMETRY (VSM)		Magnetic property determination
SCANNING ELECTRON MICROSCOPY (SEM)		Particle or aggregate size and surface texture determination, elemental mapping
LASER ABLATION – INDUCTIVELY COUPLED PLASMA – MASS SPECTROMETRY (LA-ICP-MS)		Elemental composition
DIFFERENTIAL SCANNING CALORIMETRY (DSC)		Heat capacity, thermal stability
THERMAL GRAVIMETRIC ANALYSIS (TGA)	Infrared Spectroscopy (TGA-IR)	Thermal stability Identity of evolved gases
X-RAY PHOTOELECTRON SPECTROSCOPY (XPS)		Element oxidation states

1.5.1 Powder X-Ray Diffraction (XRD)

Powder X-Ray Diffraction (XRD) is used to analyze the crystallinity, lattice parameters, crystal structure, and average crystallite size of materials. In XRD, x-rays striking the sample are scattered and diffracted according to Bragg's Law (Equation 5):

$$n\lambda = 2dsin\theta \tag{5}$$

where n is an integer, λ is the incident x-ray wavelength, d is the distance between crystal planes, and θ is the angle of incidence of the x-rays. As values of θ are scanned, diffraction occurs for each of the crystal planes present in the sample.[103–106] These have been catalogued in databases such as the International Center for Diffraction Data (ICDD).[103] Comparison of analyte patterns to this database allows for the determination of the crystal phase(s) present in the sample and indexing of peaks.[106–108] Advanced analyses for the determination of crystallite size and lattice parameters, as well as in-situ measurements in elevated temperatures or under various atmospheric conditions, are also possible.[103–105,107–113] The diffractometer used for this work was a Panalytical X'Pert Pro MPD Diffractometer equipped with a spinner stage and a zero-background silicon holder (single scan; 20° ≤ 2θ ≥ 90°; 0.010° step size; 1 s/step). PDF-2 ICDD Library 2004 Release pattern 00-046-0513 ($La_{0.60}Ca_{0.40}MnO_3$), which was used for comparison for materials created in this work, is shown in **Figure 1.11** with the most intense peaks indexed.

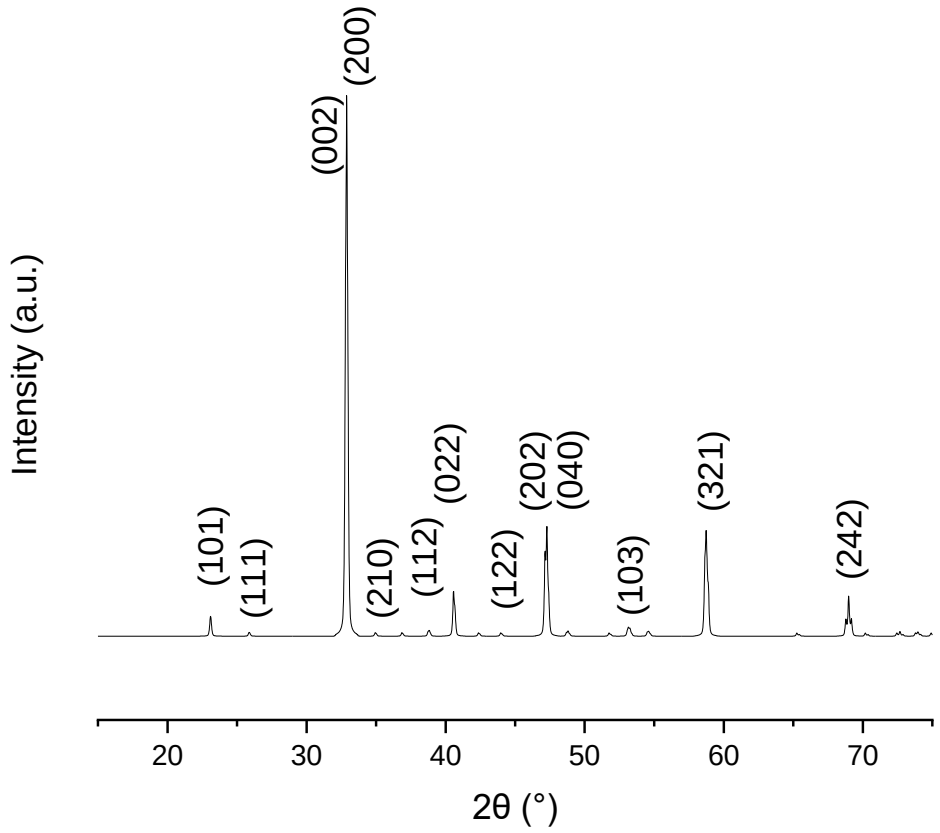

Figure 1.11 *Simulated XRD pattern from PDF-2 ICDD Library 2004 Release 00-046-0513 reference pattern.*

1.5.1.1 Scherrer Analysis

Scherrer analysis allows for the determination of average crystallite size. Theoretically, a diffraction peak for a perfect crystal system would have a width of zero because of a constant interplanar distance, d.[107,109] Experimentally, diffraction peaks have non-zero widths as a result of instrumental line broadening, which can be determined by running a standard and then subtracted out of experimental patterns, and size effects prevalent in nanoscale systems.[107]

Crystallite size is inversely proportional to peak width and can be determined using Scherrer's formula (Equation 6):

$$size = \frac{K\lambda}{FWHM \cos\theta} \quad (6)$$

where K is the Scherrer constant, which typically falls between 1.0 and 0.9 and is dependent on the crystal structure of the analyte, λ is the wavelength of the incident x-rays, FWHM is the full width at half maximum intensity of one diffraction peak (subtracting out instrumental broadening), and θ is the angle of the incident x-rays.[106] Although this is a powerful and useful tool, it must be noted that this calculation is biased toward the largest crystals. Large crystallites have the highest degree of crystallinity and more greatly affect peak broadening than any small crystals present in the sample.[103,110,111] Scherrer analysis in this work was carried out using the Scherrer Calculator feature in X'Pert High Score Plus analysis software.

1.5.1.2 Rietveld Refinement

Another powerful XRD tool is Rietveld Refinement. In this technique, standard phase parameters such as space group, lattice parameters, and atomic positions are used to model the phases determined to be present in the sample.[112,114,115] Patterns in this work were compared to PDF-2 ICDD Library 2004 Release, PDF reference number 00-046-0513. The model is then compared to the experimental data using computer software (X'Pert High Score Plus) and through refinement reasonably accurate phase percentages, bond distances, bond angles, and lattice parameters can be determined.[112,114,115] Error arises in both Rietveld refinement and crystallite size determination from line broadening due to small crystallites (exacerbated when a sample has very small crystallites or when a few large crystallites are present in a sample with

mostly small crystallites) and deviations in peak positions of up to 2θ=0.01° due to inherent instrumental error. Error in lattice parameters is ≈0.002 Å; error in bond distances and angles is ≈0.02%, dependent on the error in the atom positions for the referenced pattern in addition to the instrumental and peak position error mentioned above.[102,112,115,116]

1.5.2 Vibrating Sample Magnetometry (VSM)

Vibrating Sample Magnetometry is used to measure the magnetic properties and responses of a material. The sample is vibrated at a constant frequency in between two pick up coils with a magnetic field applied perpendicular to the vibration axis. The resulting magnetic flux creates an electric potential through Faraday Induction which is proportional to the material's magnetic moment. [117–120] Through manipulation of the applied temperature and field important values such as the Curie Temperature (T_c), magnetic entropy change (ΔS), magnetocaloric working temperature range (ΔT_{FWHM}), magnetic saturation (M_s), and magnetic domain size (d_s), as well as a measure of the magnetic domain size distribution (difference between T_b and T_{bif}) can be determined.

All VSM measurements were obtained using a Quantum Design DynaCool Physical Property Measurement System (PPMS) with a Vibrating Sample Magnetometer Option. Unless otherwise stated, Zero Field Cooled (ZFC) and Field Cooled (FC) M(T) curves for the determination of T_c (taken as the temperature where $(\delta M/\delta T)_H$ is maximized in the FC curve), T_b (taken as the temperature where the ZFC curve is maximized), and T_{bif} (taken as the temperature where the FC and ZFC curves deviate) were obtained from 50K to 300K at 100 Oe (**Figure 1.3**); M(H) curves for the calculation of ΔS (calculated according to the equations given in Chapter 1), ΔT_{FWHM}

(taken as the full width at half maximum of the ΔS curve) were obtained from 220K to 320K at 5K intervals over an applied field of 3T (**Figure 1.2**). d_s was calculated using Equation 7:

$$d_s = \left[\left(\frac{18k_BT}{\pi\rho_x M_s^2}\right)\left(\frac{\Delta M}{\Delta H}\right)_{H=0}\right]^{\frac{1}{3}} \quad (7)$$

where k_B is Boltzmann's constant, ρ_x is the density, T is the temperature (220K used in this work), M_s is the magnetic saturation (found using the M(H) curve taken at 220K across 3T), and $(\Delta M/\Delta H)_{H=0}$ is the slope of the 220K M(H) curve at H=0 (**Figure 1.12**).[120] Any deviations from these parameters are described in the relevant "Experimental Details" sections for each chapter.

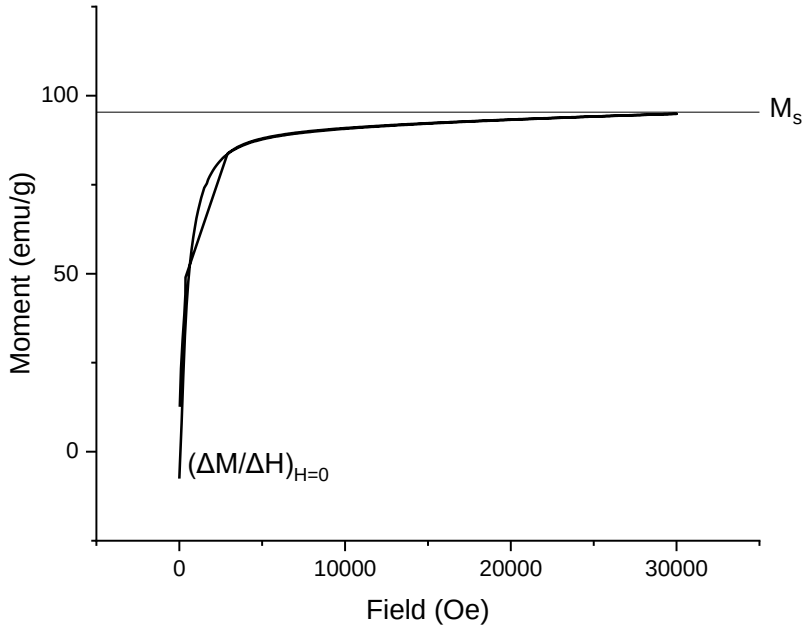

Figure 1.12 *Example MH curve used to find M_s, $(\Delta M/\Delta H)_{H=0}$, and ΔS.*

1.5.3 Scanning Electron Microscopy (SEM)

Because the size and shape of a magnetic particle can appreciably alter the magnetic properties, determination of particle size and shape is important.[121,122] Although crystallite size can be determined using XRD,[107,108] and magnetic domain size can be determined from magnetics measurements,[31] these are not always indicative of particle size and do not give information regarding surface texture (**Figure 1.13**). Imaging of the particles is therefore necessary. A Scanning Electron Microscopy image is created by mapping the electrons scattered off the surface of the sample.[123–125] This allows for visualization of particle size, any amorphous material present, surface texture, and overall shape. All SEM images in this work were obtained on a Hitachi SU-70 FE-SEM at an 8-10 mm working distance with a beam energy of 5 kV after sputter coating with Au. Samples were mounted to SEM pucks using double-sided carbon tape.

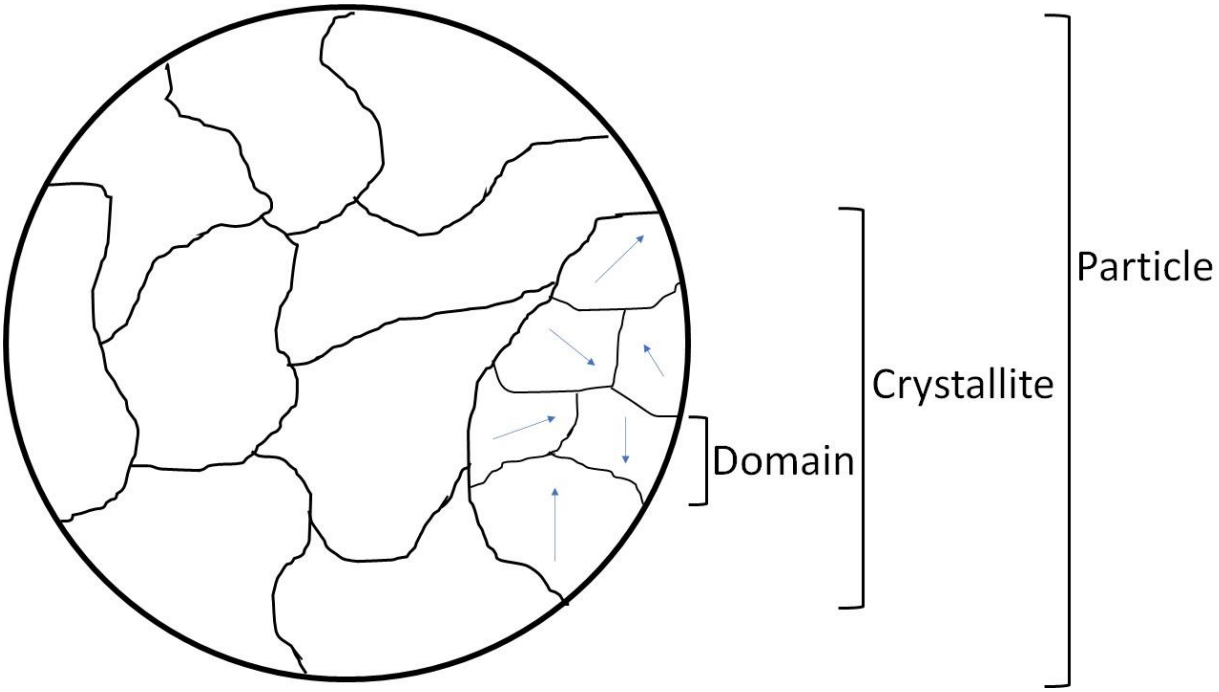

Figure 1.13 *Depiction of magnetic domain, crystallite, and particle.*

1.5.4 Laser Ablation-Inductively Coupled Plasma-Mass Spectrometry (LA-ICP-MS)

Inductively Coupled Plasma (ICP) techniques, both ICP-Mass Spectrometry (ICP-MS) and ICP-Optical Emission Spectroscopy (ICP-OES), are commonly used for the determination of the chemical formula of materials. In the general methods, the samples must be dissolved, usually in a weak nitric acid solution.[126,127] This presents a challenge for materials which do not readily dissolve. Solid samples can be more easily analyzed by adding laser ablation to the ICP-MS technique, creating LA-ICP-MS.[126,127] Powder samples in this work were pressed into 13 mm pellets and analyzed using an NWRfemto laser ablation system and an Agilent 7900 ICP-MS (20 sec laser pulse; 30 µm diameter; 30 Hz rep rate; 8 J/cm power) using internal standards for comparison.[128]

1.5.5 Differential Scanning Calorimetry (DSC

Differential Scanning Calorimetry (DSC) measures the difference in the heat flow required to raise the temperature of a sample and a reference material; that difference is plotted as a function of temperature. Endothermic events show a negative peak in the heat flow vs. temperature plot whereas exothermic events exbibit positive peaks. In the final stages of the sol-gel synthesis of lanthanum manganites, potential events are evaporation of water, decomposition of the gel's organic components, melting, and recrystallization. A Thermal Analysis DSC model Q200 was used in this work for in-situ characterization of the gel decomposition and sintering stages of the synthesis. Operating temperature was 25 °C to 600 °C and analysis was carried out in aluminum analysis pans under a nitrogen atmosphere with a ramp rate of 10 °C/min.

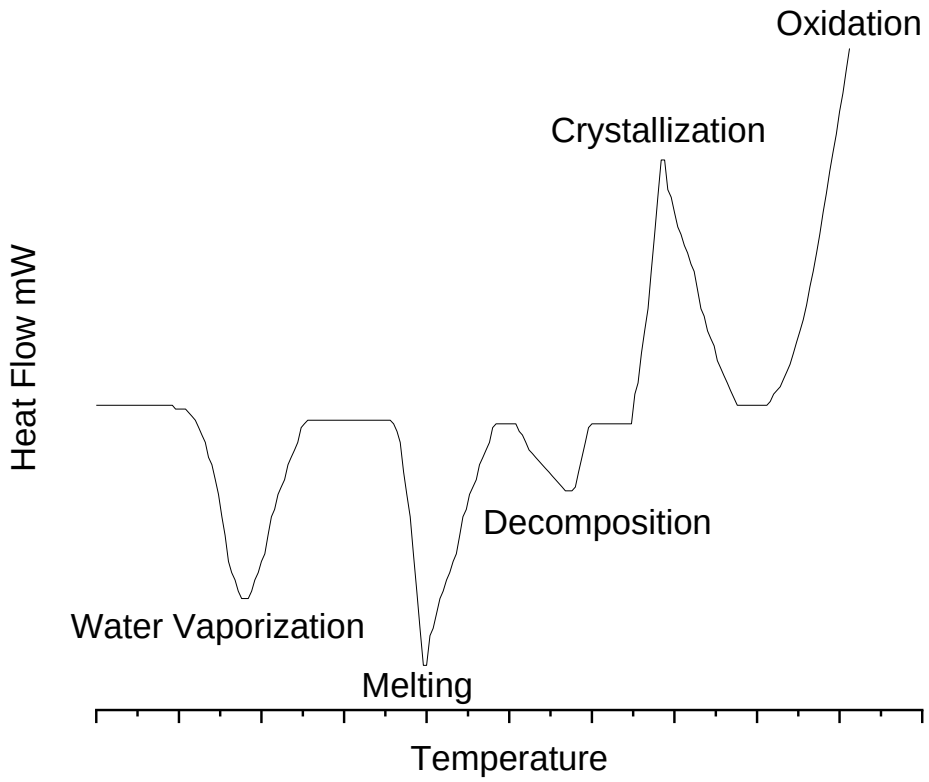

Figure 1.14 *Example DSC curve with important features labeled.*

1.5.6 Thermal Gravimetric Analysis (TGA)

Thermogravimetric Analysis (TGA) monitors the mass of a sample as its temperature is changed. Percent mass is then plotted as a function of time or temperature in order to monitor the evaporation or decomposition of water or organic material, or any oxidation if the analysis is performed under air (**Figure 1.15**). The addition of Infrared Spectroscopy (IR) on the evolved gases, creating a combined technique called TGA-IR, allows for identification of the decomposition products and evaporated gases (**Figure 1.16**). The TGA-IR setup used for this work was composed of a Thermal Analysis q500 TGA and Nicolet 6700 FTIR. Analyses were performed

under nitrogen in sealed aluminum pans. TGA temperature range for characterization of the decomposition stage was 25 °C to 200 °C. For characterization of the sintering stage the upper bound was increased to 600 °C. The FTIR cell and transfer line were set at 200 °C and the analysis was performed between wavenumbers of 500 cm^{-1} and 4000 cm^{-1}.

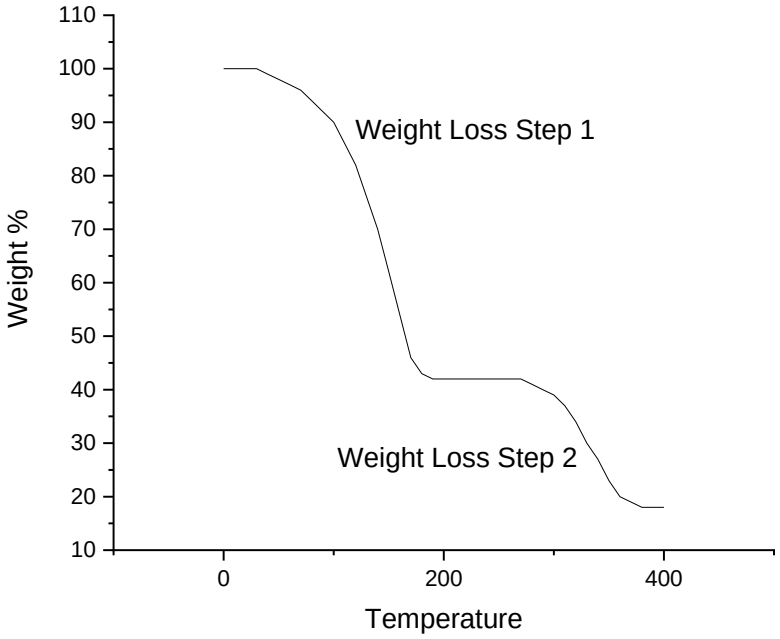

Figure 1.15 *Example TGA curve with two weight loss steps which could be from the loss of water (step 1) and decomposition of organic content (step 2).*

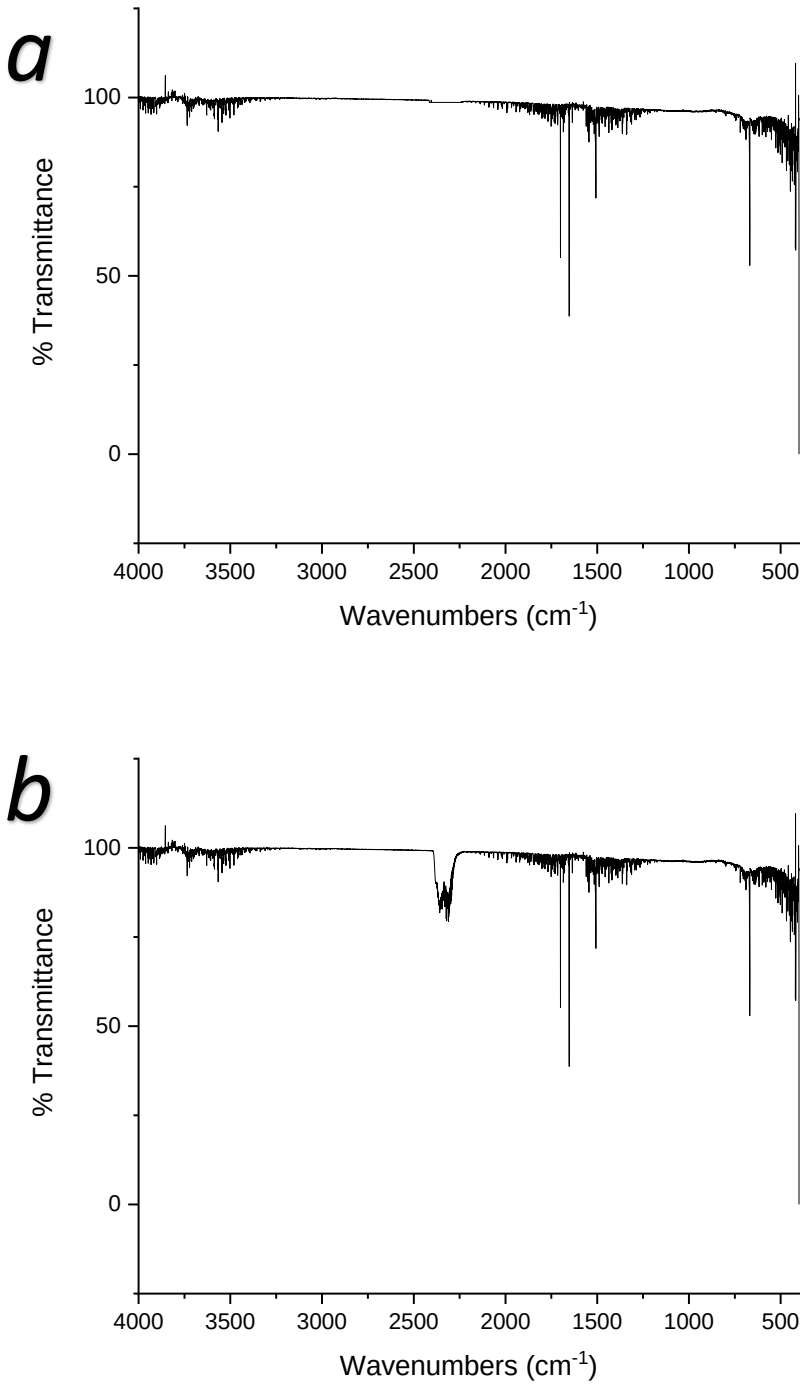

Figure 1.16 *Example IR curves which could correspond to the example DSC curve given above. (a) shows what the IR spectrum collected during the first weight loss step may look like, which only H_2O present in the spectrum. (b) shows the second weight loss step where CO_2 is also being detected as a result of organic decomposition.*

1.5.7 X-Ray Photoelectron Spectroscopy (XPS)

X-Ray Photoelectron Spectroscopy (XPS) characterizes the oxidation state(s) of the present elements. The surface of the sample is irradiated with x-ray light which excites the core electrons. The energy of those electrons is equal to the energy of the incident light minus the electron's binding energy, which is unique to the element and energy level. Higher measured binding energies correlate to more electronegative atoms and more positive oxidation states.[105] The XPS instrument used in this work was a PHI VersaProbe III Scanning XPS Microprobe and data processing of the collected spectra, including peak deconvolution and oxidation state quantification, was completed using CasaXPS software.[129]

1.6 Summary of Objectives

The goal of this work was to develop a material that has potential in a practical magnetic refrigeration system by maximizing ΔS near room temperature. This was done by doping LCMO materials at the a-site and altering synthesis parameters to affect changes in the Mn-O-Mn bond angles and distances, Mn oxidation states, and nanoparticle crystallite sizes. Some key objectives were:

- Introduction of a-site size disorder through substitution of Sr^{2+} in place of Ca^{2+} in the $La_{0.6}Ca_{0.4}MnO_3$ crystal structure in order to tease out the effects of lattice parameters and strain on the magnetic properties[4]
- Tuning of Mn ion oxidation states through substitution of Na^{+} in place of Ca^{2+} in order to determine specifically the effects of Mn oxidation state, absent of appreciable lattice parameter effects, on the relevant magnetic properties[5]

- Tuning and optimization of synthesis parameters such as chelating agents, sintering time, cooling rate, and sintering temperature and examination of the effects of these parameters on the magnetocaloric properties which would result from the induced changes in crystallite size
- The application of the findings relating to $La_{0.6}$-based materials to $La_{0.75}$-based materials[7]

2 Altering Primarily the Mn-O-Mn Bond Distance and Angle Through Strontium Substitution

2.1 Overview

The work of Zener et. al demonstrated that the magnetic properties of lanthanum manganites are determined largely by the manganese oxidation states and the Mn-O-Mn bond angles and distances. The bond distances and angles affect the d-orbital overlap and therefore change the energy required for electrons to be passed across the Mn-O-Mn bond. A smaller bond angle increases orbital overlap, thereby increasing interactions.[50] Size disorder at the a-site affects this bond angle, enabling tuning of the magnetic properties. This disorder is introduced and tuned by doping of the a-site with Ca^{2+}, Sr^{2+}, Ba^{2+}, and Na^{+}, which have ionic radii of 114 pm, 132 pm, 149 pm, and 116 pm, respectively. Because LCMO materials have been shown to have the highest values of ΔS, but LSMO and LBMO materials have more favorable T_c values, doping LCMO materials with an additional cation has the potential to correct T_c while maintaining a useable ΔS.[3,13,68,69,130–133] Introducing Sr^{2+} into LCMO nanoparticles synthesized via a modified Pechini sol-gel synthesis showed the anticipated decrease in ΔS, but without further synthesis modifications T_c did not change.[4] Because Sr^{2+} and Ca^{2+} have significantly different ionic radii but the same oxidation states, replacing Ca^{2+} with Sr^{2+} affects the bond distances and angles without altering the Mn oxidation states.

2.2 Experimental Details

The modified Pechini sol-gel synthesis was carried out as described in section 1.4, with the standard citric acid and 10-hour sinter time at 1000 °C parameters used. The calcium carbonate

precursor was substituted out for strontium nitrate while maintaining a constant stoichiometry of Ca^{2+} and Sr^{2+} together to promote the creation of $La_{0.6}Ca_xSr_{0.4-x}MnO_3$ materials. Recipes for x = 0.4 (LCMO parent), 0.32, 0.24, 0.16, 0.08, and 0 (LSMO parent) were used. Because the Sr^{2+} was not incorporated into the material as effectively as the Ca^{2+} only the parent compounds were created with the same ending formula as initial stoichiometric amounts of precursors. The intermediate compounds, where both Sr^{2+} and Ca^{2+} were included in the synthesis, had a greater final amount of calcium than set up by the initial stoichiometry.

Analysis of the samples was done using XRD, LA-ICP-MS, and PPMS with no deviation from the parameters described in the Characterization Techniques section. The collected XRD patterns were compared to PDF-2 ICDD Library 2004 Release, PDF reference number 00-46-0513; Rietveld Refinement and Scherrer analysis were performed. M(T) and M(H) curves were acquired and T_c, T_b, T_{bif}, and ΔS were calculated as described previously.

2.3 Results and Discussion

XRD and ICP data show that only the x=0.4 and x=0 (the LCMO and LSMO parent compounds, respectively) recipes produced the anticipated material. The recipes for the x=0.32 and x=0.24 materials produced materials where x=0.39 and x=0.32, respectively, meaning Ca^{2+} was incorporated more effectively than Sr^{2+}. This carries forward more dramatically in the x=0.16 and x=0.08 recipes where the amount of Sr^{2+} in the starting solution was much greater than the amount of Ca^{2+}. Because it could not be effectively incorporated, skewing the stoichiometric ratios of lanthanum to the dopants, the materials produced were in the $La_{0.80}Ca_xSr_{0.2-x}MnO_3$ family, where x=0.15 and x=0.13. The T_c value for $La_{0.8}Ca_{0.2}MnO_3$ compounds is even further from

room temperature than for $La_{0.6}Ca_{0.4}MnO_3$ materials, so the unintended materials were set aside and further analysis was not carried out (**Figure 2.1**).[13]

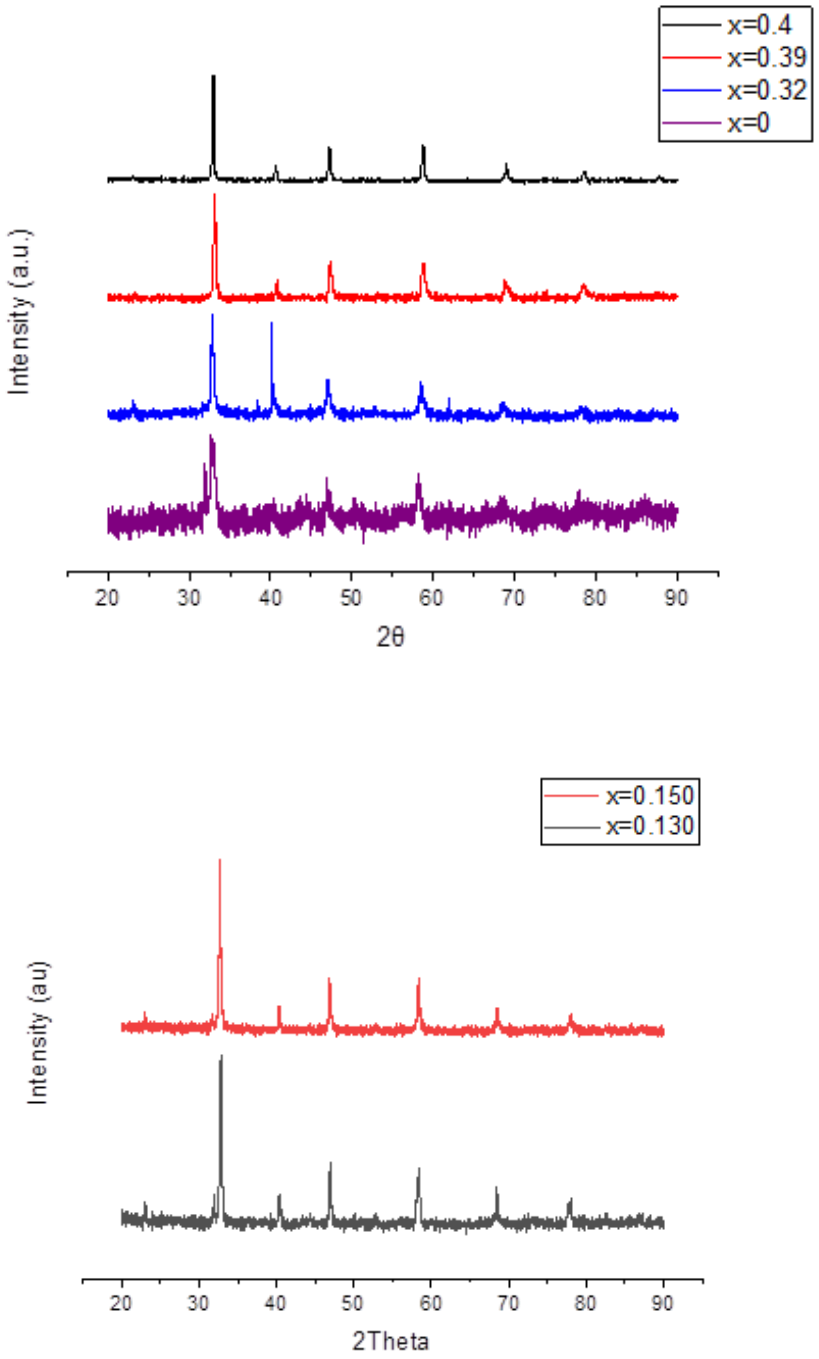

Figure 2.1. *XRD patterns collected for the materials where Sr was substituted in place of Ca. When Ca was more concentrated than Sr in the precursor solution* $La_{0.6}Ca_xSr_{0.4-x}MnO_3$ *materials were successfully*

synthesized where x=0.4, 0.39, 0.32 and x (a). When Sr was present in larger quantities than Ca $La_{0.8}Ca_xSr_{0.2-x}MnO_3$ materials were created (b).

The $La_{0.6}Ca_xSr_{0.4-x}MnO_3$ materials exhibit excellent phase purity, with the exception of the x=0.32 sample. The aberrant peak at 2θ=38° is likely from $LaMnO_3$. Through comparison with ICDD patterns calcium oxide, manganese oxide, lanthanum manganese oxide, and other LCMO formulas have all been eliminated as contaminants as none of them provide a match for the peak at 38°. Although $LaMnO_3$ does have a peak at the appropriate location, the intensities of the other peaks appear to be too small to be present in the experimental pattern. This makes identification less definitive. In addition to phase purity analysis, Scherrer calculations and Rietveld Refinement were carried out to determine average crystallite size and lattice parameters (**Table 2.1**). As strontium content increases, the lattice parameters increase, with the exception of the "a" lattice parameter for the x=0.32 material. This demonstrates distortion of the lattice which is likely responsible for the shifting magnetic properties.

Table 2.1. *Rietveld Refinement and Scherrer Calculator results from XRD data showing how crystallite size decreased as Sr was incorporated. The error on the lattice parameters is ±0.002. The error on the Mn-O-Mn angles is ±0.2*

X	Crystallite Size (nm)	a (A)	b (A)	c (A)
0.4	70.2	5.452	7.706	5.442
0.39	37.0	5.482	7.756	5.445
0.32	32.4	5.406	7.780	5.510
0	16.1	5.509	7.788	5.543

As strontium levels increase, M_s and maximum ΔS both decrease (**Figure 2.2**). M_s values decrease from 97 emu/g to 33 emu/g; ΔS values decrease from 5.6 J/kgK to 1.5 J/kgK, which is a 73% decrease. This is congruent with the patterns seen in bulk $La_{0.6}Ca_{0.4}MnO_3$ materials and in

LCMO nanomaterials of other formulas.[3,13,134] Additionally, the maximum ΔS values observed are comparable or even larger than those found previously in both bulk and nanoscale systems.[13,56,134] This suggests that shorter bonds and a smaller crystal lattice promote the MCE.

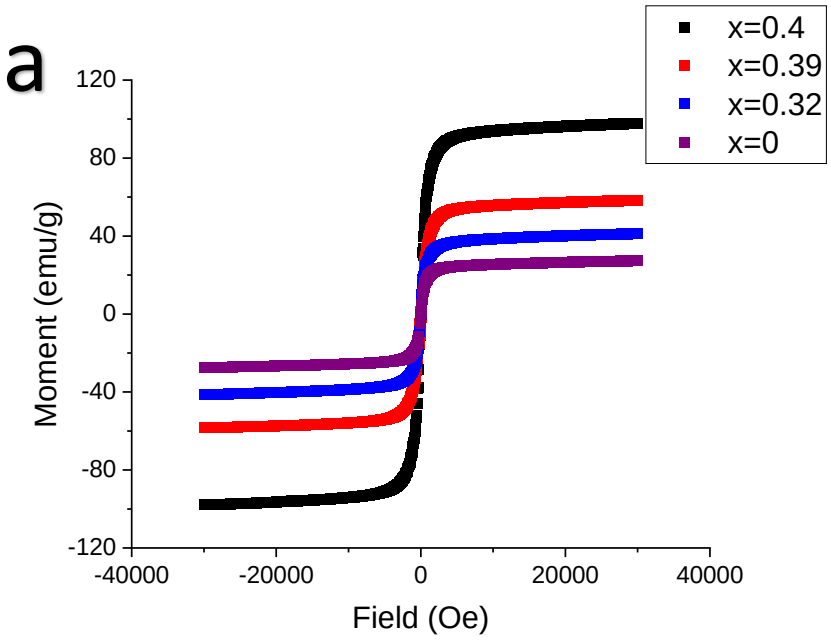

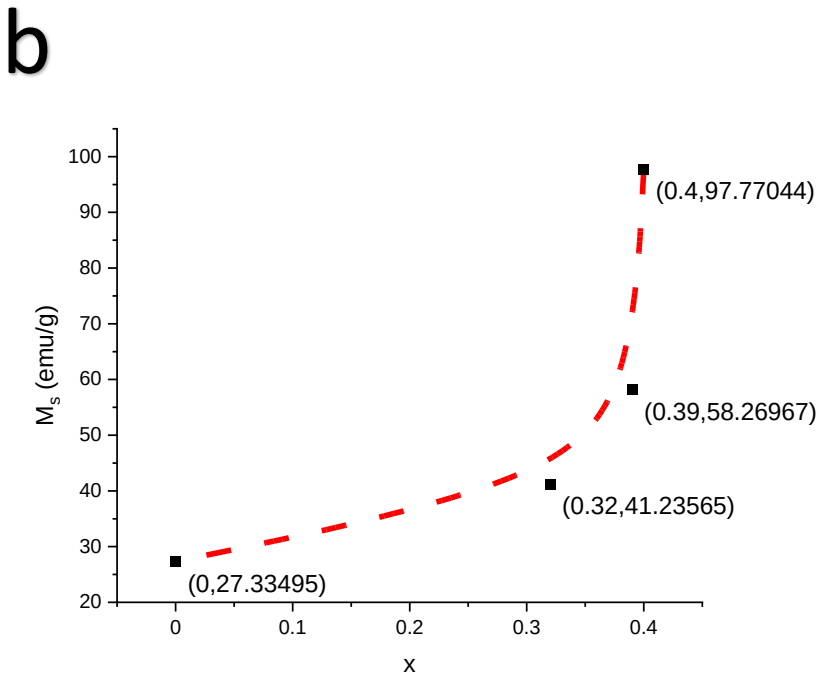

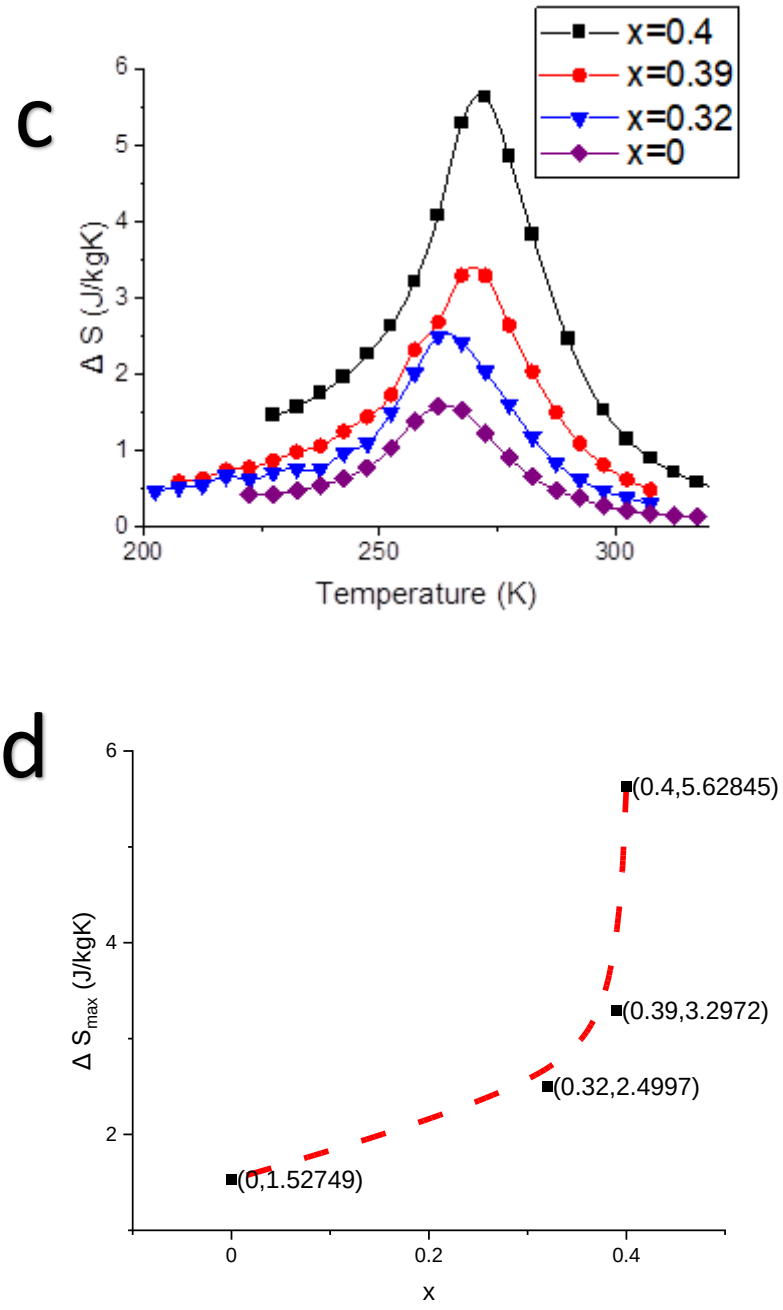

Figure 2.2. *(a) M(H) curves collected at 220K across 3T. M_s values are shown in (b). (c) ΔS curves calculated at 5K intervals from 200K to 320K across 3T. As x decreases (Sr increases) M_s and ΔS both decrease as is congruent with previous findings in the literature for bulk materials. Maximum ΔS values are shown in (d)*[13]

The average magnetic domain sizes, d_s, increase slightly with Sr content. The calculated values were 6.76 nm (x=0.4), 7.45 nm (x=0.39), 10.08 nm (x=0.32), and 11.27 nm (x=0). The M(T) curves were also used to calculate T_b, T_{bif}, and T_{bif}-T_b for each material. T_b values were 239K, 230K, 242K and 230K for the x=0.4, x=0.39, x=0.32 and x=0 materials, respectively. T_{bif} values in the same order were 269K, 260K, 269K, and 261K. Accounting for the 0.1% error in the PPMS temperature measurement all T_{bif}-T_b values are ~30K, meaning the magnetic domain size distribution is uniform across the synthesized materials (**Table 2.2**).

Table 2.2 *Magnetic domain sizes, d_s, T_b, and T_{bif}, for each of the four strontium substitution materials.*

X	T_b	T_{bif}	T_{bif}-T_b	d_s
0	239	269	30	6.76
0.32	230	260	30	7.45
0.39	242	269	27	10.1
0.40	230	261	31	11.3

Unlike the change in ΔS, the expected increase in T_c as Sr^{2+} was introduced was not observed. For all four samples T_c remained constant at around 268 K (**Figure 2.3**). This is the expected temperature for the LCMO material – based on studies of bulk LCMO the introduction of strontium should increase T_c from 268K.[3] This can may be partially explained by the increased presence of a Griffith's phase as particle size decreases. A Griffith's phase is confirmed by a deviation from the Curie-Weiss law (**Figure 2.4**). Smaller nanoparticles have a more substantial surface area to volume ratio and therefore a larger contribution to the overall properties by the magnetically disordered shell. The x=0.4 material has two deviations from the Curie-Weiss Law which suggests the presence of multiple ferromagnetic to paramagnetic phase transitions and multiple competing magnetic phases above the Curie Temperature. The M(T) and $1/\chi$ graphs also

never show a complete flatline at the Curie Temperature which would be indicative of a perfect ferromagnetic to paramagnetic phase transition. This is potentially due to the x=0.40 crystallites being very small despite there being no change in the magnetic domain size distribution and the magnetic domain size being closer to the crystallite size. With fewer domains per crystal and much smaller crystallites the magnetically disordered shell and competing magnetic domains may not be averaging each other out as effectively for the smaller x=0.40 sample (**Table 2.2**).

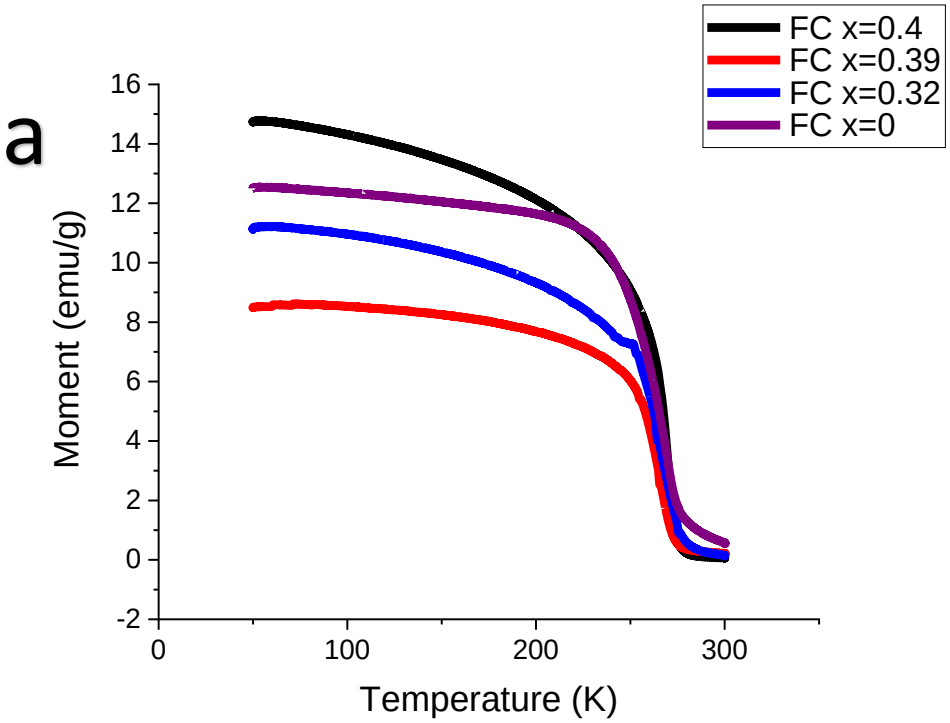
a
FC x=0.4
FC x=0.39
FC x=0.32
FC x=0
Moment (emu/g)
Temperature (K)
16
14
12
10
8
6
4
2
0
-2
0
100
200
300

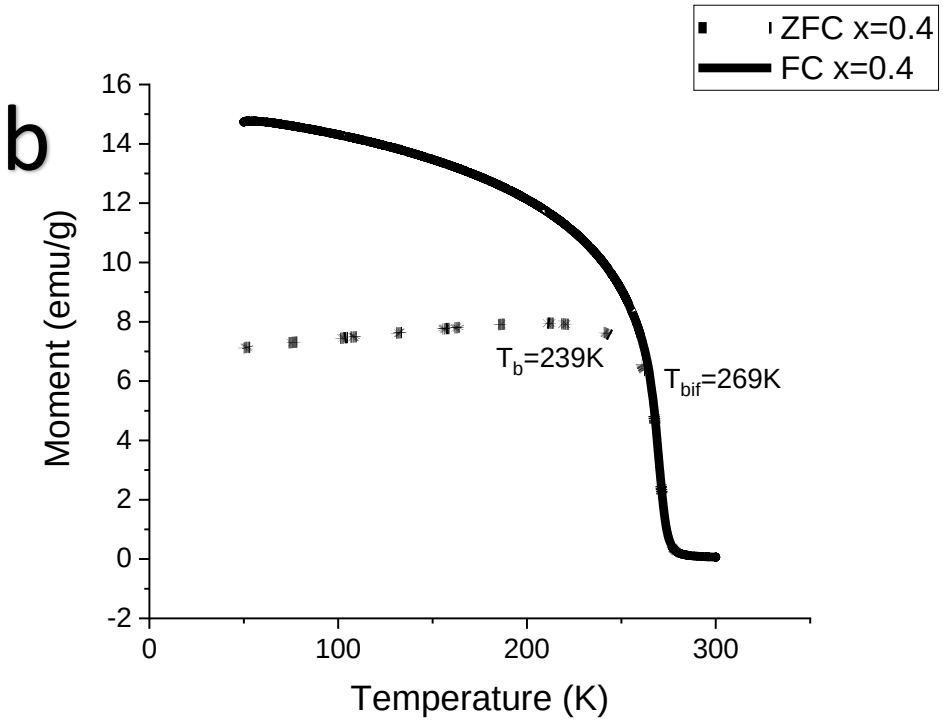
b
ZFC x=0.4
FC x=0.4
Moment (emu/g)
Temperature (K)
T_b=239K
T_bif=269K
16
14
12
10
8
6
4
2
0
-2
0
100
200
300

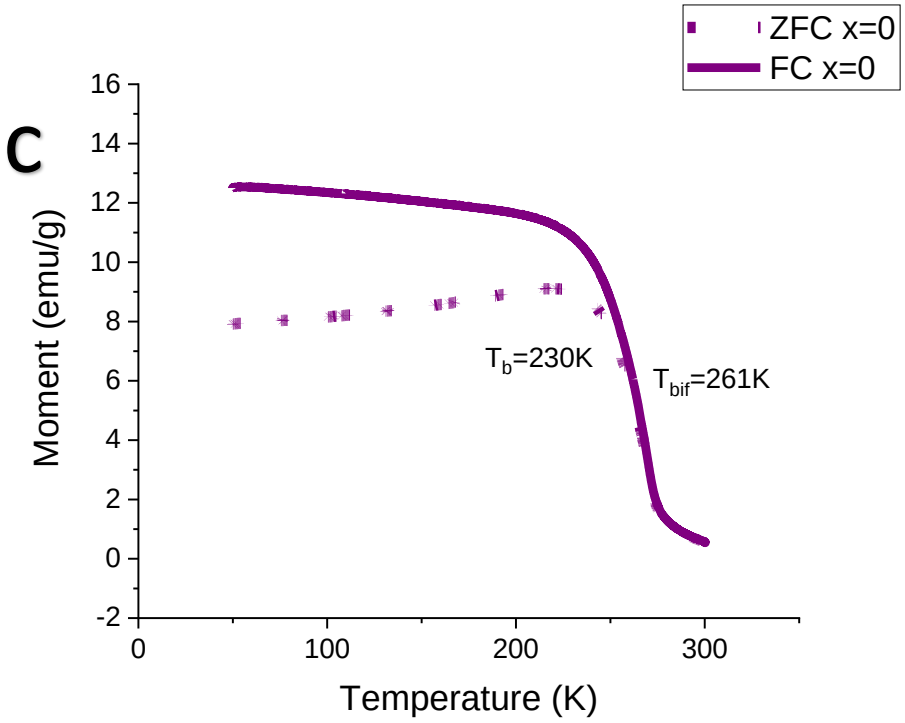

Figure 2.3 *(a) FC M(T) curves for each of the Sr substituted LCMO materials used to obtain the T_c value for each material, which was ~268K in all cases. (b) shows the FC and ZFC curves for the x=0 and (c) shows the FC and ZFC curves for the x=0.40 material, both with T_b and T_{bif} labeled.*

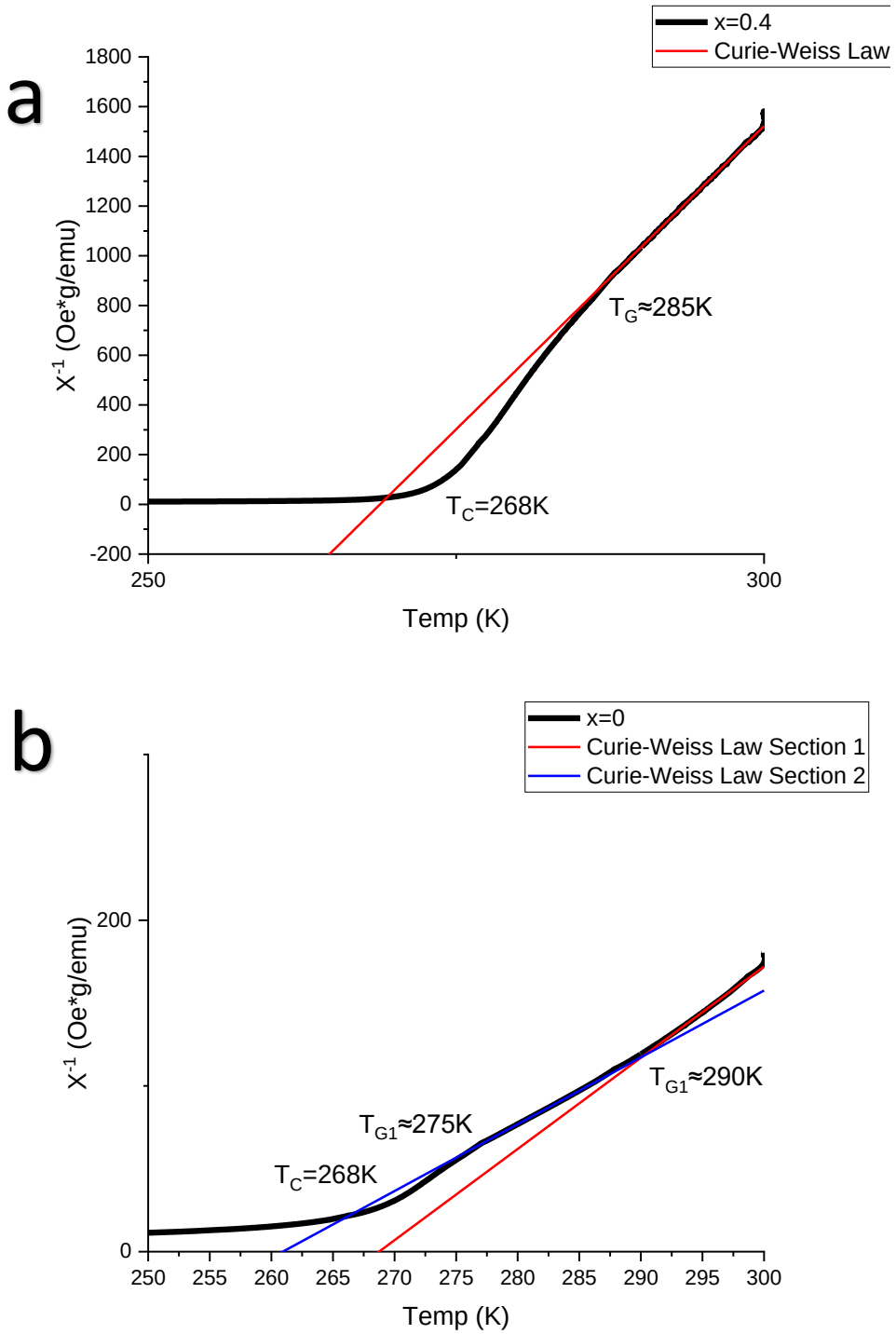

Figure 2.4 *Inverse of magnetic susceptibility plotted against temperature for the x=0.4 (a) and x=0 (b) samples along with the Curie-Wiess Law. The deviation near the Curie Temperature confirms the presence of a Griffiths phase which may partially account for the lack of a change in T_c expected as Sr is introduced.*

The SEM images show a noticeable decrease in particle size congruent with the decrease in crystallite size shown in the XRD. The particles, however, are considerably larger than the calculated crystallite sizes suggesting that each particle is composed of multiple crystals (**Figure 2.5**). This further supports the conclusion that an appreciable Griffith's phase is present and contributing to the magnetic properties observed. It also appears that the particles may become more spherical as opposed to irregularly shaped as Sr^{2+} is introduced, which may alter the anisotropy of the material and decrease the amount of magnetic hysteresis. Increasing the Griffiths phase through smaller crystallites may be decreasing T_c, thereby offsetting potential increases in T_c expected from the incorporation of Sr into the lattice.

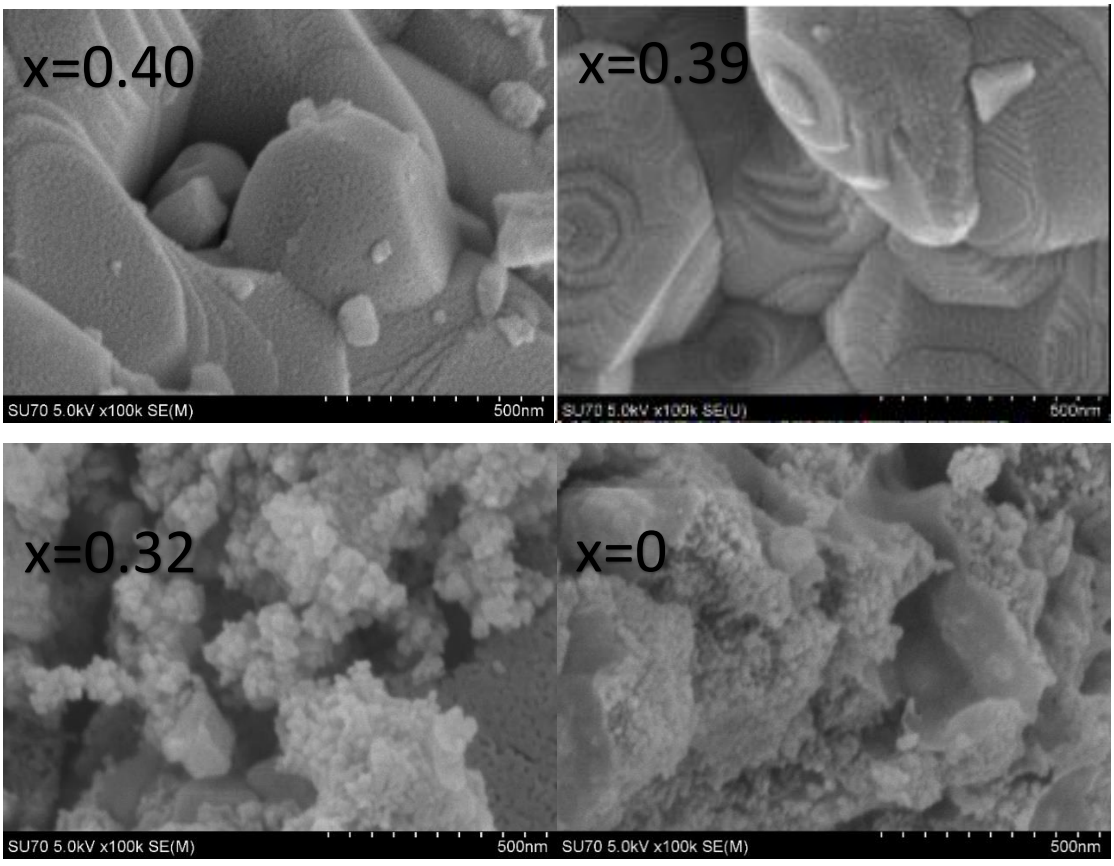

Figure 2.5 *SEM images for all $La_{0.60}Ca_xSr_{0.4-x}MnO_3$ materials. Appearance and texturing are appreciably different.*

2.4 Strontium Substitution Conclusion

As Sr^{2+} concentration increases (x decreases), which is larger than the Ca^{2+} it is replacing, the lattice parameters and strain increase. The resultant increase in the Mn-O-Mn bond distances and angles causes a decrease in ΔS from 5.6 J/kgK to 1.5 J/kgK as a result of the change in energy required for Zener Double Exchange interactions to occur. Recent work done by Zhang and Xu at North Carolina State University successfully predicted RCP using the lattice parameters alone, supporting the conclusion given here that the incorporation of the strontium ion in place of calcium and subsequent distortion of the crystal lattice leads to the change in ΔS.[135,136] It was anticipated that this would be accompanied by an increase in T_c, based on literature findings, which was not observed.[4,74] All samples have a T_c of ~268 K, which is what is expected for the LCMO parent.[3] This may be attributed to either a decrease in crystallite size as Sr^{2+} is introduced, the changing surface texture seen in the SEM images, or the absence of a change in the Mn oxidation states. Future chapters will explore how each of those attributes affect the magnetic properties of lanthanum manganites in order to understand what, if anything, is preventing the expected change in T_c.

3 Altering Primarily Mn Oxidation State Ratio Through Sodium Substitution

3.1 Overview

Introducing Na^+ in place of Ca^{2+}, in contrast to incorporating Sr^{2+} into the lattice as discussed in the previous chapter, keeps the average a-site radius and lattice parameters comparable while significantly altering the Mn oxidation states.[50,59,68,70,137] It was therefore proposed that doing each substitution in turn would elucidate the individual effects of the lattice parameters and Mn oxidation states on the magnetic properties. The previous chapter demonstrated that altering primarily the a-site cation average radius, in conjunction with an induced decrease in crystallite size, decreased ΔS without appreciably altering T_c. In this chapter, substituting Na^+ (ionic radius of 116 pm) into the lattice in place of Ca^{2+} (ionic radius of 114 pm) is shown to change the Mn oxidation states without affecting crystallite size or lattice parameters. This creates a less dramatic drop in ΔS than what was seen in the Sr^{2+} substitution as well as a significant increase in T_c. This suggests that the Mn oxidation state is primarily responsible for determining T_c while Mn-O-Mn bond distance and angle primarily dictates ΔS.[5]

3.2 Experimental Details

$La_{0.60}Ca_xNa_{0.4-x}MnO_3$ materials, where x=0.4, x=0.28, x=0.19 and x=0, were synthesized following the standard sol-gel synthesis described in section 1.4 with a sintering temperature of 1100 °C. Similar to the Sr^{2+} incorporation study, the starting ratios differed slightly from the resultant ratios though not as dramatically – x=0.30 and x=0.20 were the intended values. This is likely due to better affinity between citric acid and Na^+ compared to Sr^{2+}. LA-ICP-MS data for

formula confirmation, magnetics measurements for T_c and ΔS determination, XRD patterns for crystallite analysis, SEM imaging of particle size and surface texture, and XPS spectra for Mn oxidation state quantification were all obtained based on the parameters discussed in the first chapter.

3.3 Results and Discussion

As sodium content was increased (x decreases), the maximum ΔS value decreased, similar to the response seen with the introduction of strontium, though far less dramatic. Whereas introducing strontium decreased the maximum ΔS by 73% from 5.6 J/kgK (for the LCMO parent) to 1.5 J/kgK (for the LSMO parent), introducing sodium only decreased ΔS by 33% from 4.1 J/kgK to 2.8 J/kgK (**Figure 3.1a**). The T_c values, meanwhile, show a considerable increase with decreasing x (increasing Na^+) not seen in the Sr^{2+} substitution (**Figure 3.1b**). Additionally, T_b and T_{bif} are essentially the same for all four materials – the maximum of the FC curve occurs at nearly the same temperature as the temperature where the FC and ZFC curves separate. This implies a very narrow magnetic domain size distribution; the average magnetic domain size for all LCNMO materials is ~10 nm.[120,122,138]

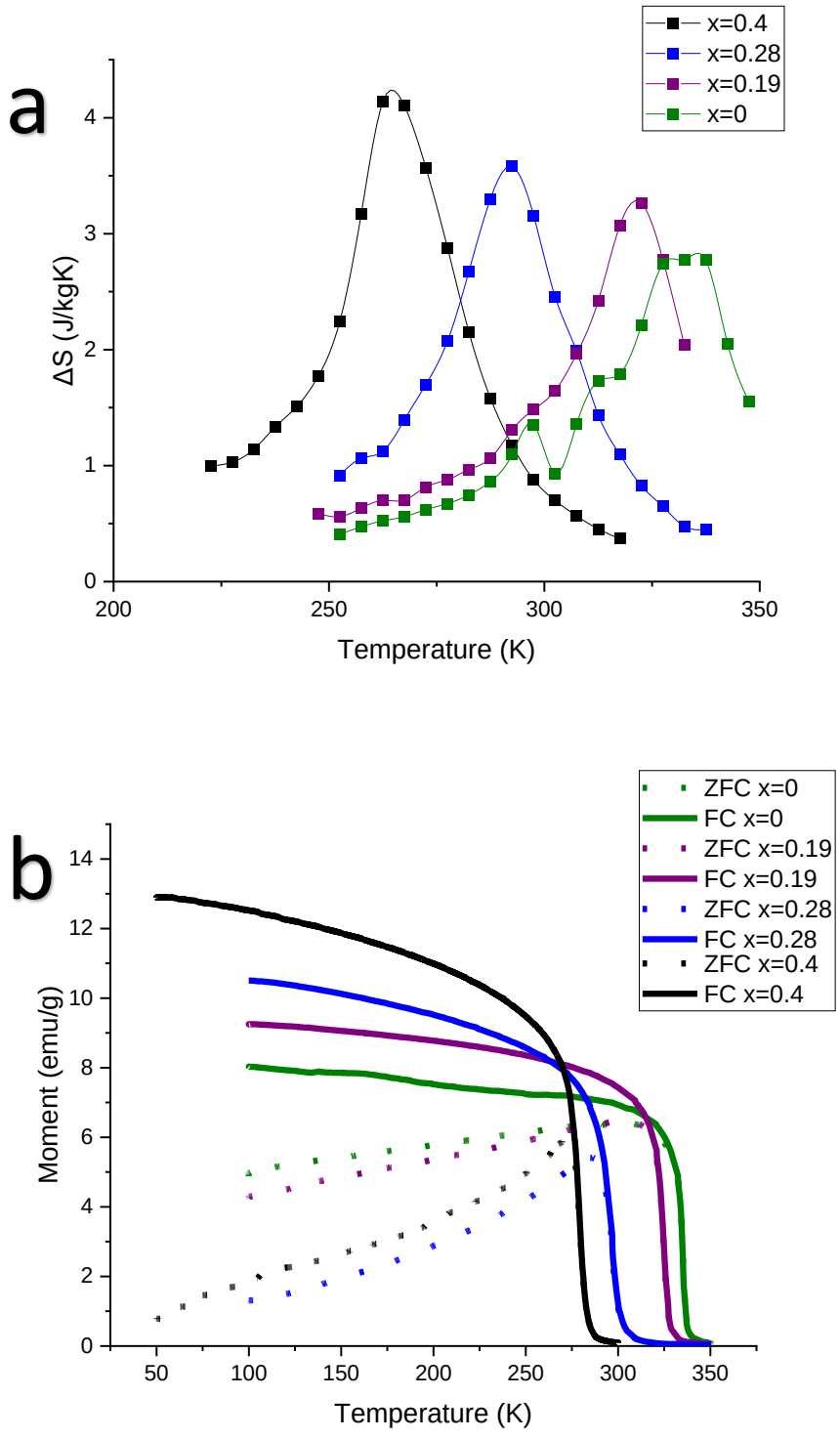

Figure 3.1. *MCE curves (a) and MT curves (b) for $La_{0.6}Ca_xNa_{0.4-x}MnO_3$ materials. The major irregularity just about 300K in the x=0 sample is the result of a measurement that stopped and restarted partway through after power loss to the system.*

The change in T_c, and potentially some of the change in ΔS, can be attributed to the alteration of the Mn oxidation states. Based on peak deconvolution performed on the Mn3s peaks in the obtained XPS spectra an increase in the percentage of Mn^{4+} and decrease in Mn^{3+} is observed with an increase in Na^+ content (**Table 3.1**). As more "openings" for electrons to transfer into present themselves with an increase in the percentage of Mn^{4+} and corresponding decrease in Mn^{3+}, T_c increases from 265K to 333K.

***Table 3.1**. Mn^{3+} and Mn^{4+}percentages and T_c values for LCNMO materials.*

x	Mn^{3+} (%)	Mn^{4+} (%)	T_c (K)
0.4	68.63	31.37	265
0.28	68.14	31.86	297
0.19	66.30	33.70	323
0	64.38	35.62	333

Based on the XRD patterns, crystallite size remains constant across the materials at ~40 nm. Lattice parameters are given in **Table 3.2**. Only the "a" lattice parameter increases appreciably outside of the ±0.002 Å error, with the exception of the x=0 material, where the "b" lattice parameter also sees an increase. It is worth noting that the peaks at 2θ≈33° and 70° begin splitting into two individual peaks as sodium content increases (**Figure 3.2**).

***Table 3.2** Lattice parameters for $La_{0.60}Ca_xNa_{0.4-x}MnO_3$ materials.*

x	a (Å)	b (Å)	c (Å)
0.4	5.457	7.700	5.450
0.28	5.460	7.701	5.442
0.19	5.482	7.700	5.448
0	5.496	7.741	5.449

a

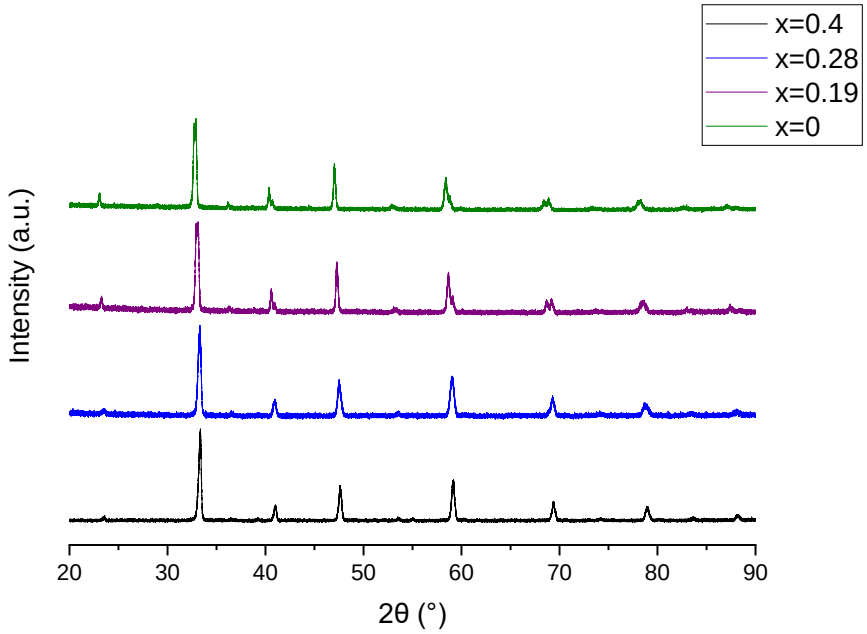
x=0.4
x=0.28
x=0.19
x=0
Intensity (a.u.)
20
30
40
50
60
70
80
90
2θ (°)

b

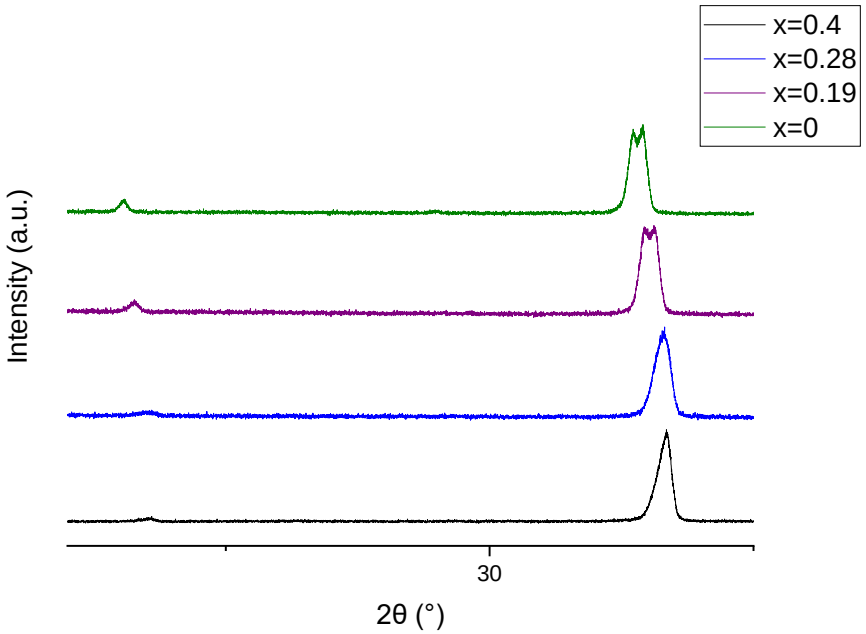
x=0.4
x=0.28
x=0.19
x=0
Intensity (a.u.)
30
2θ (°)

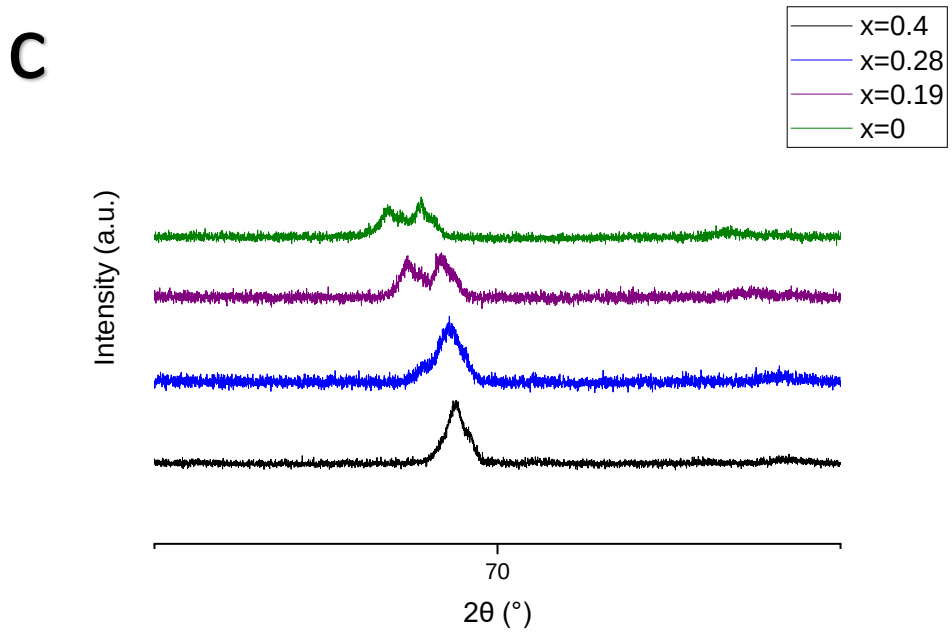

***Figure 3.2**. Complete XRD patterns (a), patterns focused on peak at 2ϑ≈33° (b), and patterns focused on the 2ϑ≈70 peak (c).*

The collected SEM images for all materials show particle sizes of ~500 nm, which implies that each particle is composed of multiple ~40 nm crystals. All particles have a similar irregular shape with soft edges and a textured surface. This contrasts with the trend seen when strontium was incorporated, where the resulting particles got progressively smaller and more spherical (**Figure 3.3**) and further supports the assertion that the primary influence on T_c is Mn oxidation state. Mn-O-Mn bond distance and angle appears to primarily affect ΔS as evidenced by the smaller change in ΔS observed here compared to the strontium substitution series.

a

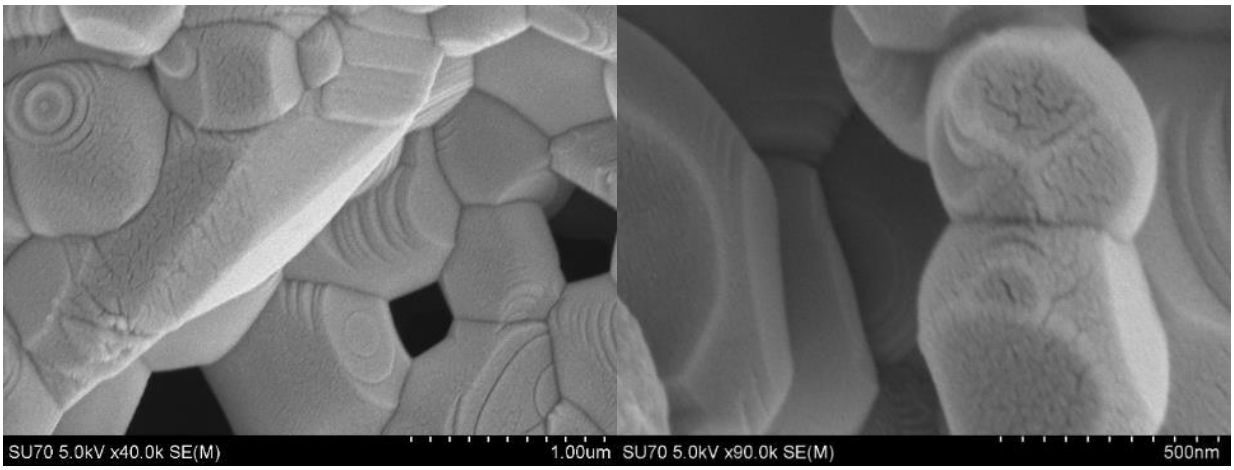
SU70 5.0kV x40.0k SE(M)
1.00um
SU70 5.0kV x90.0k SE(M)
500nm

b

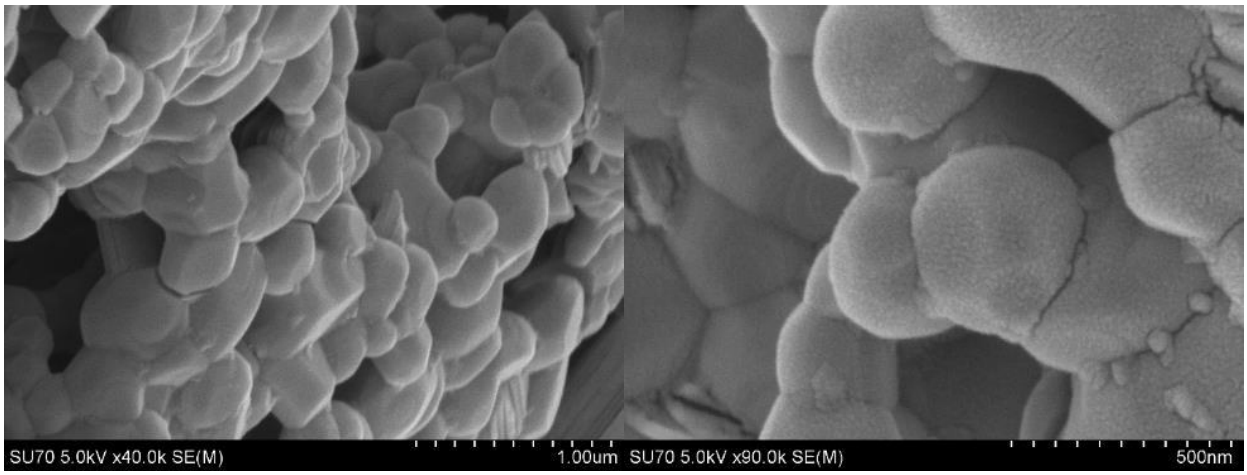
SU70 5.0kV x40.0k SE(M)
1.00um
SU70 5.0kV x90.0k SE(M)
500nm

c

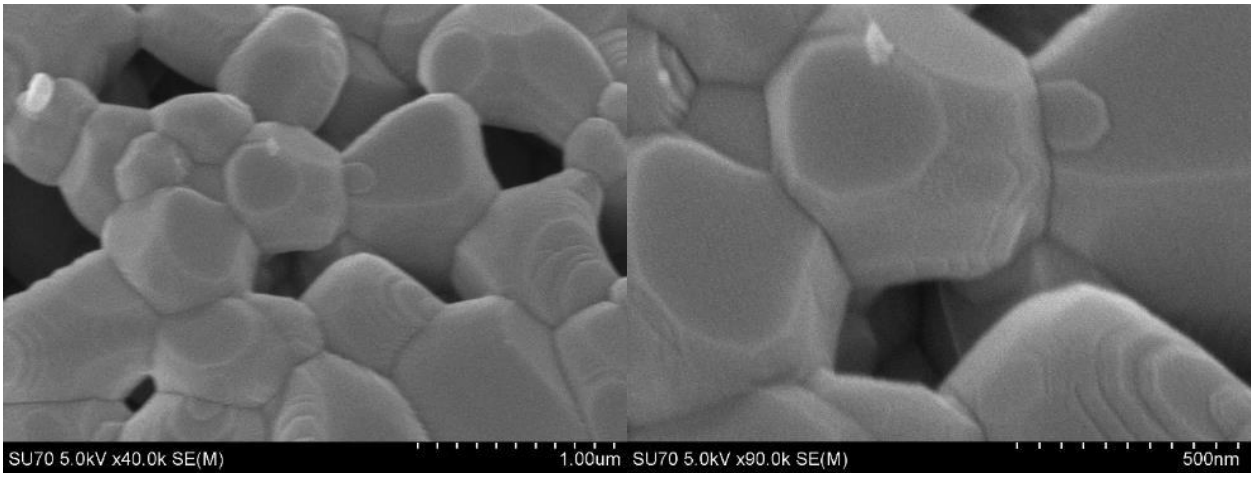
SU70 5.0kV x40.0k SE(M)
1.00um
SU70 5.0kV x90.0k SE(M)
500nm

d

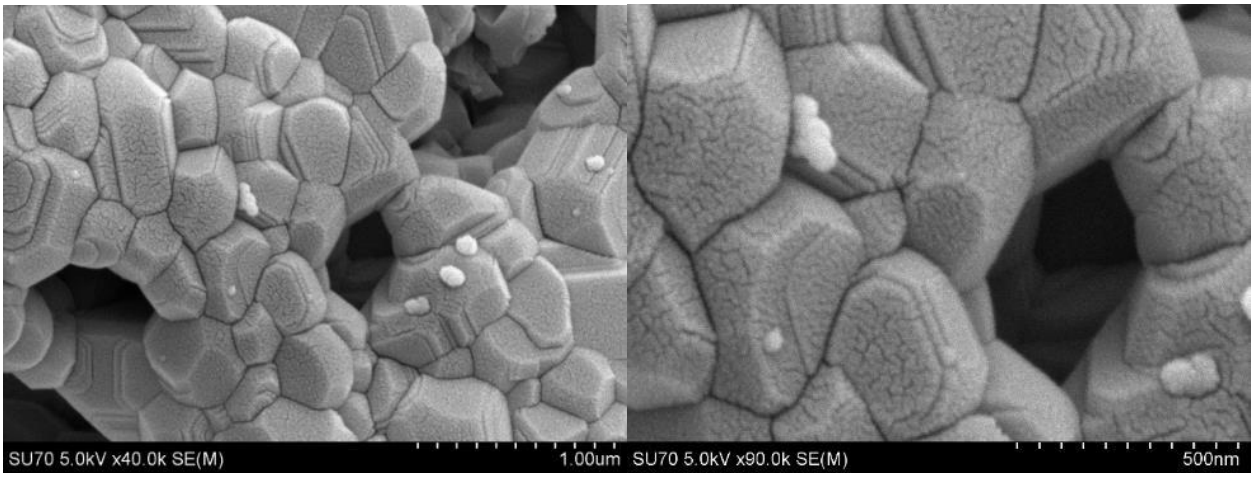

Figure 3.3. *Scanning Electron Micrographs of $La_{0.60}Na_{0.4}MnO_3$ (a), $La_{0.60}Ca_{0.19}Na_{0.21}MnO_3$ (b), $La_{0.60}Ca_{0.28}Na_{0.12}MnO_3$ (c), and $La_{0.60}Ca_{0.40}MnO_3$ (d).*

3.4 Na Substitution Conclusion

As the concentration of sodium was increased (x decreased) across the $La_{0.6}Ca_xNa_{0.4-x}MnO_3$ materials, Mn^{3+} percentage decreased from ~68% to ~64% and Mn^{4+} percentages increased from ~32% to ~36% creating additional Mn^{4+} "openings" for Mn^{3+} electrons to transfer into. The particle size, basic shape and texture, lattice parameters, and crystallite size, meanwhile, remained constant. This suggests that T_c, which increased dramatically from x=0 to x=0.4, is primarily controlled by the Mn oxidation states. When the results from the strontium substitution are considered along with these sodium substitution results it can be surmised that Mn-O-Mn bond distances and angles mostly affect ΔS, while T_c is mostly dictated by Mn oxidation states. This fits with the study mentioned at the end of the previous chapter wherein the RCP of manganites was successfully modeled using only the lattice parameters.[135] In addition, literature findings show that the introduction of iron in place of manganese at the b-site pushes T_c to lower temperatures.[139–141] By incorporating iron into the lattice the interactions between Mn^{3+} and Mn^{4+} are disrupted by the Fe^{3+} and the result is a significant decrease in T_c. This further supports

the conclusion that T_c is more affected by Mn ion oxidation states and the energy required for Zener Double Exchange to occur (and thus the ΔS value) is primarily affected by lattice distortion.

4 Altering Crystallite Size and Magnetic Properties Through Synthesis Optimization

4.1 Overview

In addition to the magnetic properties of manganite materials being dictated by the Mn-O-Mn bond angles and distances and Mn oxidation states, entering the nanoscale introduces effects due to crystallite size.[95] Across previous studies, there is an appreciable level of variability in specific synthesis parameters used and in how the Pechini sol-gel method has been modified for creating lanthanum manganites. While these synthesis alterations have been studied to some degree for other nanomaterials, no systematic study of the effects of various parameters on the crystal size and structure, particle surface features, and magnetic properties of LCMO materials has been completed.[95] In the Pechini sol-gel synthesis of yttrium aluminum garnet materials, for example, altering parameters such as sintering temperature, identity and concentration of the chelating agent, and the time and temperature of the gelation step has been shown to change the crystallinity, composition, and phase purity of the resulting nanopowders.[95] The citric acid to PEG ratio, sintering time, and other factors have also been demonstrated to change the surface texture, crystallite size, and other important features of other sol-gel synthesized materials.[90,94–97] By systematically altering parameters at every stage of the synthesis method optimal parameters for creating materials with a high ΔS and T_c near room temperature may be developed.

At the first stage of the synthesis, changing the chelating agent can affect the purity of the product. Swapping out the chelating agent in the creation of $YBa_2Cu_3O_{7-\delta}$ (YBCO) nanopowders,

for example, has been shown to affect the occurrence of a secondary $BaCO_3$ phase, with the use of EDTA eliminating the $BaCO_3$ phase altogether; this implies that the nature of the chelating agent and its ability to chelate the metals of the chosen material have a major impact on the phase purity of the final product.[142] Altering the starting concentration of all precursors or the molar ratios of the starting materials can affect surface texture and area, phase purity, crystallite size, particle shape, or other features. Changing the pH in the creation of calcium hydroxyapatite has been demonstrated to alter phase purity, grain size, and particle shape of the resulting materials.[143] Surface texture and surface area in sol-gel synthesized TiO_2 has been altered through molar ratios of starting materials and synthesis temperature.[144] In addition, polyethylene glycol of varying molecular weights has been analyzed in the creation of $La_{0.6}Ca_{0.4}MnO_3$ nanomaterials. This was demonstrated to alter the maximum ΔS values, with PEG 600 leading to the highest ΔS, followed by PEG 2000, then PEG 4000. This suggests that the higher the molecular weight of PEG the lower the ΔS. T_c, however, was not affected by which PEG was used.[97] In the work of Macedo et al. (2010), using gelatin and ethylene glycol was shown to be effective, with better chelation between the citric acid and metal ions assumed to be the cause of the increased crystallinity and homogeneity in the ethylene glycol products as opposed to the gelatin products.[145]

Because crystallization and particle formation both occur during the sintering stage, features such as crystal homogeneity, defects, crystallite size and strain, lattice parameters, and surface texture are all potentially affected by the sintering step of the synthesis. There is previous evidence demonstrating the effect on crystallite size, though other features have not been thoroughly analyzed. Increasing the sintering temperature of $La_{0.7}Ca_{0.3}MnO_3$ materials produces

a decrease in T_c correlating with increasing crystallite size.[78,82,99] Work with $La_{0.8}Ca_{0.2}MnO_3$ and $La_{0.6}Ca_{0.4}MnO_3$ nanoparticles similarly showed that an increase in sintering temperature created larger particles, which increased the maximum ΔS and T_c while decreasing the width of the MCE curve.[56,146] This has been attributed to tuning of the Griffith's phase.

In this section, chelating acid identity, sintering time, sintering temperature, cooling rate after sintering, starting concentrations of citric acid and PEG, reaction time, and starting volume of 4 M nitric acid were analyzed in pursuit of a set of parameters which create a product with the highest possible ΔS and most optimal T_c. A material with these optimized parameters was also synthesized and characterized using XRD, which showed a crystallite size of 150 nm. Assuming this material does not unexpectedly break the patterns seen in this section, it should have a high ΔS value and a T_c of ~280K.

4.2 Experimental Details

The parameters in the sol-gel synthesis described in section 1.4 were modified one or two at a time. Parameters tested were chelating acid identity, sintering time, sintering temperature, cooling rate after sintering, starting concentrations of citric acid and PEG, reaction time, and starting volume of 4M nitric acid (

Table 4.1). The magnetic properties, particle appearance, and crystal structures were then characterized for all the materials using PPMS, SEM, and XRD as described earlier in this work. All materials were compared to the standard material created with citric acid, sintered for 10 hours at 1000 °C (with the exception of the materials created with varying chelating acid species, which

were synthesized at 1100 °C) and cooled slowly, with a citric acid starting concentration of 0.26 M, a starting PEG 600 concentration of 0.08 M, and a starting nitric acid volume of 10 mL.

Table 4.1. *Synthesis parameters modified and the set points used.*

Parameter Changed	Set Points
Chelating acid identity	Citric acid, tannic acid, fumaric acid, oleic acid, oxalic acid
Sintering temperature	600C, 900C, 1000C, 1100C, 1200C
Sintering time	1 hr, 3 hr, 6 hr, 10 hr
Cooling rate after sintering	Slowly in tube furnace, quickly after removal from tube furnace
Citric acid concentration	0.05 M, 0.13 M, 0.26 M, 0.39 M
PEG concentration	0.04 M, 0.08 M, 0.16 M
4 M nitric acid volume	5 mL, 10 mL, 15 mL, 20 mL

4.3 Results and Discussion

4.3.1 Chelating Agent

The chelating acids chosen were citric acid, tannic acid, fumaric acid, oleic acid, and oxalic acid (**Figure 4.1**). Literature states an α-hydroxycarboxylic acid is needed. An α-hydroxycarboxylic acid promotes chelation as well as the nucleophilic attack necessary for the esterification step to occur, and multiple hydroxyl groups after chelation (a polybasic chelated complex) allows for effective cross-linking.[90,147] Citric acid both is an α-hydroxycarboxylic acid and is polybasic. Tannic acid can be polybasic, to an extreme degree given the large quantity of available OH groups but

is not α-hydroxycarboxylic. Fumaric acid and oxalic acid are both polybasic, but not α-hydroxycarboxylic acids. Oleic acid is neither polybasic nor an α-hydroxycarboxylic acid.

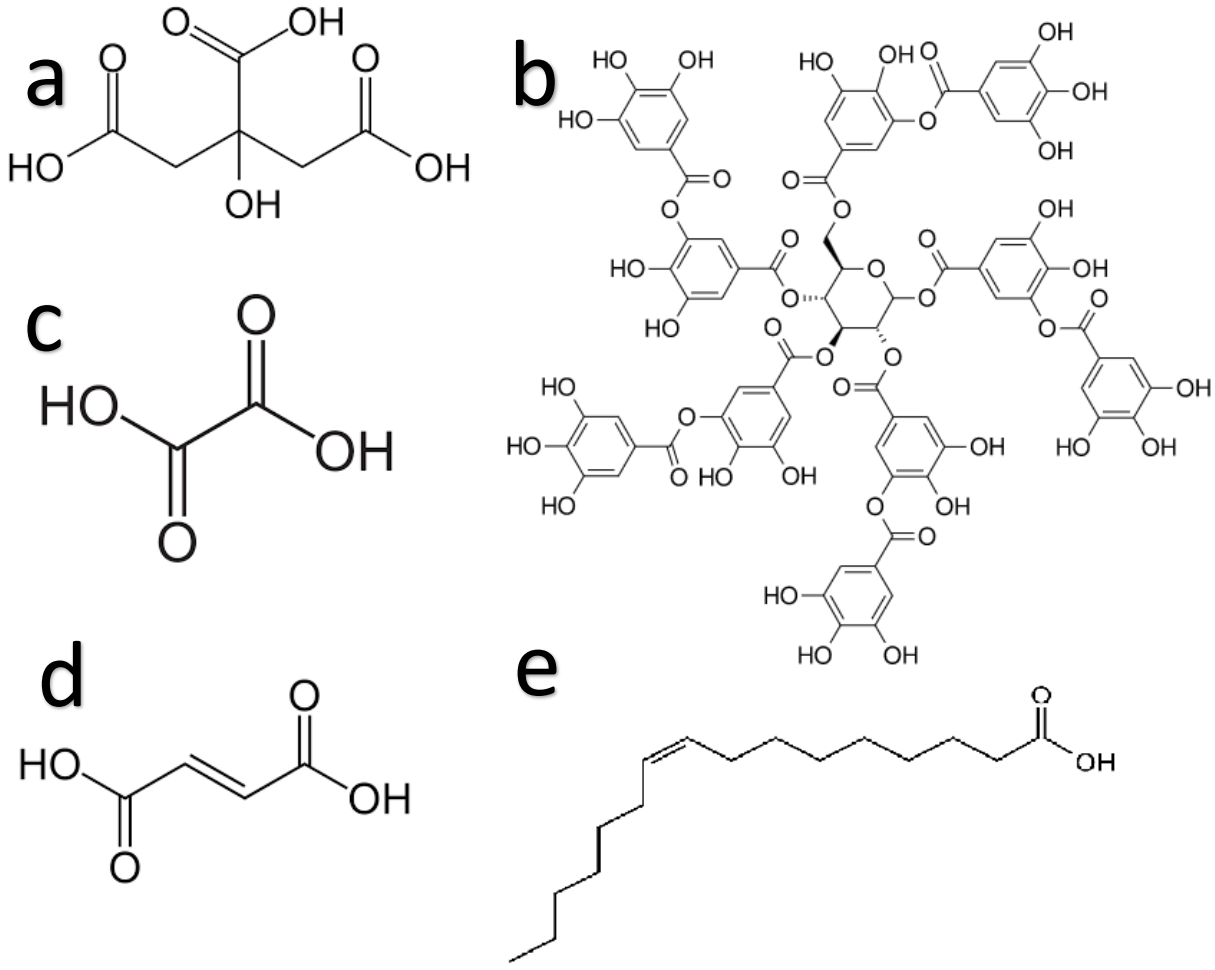

Figure 4.1 *Chemical structures of (a) citric acid, (b) tannic acid, (c) oxalic acid, (d) fumaric acid, and (e) oleic acid.*

Regardless of the chelating agent used, all materials are phase pure (**Figure 4.2**), though the oleic acid and oxalic acid materials show significant shifts in their lattice parameters (**Figure 4.2**). Oleic acid has the smallest a and b lattice parameters and the largest c parameter as well as the smallest maximum ΔS; similarly, oxalic acid has smaller a and b lattice parameters and a larger c

lattice parameter than the others and has the second smallest ΔS value. The comparably smaller deviations between the lattice parameters of the other three materials do not directly correlate to ΔS or T_c. This implies that small differences in the lattice parameters have little effect on the magnetic properties. This correlates well with the sodium substitution work which suggested that very small changes in the crystal structure were less important to the T_c value, and of only minimal importance to the orbital overlap, exchange energies and subsequent ΔS value. Crystallite sizes were 147.0 nm for citric acid, 125.8 nm for tannic acid, 87.6 nm for fumaric acid, 62.4 nm for oxalic acid, and 45.9 nm for oleic acid. Crystallite sizes appear to change independent of whether the acid is polybasic, though citric acid, the only α-hydroxycarboxylic acid tested, lead to the largest crystallites.

Table 4.2 *Lattice parameters for materials synthesized with each of the tested chelating agents. Error is ±0.002 Å. Oxalic acid and oleic acid show significant shifts in all three lattice parameters while all the others remain comparable.*

Material	a (Å)	b (Å)	c (Å)
Tannic	5.455	7.686	5.442
Citric	5.457	7.687	5.434
Fumaric	5.461	7.688	5.442
Oxalic	5.430	7.693	5.462
Oleic	5.426	7.745	5.478

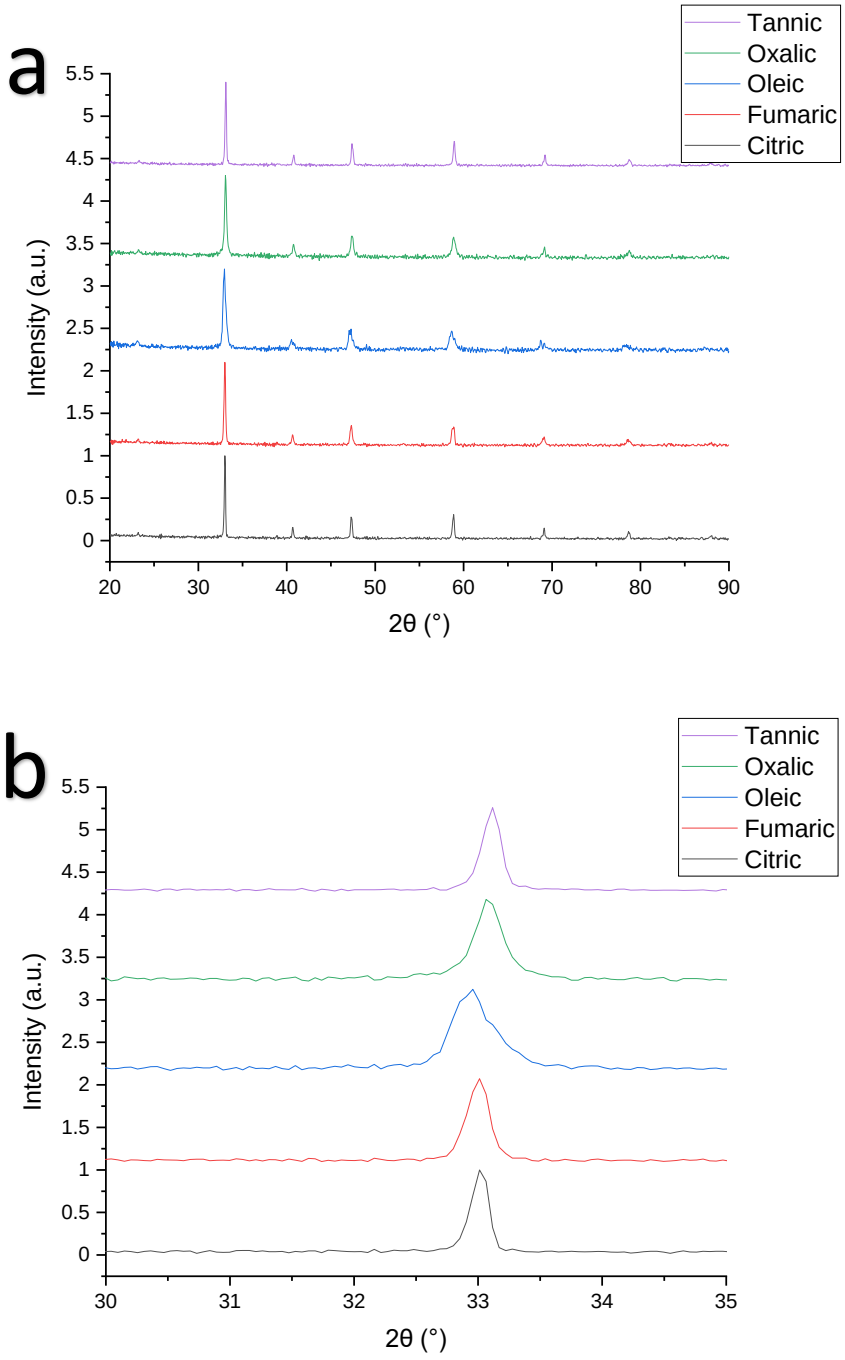

Figure 4.2 *(a) Full XRD patterns for $La_{0.60}Ca_{0.40}MnO_3$ nanoparticles synthesized with various chelating agents. (b) XRD peak at 2T≈33 showing a slight shift to the left and appearance of asymmetry in the oleic acid sample.*

All materials have a T_c value of ~270K, with only the citric acid material being slightly higher at ~272K, consistent with typical T_c values for $La_{0.60}Ca_{0.40}MnO_3$ (**Figure 4.3a**).[3,51,56,97,134] The working temperature range, ΔT_{FWHM}, is also comparable across the materials at ~33 K. Only the maximum ΔS changes when the chelating agent changes (**Figure 4.3b**). The oleic acid M(T) curve has a far less sharp phase transition than the other four materials leading to a much smaller MCE peak. Maximum ΔS values are 4.1 J/kgK for citric acid, 3.7 J/kgK for tannic acid, 3.1 J/kgK for fumaric acid, 2.6 J/kgK for oxalic acid, and 1.1 J/kgK for oleic acid. Although some work has suggested a connection between crystallite size and T_c,[56,78,83] the varying crystallite sizes (calculated using the Scherrer calculator in X'Pert HighScore) seen in these materials only lead to a change in T_c with a significant increase in crystallite size (**Figure 4.3c**).

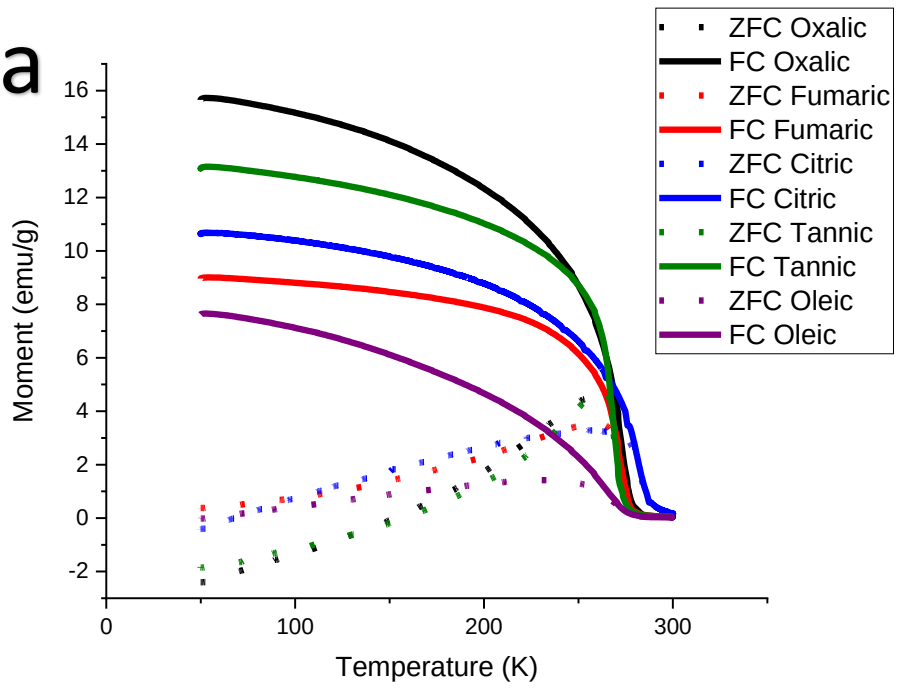

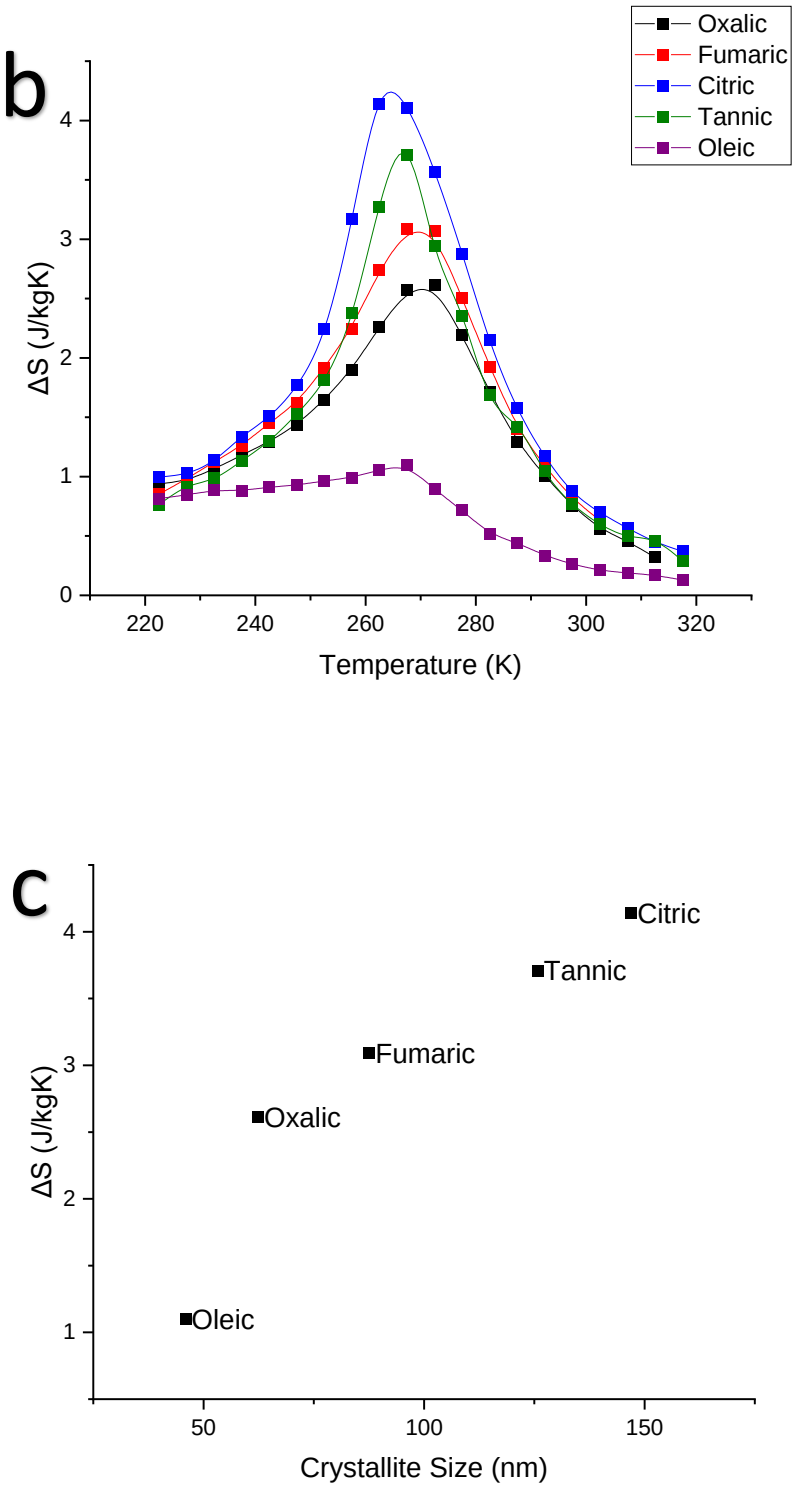

Figure 4.3 *(a) MT and (b) MCE curves for $La_{0.60}Ca_{0.40}MnO_3$ materials synthesized with various chelating agents. (c) Plot of crystallite size vs. maximum ΔS for samples made with various chelating acids which demonstrates the direct relationship between the two variables.*

These crystallite sizes are supported by the collected SEM images (**Figure 4.4**). The images also show a clear surface texture and particle shape difference when comparing the citric, tannic, and fumaric samples with the oxalic and oleic samples. The oxalic and oleic samples are much more spherical than the other materials, which would imply fewer easy axes and thus different anisotropy. The citric acid sample in particular has very rigid edges and even the presence of ridges or grooves on the surface of the particles. This morphological difference – shifting from hard, rigid edges to rounded edges – correlates with the decreasing ΔS values which could potentially be attributed to the change in anisotropy and number of easy axes.

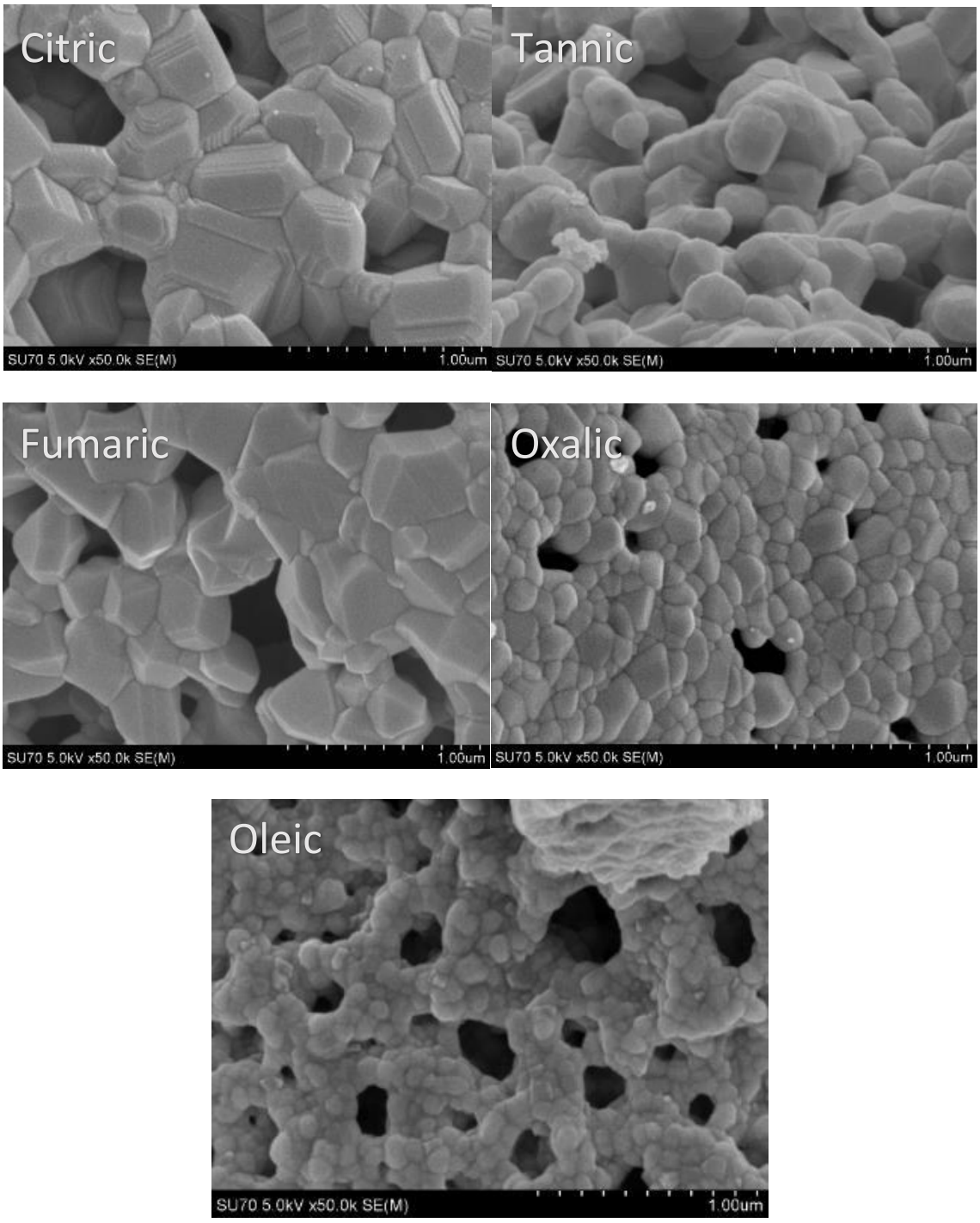

Figure 4.4 *SEM images for materials synthesized with various chelating agents.*

4.3.2 Sintering Temperature

In previous literature, the only systematic study of sintering temperature for $La_{0.60}Ca_{0.40}MnO_3$ materials tested temperatures of 700 °C, 800 °C, 900 °C, and 1000 °C but did not proceed to higher temperatures, which have been known to appear elsewhere in the literature.[56,140,148] To further examine the effects of the nature of the sintering stage, the sintering temperatures were extended up to 1200 °C, with 600 °C, 900 °C, and 1000 °C repeated for comparison. The sample prepared with a 600 °C sintering temperature shows an XRD pattern with significantly more noise than the others, suggesting that sintering temperatures this low create less crystalline materials (**Figure 4.5**). Crystallite sizes for the sintering temperature samples are 15.8 nm for 600C, 97.3 nm for 900C, 58.3 nm for 1000C, 147.0 for 1100C, and 176.9 for 1200C. The 900C and 1000C syntheses were repeated a second time in order to verify reproducibility of crystallite sizes and phase purity. No significant deviation was observed for either of these materials. With the exception of the 1000C material, these crystallite sizes increase with increasing sintering temperature (**Figure 4.6**). The 900C material shows a significant shift to the left in the XRD pattern, which suggests a difference in the lattice parameters for that material.

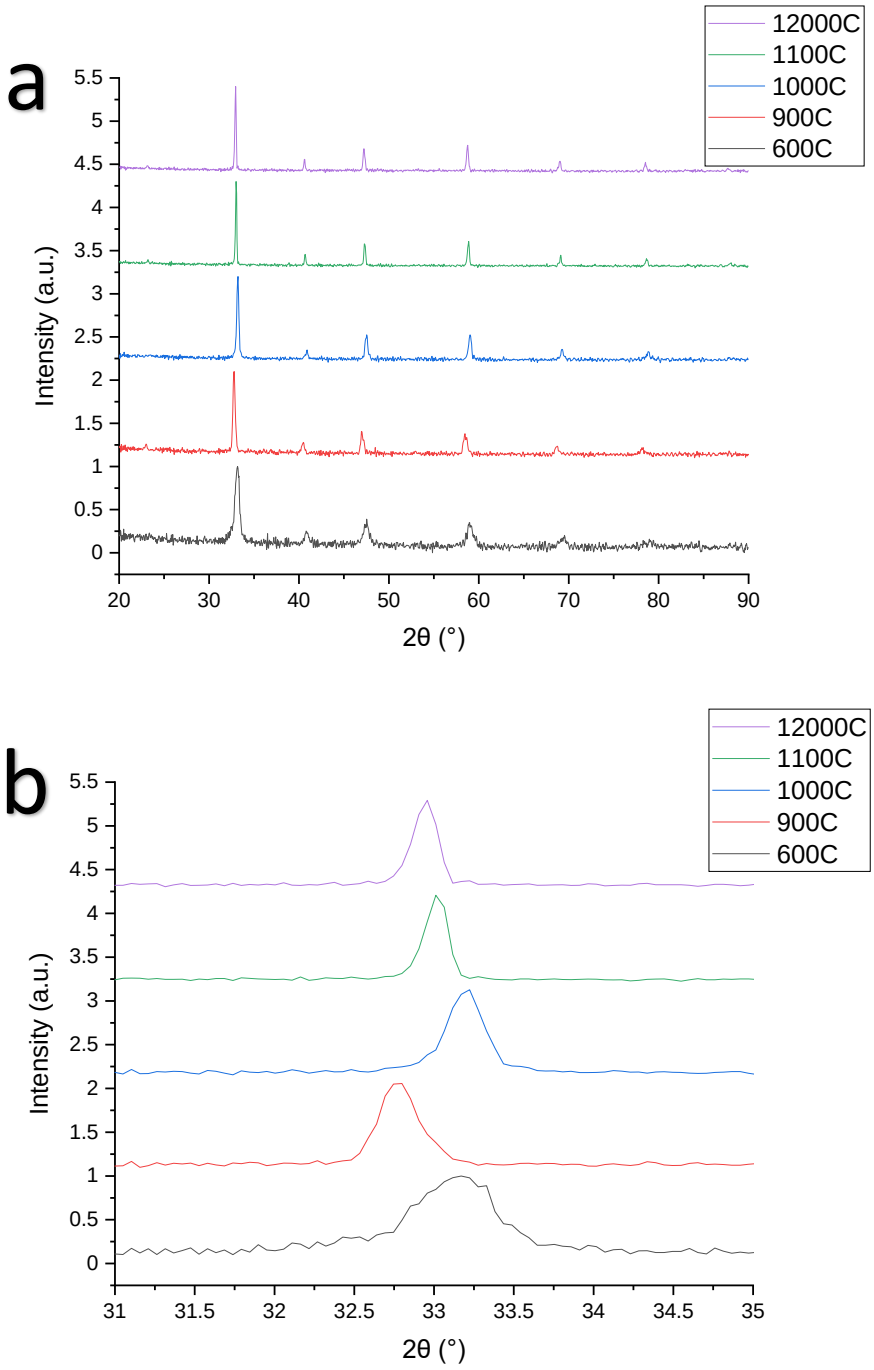

Figure 4.5 *XRD patterns, both full (a) and centered on the peak at 2ϑ≈33° (b), for the materials created at increasing sintering temperatures. All patterns show excellent crystallinity. The 600C sample has the noisiest pattern and there is a shift to the left observed in the 900C pattern.*

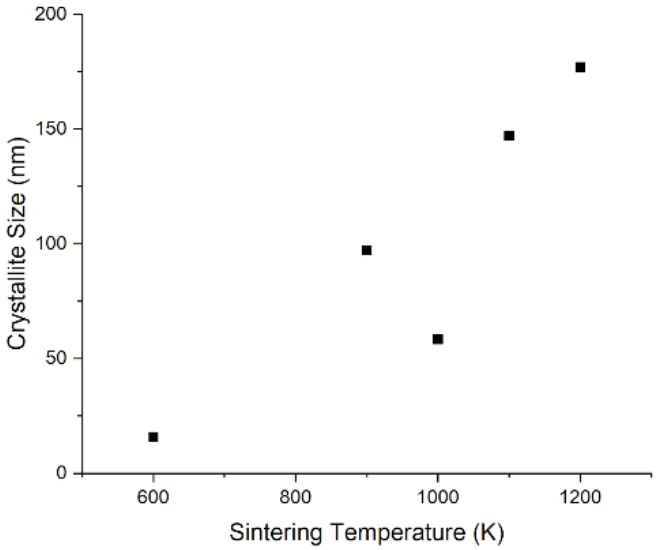

Figure 4.6 *Plot of sintering temperature and crystallite size showing an increase of crystallite size with increasing temperature with the exception of the material synthesized at 1000C.*

The M(T) curves collected suggest that an increase in sintering temperature leads to an increase in crystallite size, with the exception of the 900C material which has a larger than expected crystallite size and T_c. A previous study suggested that increasing crystallite size through sintering temperature (analyzing sintering temperature of 700 K to 1000 K) increased T_c. The T_c changes in that work are pretty minimal, however (only a 5 K difference from the lowest to the highest) while the crystallite size changes are more dramatic (a 180 nm difference between the largest and the smallest crystallites).[56] The 900C and 1000C material created in the present work have T_c values comparable to the 270 K and 272 K values for the materials in the cited work created at the same sintering temperatures and the jump to a T_c of ~280K for the 1100C and 1200C materials suggests that perhaps a minimum increase in crystallite size exists in order for an increase in T_c to be observed. This fits with the strontium substitution work where there was

a large difference between the crystallite sizes of the LCMO and LSMO parent compounds which can account for the lack of change in T_c; it also fits with the findings for the chelating agent work, where the crystallite sizes were comparatively tightly grouped and no change in T_c was observed. The maximum ΔS, however, clearly increases with even the small increases in crystallite size, which suggests that ΔS is far more sensitive to changes in crystallite size than the Curie Temperature. Maximum ΔS values are 0.37 J/kgK (600C), 5.6 J/kgK (900C), 1.8 J/kgK (1000C), 4.1 J/kgK (1100C), and 5.1 J/kgK (1200C). Deviation from the Curie-Weiss law in all five materials implies the presence of a Griffith's phase. (**Figure 4.7**)

The SEM images collected for the sintering temperature change materials (**Figure 4.8**) show that the 600C material is composed of very small particles. All other samples have significantly larger particles and an appreciable discrepancy between particle size and crystallite size. There are therefore multiple crystallites present in each particle. Given these results, it would appear that the ideal sintering temperature is 900 °C, where an unusual increase in crystallite size and ΔS beyond what would be expected based on the emergent pattern has been observed.

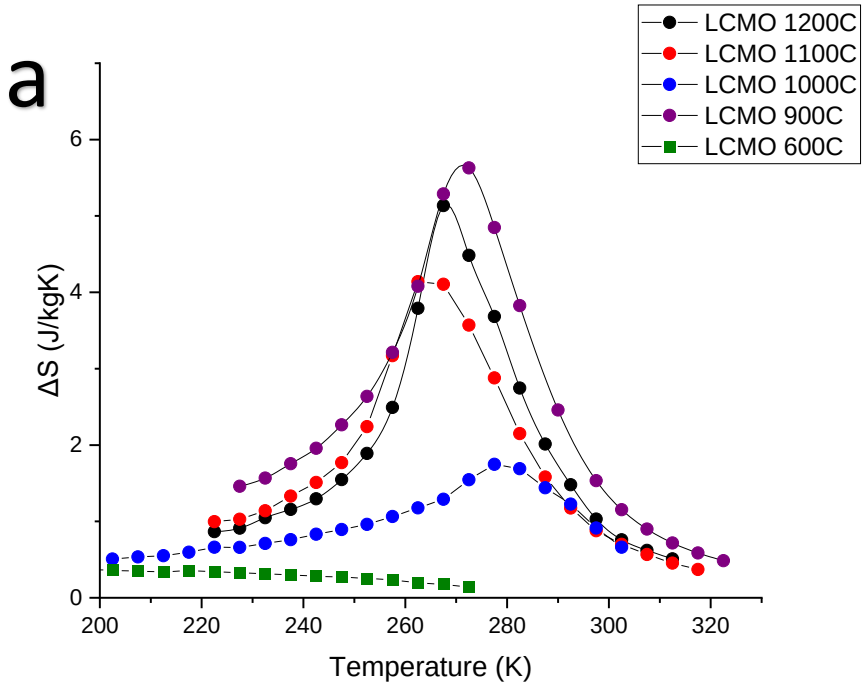
a
LCMO 1200C
LCMO 1100C
LCMO 1000C
LCMO 900C
LCMO 600C
ΔS (J/kgK)
Temperature (K)
0
2
4
6
200
220
240
260
280
300
320

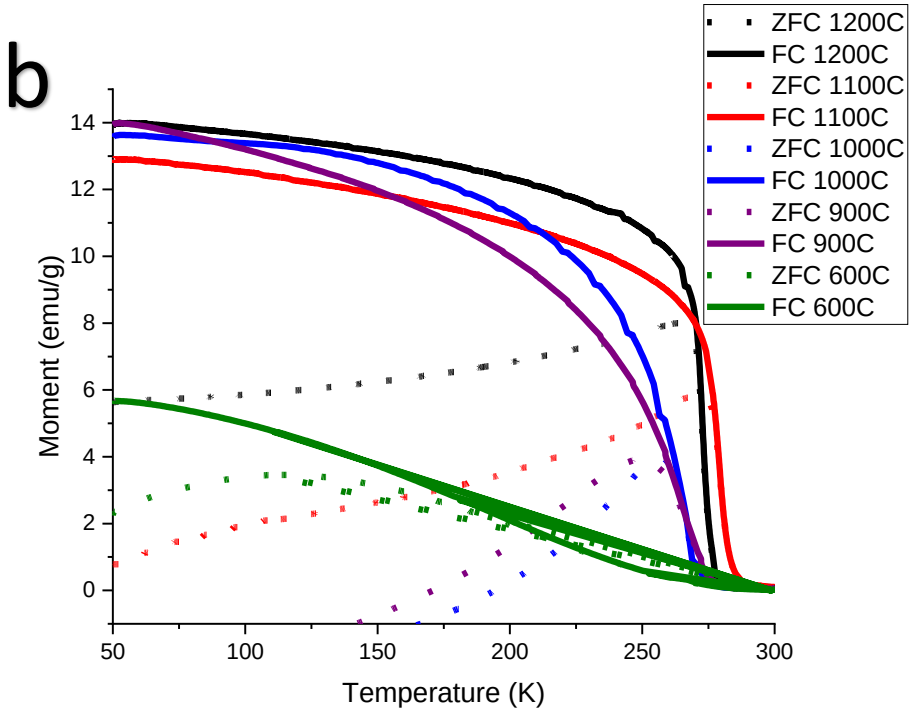
b
ZFC 1200C
FC 1200C
ZFC 1100C
FC 1100C
ZFC 1000C
FC 1000C
ZFC 900C
FC 900C
ZFC 600C
FC 600C
Moment (emu/g)
Temperature (K)
0
2
4
6
8
10
12
14
50
100
150
200
250
300

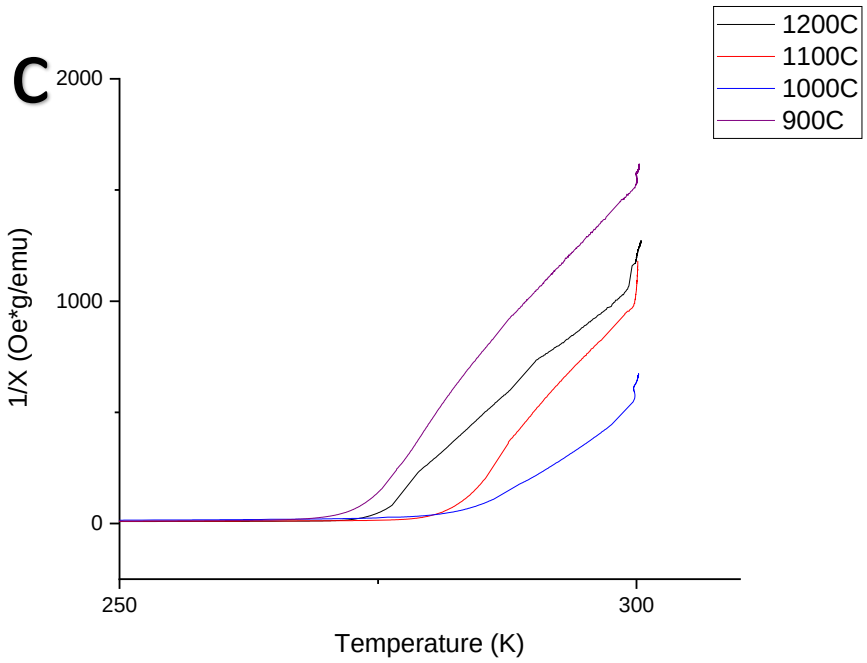

Figure 4.7 *MCE (a), MT (b), and 1/X (c) curves for the sintering temperature materials.*

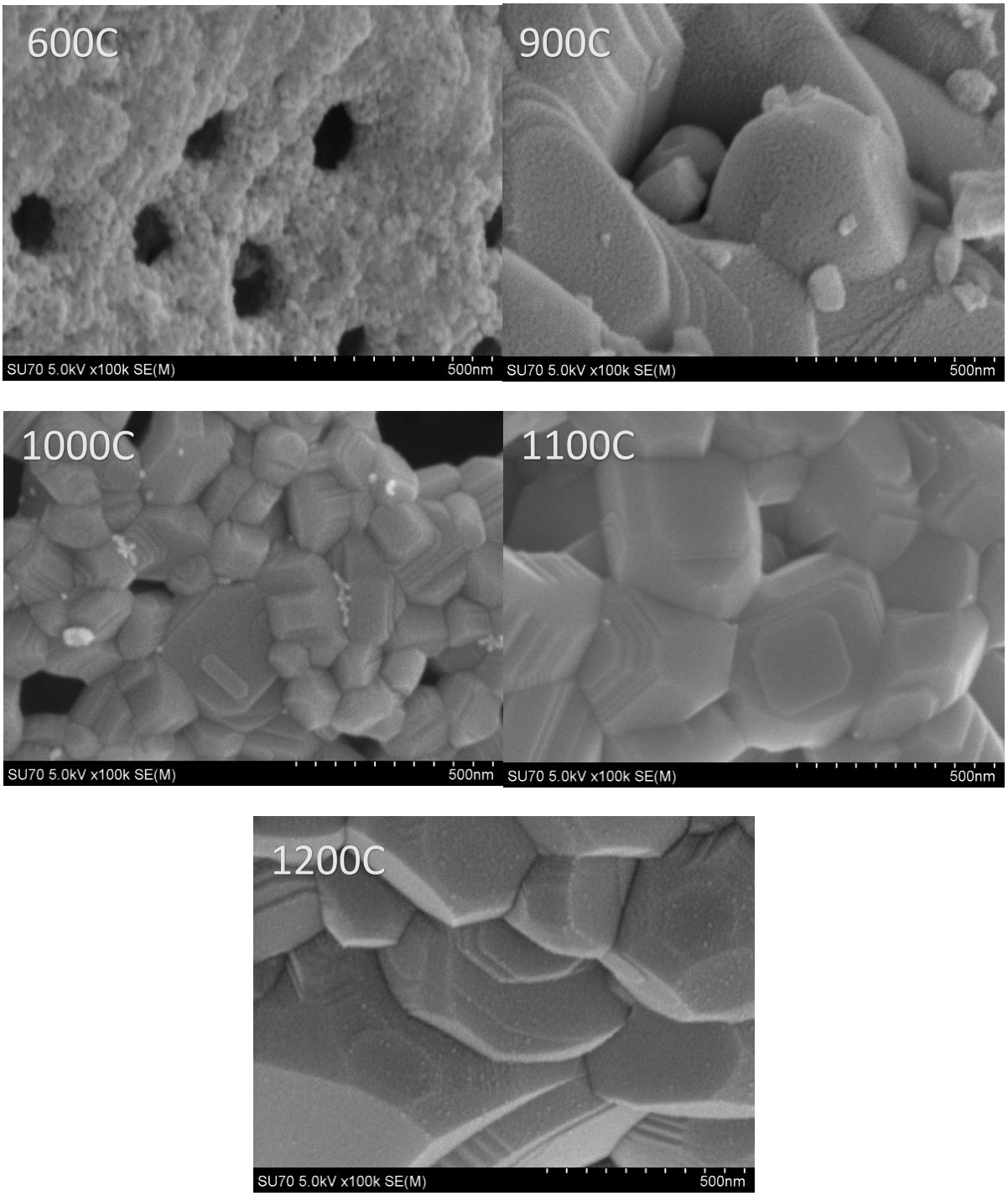

Figure 4.8 *SEM images for materials synthesized at varying sintering temperatures showing an increase in particle size as sintering temperature was increased.*

4.3.3 Sintering Time and Cooling Rate

Sizes and ΔS values for the samples cooled quickly are 43.6 nm and 1.9 J/kgK for r1hr, 41.5 nm and 2.0 J/kgK for r3hr, and 222.4 nm and 3.9 J/kgK for r6hr. Samples cooled slowly have crystallite sizes and ΔS values of 67.3 nm and 1.3 J/kgK for sp1hr, 86.7 nm and 4.8 J/kgK for sp3hr, and 65.3 nm and 2.2 J/kgK for sp6hr (**Figure 4.9**). The sp10hr sample is the same as the 1000C material discussed in the sintering temperature section above. The two materials with the furthest shift to the left in the XRD patterns and the largest crystallite sizes – sp3hr, and r6hr – have the highest maximum ΔS values (**Table 4.3**).

Congruent with the sintering temperature analysis discussed above, very small changes in crystallite size appear to have little to no effect on T_c. Only the very largest crystallites – r6hr and sp3hr – have an appreciably different T_c. The MCE curves are maximized after sintering for 6 hours when the materials are cooled quickly, but after only 3 hours when cooled slowly. This discrepancy may be attributed to the samples which are cooled slowly continuing to effectively sinter until the temperature is as low as 600 °C, as suggested by the data from varying the sintering temperature section above (**Figure 4.10**). This may increase total sintering time for the sp3hr sample to a duration comparable to the sp6hr sample. Generally speaking, the greater the maximum ΔS, the narrower the MCE peak and working temperature range. This fits with previous work suggesting larger crystals are less affected by the contribution of the Griffith's phase in the material. The presence of a Griffith's phase is confirmed in all materials by a deviation from the Curie-Weiss law near T_c (**Figure 4.11**). The sp1hr, sp6hr, r1hr, r6hr, and 600C materials appear fairly spherical in the SEM images (**Figure 4.12**). The other materials have much more rigid, rectangular attributes, with the 1000C and sp3hr materials possessing the most rectangular

shape. This is congruent with the chelating agent results suggesting that less spherical particles are more ideal, perhaps as a result of the differing magnetic anisotropy between spherical and non-spherical particles. The ideal sintering duration is 3 hours with a slow cooling rate.

Table 4.3 *Crystallite sizes, ~33° peak position, maximum ΔS, and T_c values for materials synthesized with varying sintering times and cooled either slowly in the tube furnace or promptly removed to cool in air.*

Sample	Crystallite Size (nm)	~33° Peak Position (°)	ΔS (J/kgK)	T_c (K)
sp1hr	67.3	33.17	1.28	260
sp3hr	86.7	33.17	4.76	275
sp6hr	65.3	32.96	2.23	255
sp10hr	58.3	33.12	1.75	280
r1hr	43.6	33.28	1.86	260
r3hr	41.5	33.22	2.01	255
r6hr	222.4	33.01	3.94	275

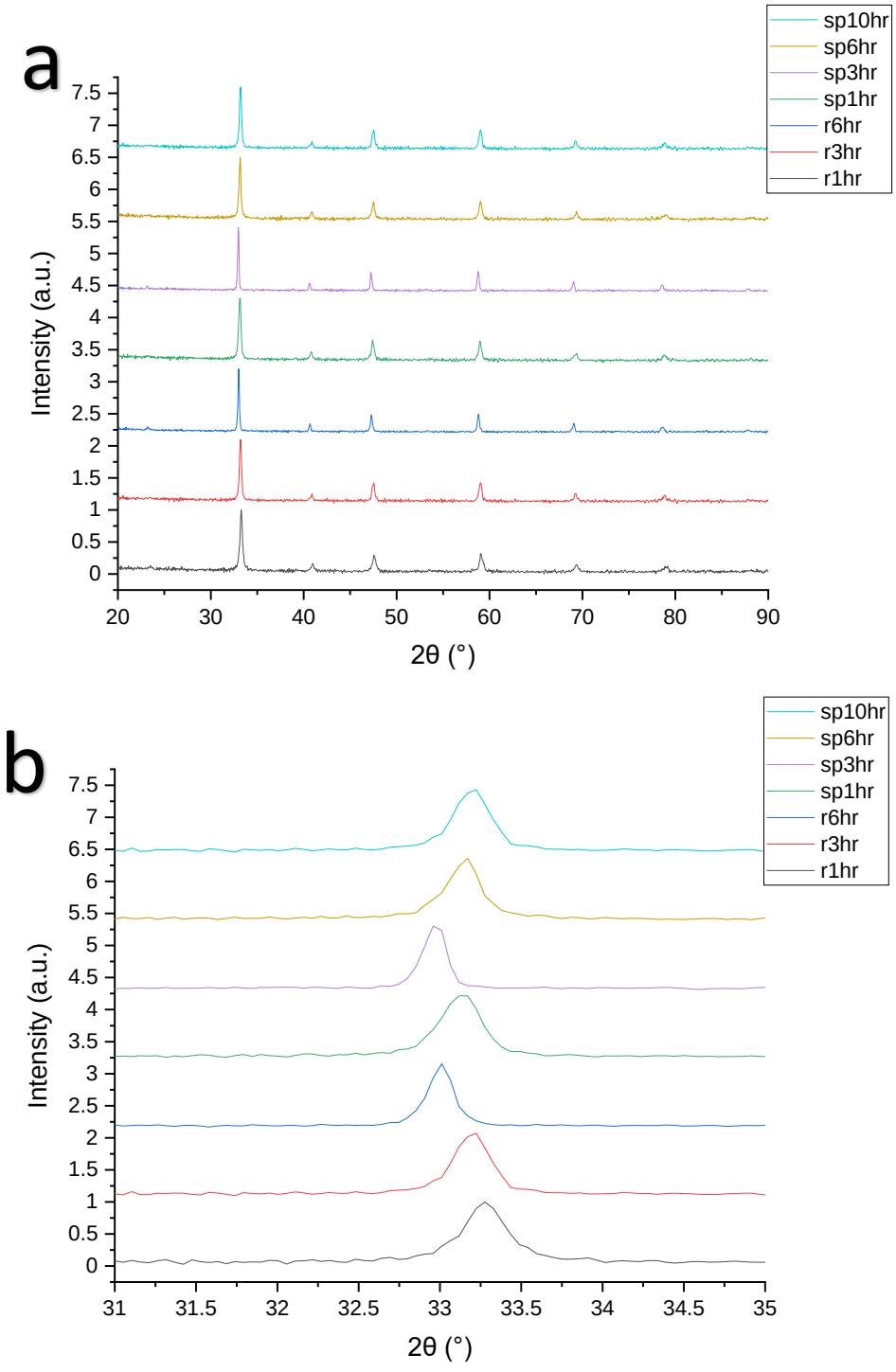

Figure 4.9 *XRD patterns for varying sintering times and cooling rates.*

a

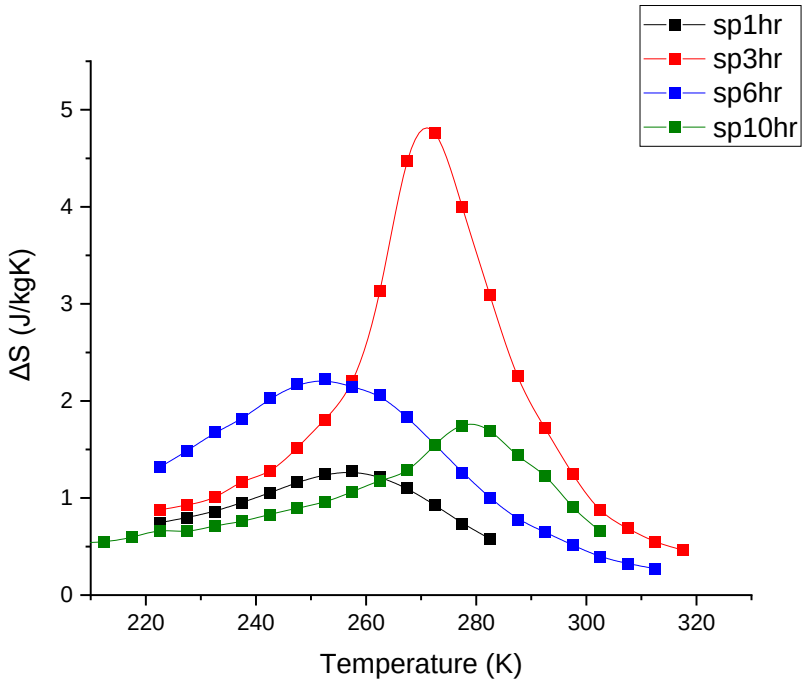
sp1hr
sp3hr
sp6hr
sp10hr
ΔS (J/kgK)
Temperature (K)
0
1
2
3
4
5
220
240
260
280
300
320

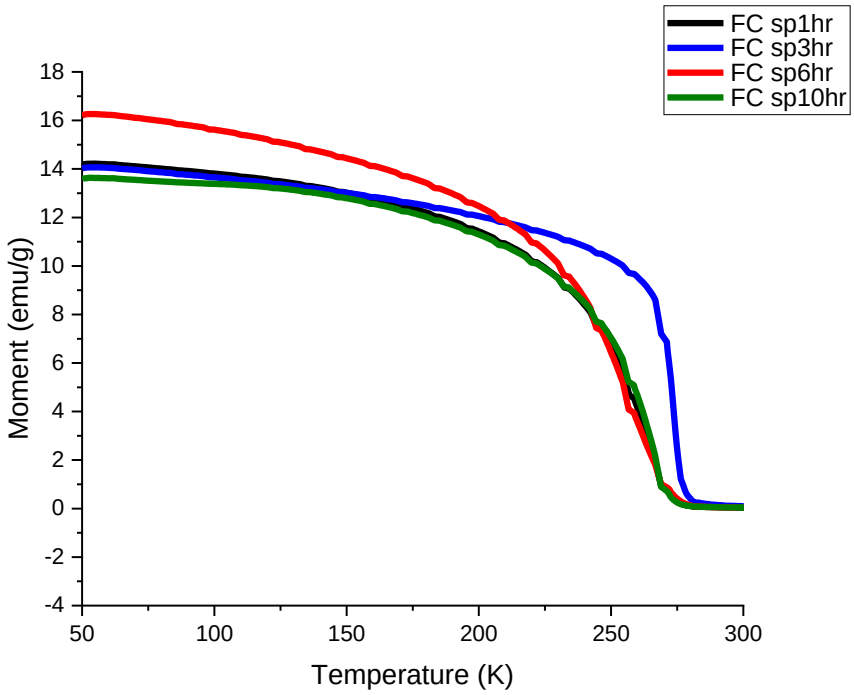
FC sp1hr
FC sp3hr
FC sp6hr
FC sp10hr
Moment (emu/g)
Temperature (K)
-4
-2
0
2
4
6
8
10
12
14
16
18
50
100
150
200
250
300

b

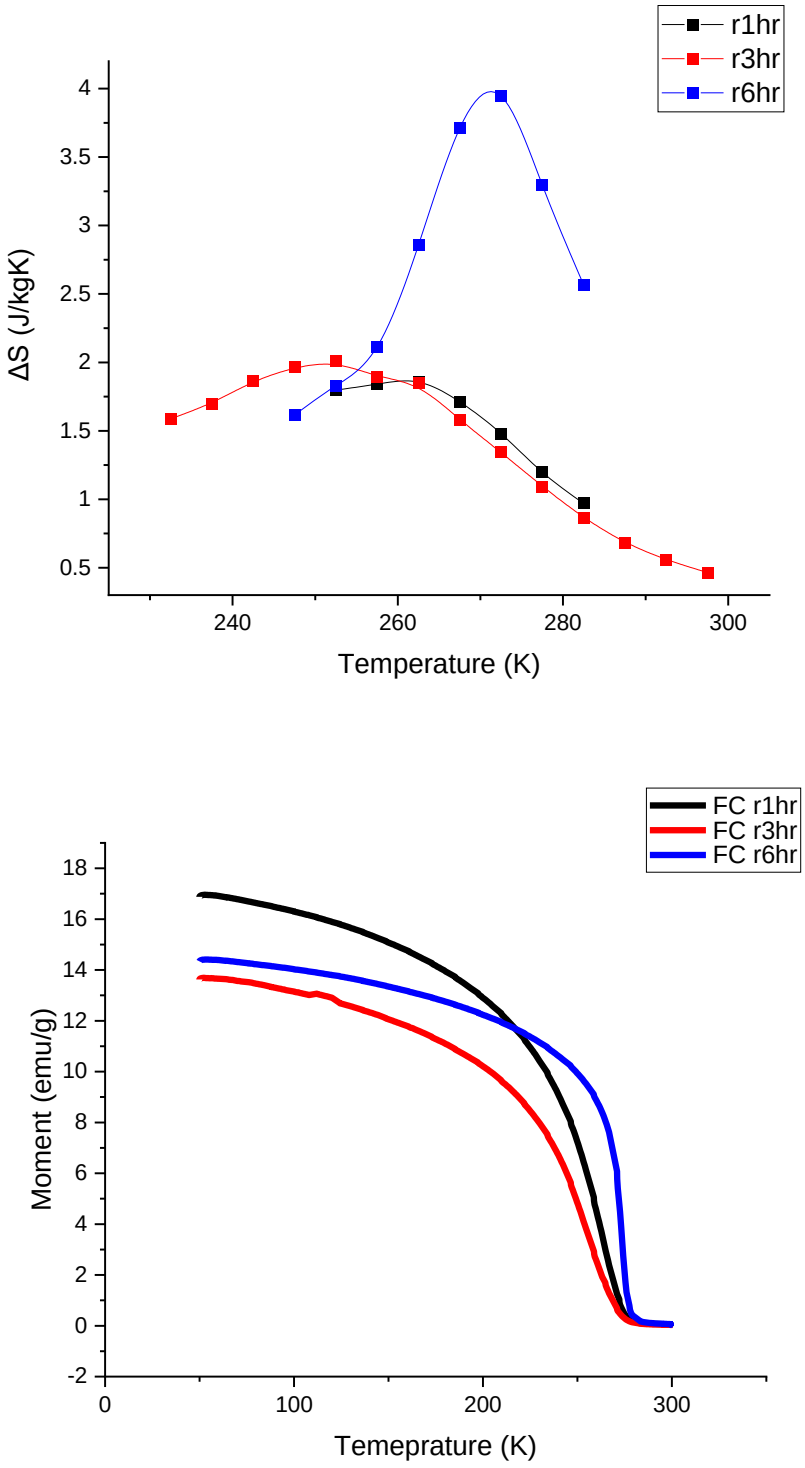

Figure 4.10 *MT and MCE curves for materials made with varying sintering times with a slow cooling rate (a), and varying sintering times with a fast cooling rate (b).*

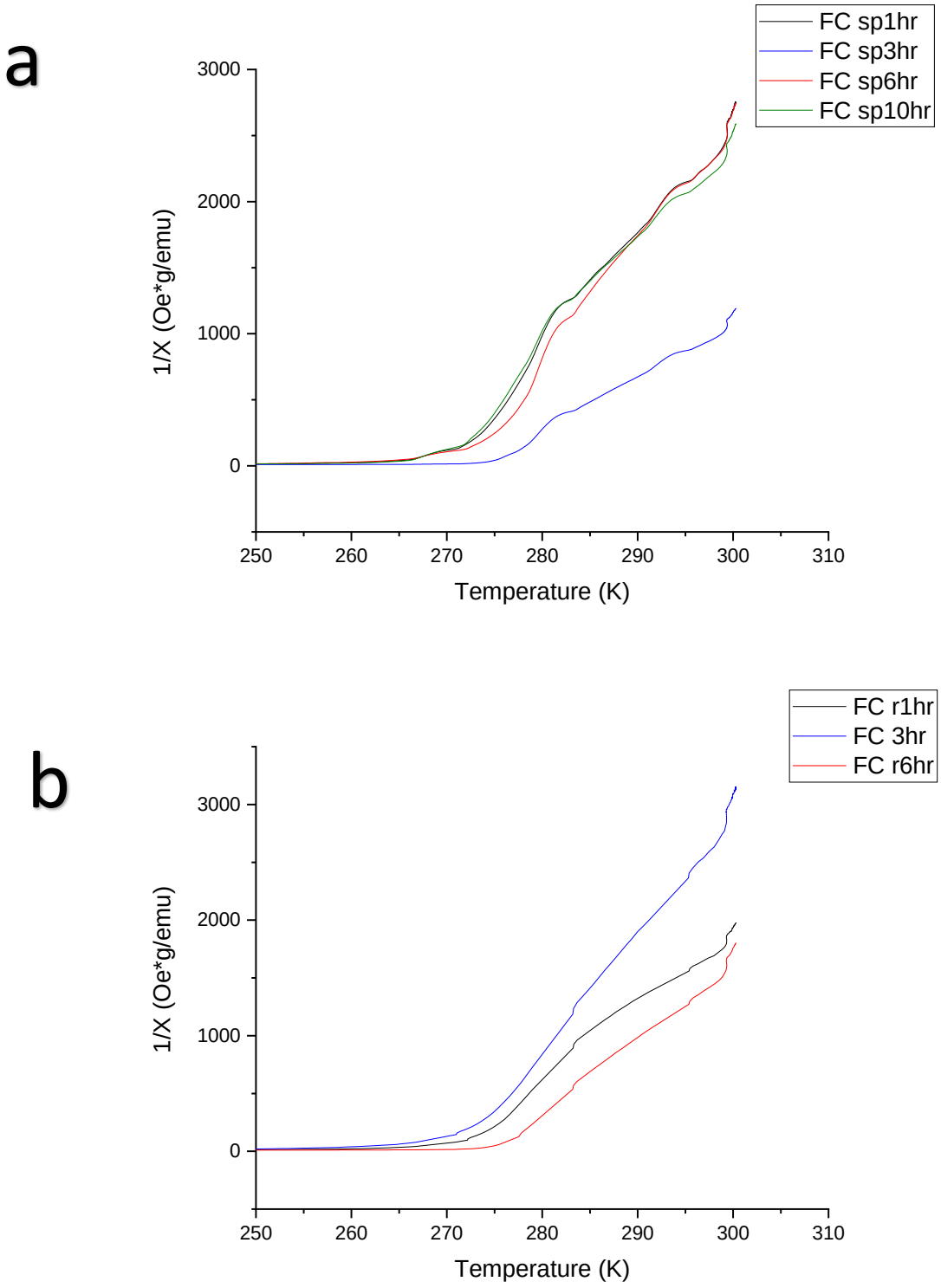

Figure 4.11 *Magnetic Susceptibility, 1/X, for materials synthesized with various sintering times and cooling rates. The deviation from the Curie-Weiss law seen in all materials is indicative of the presence of a Griffiths phase.*

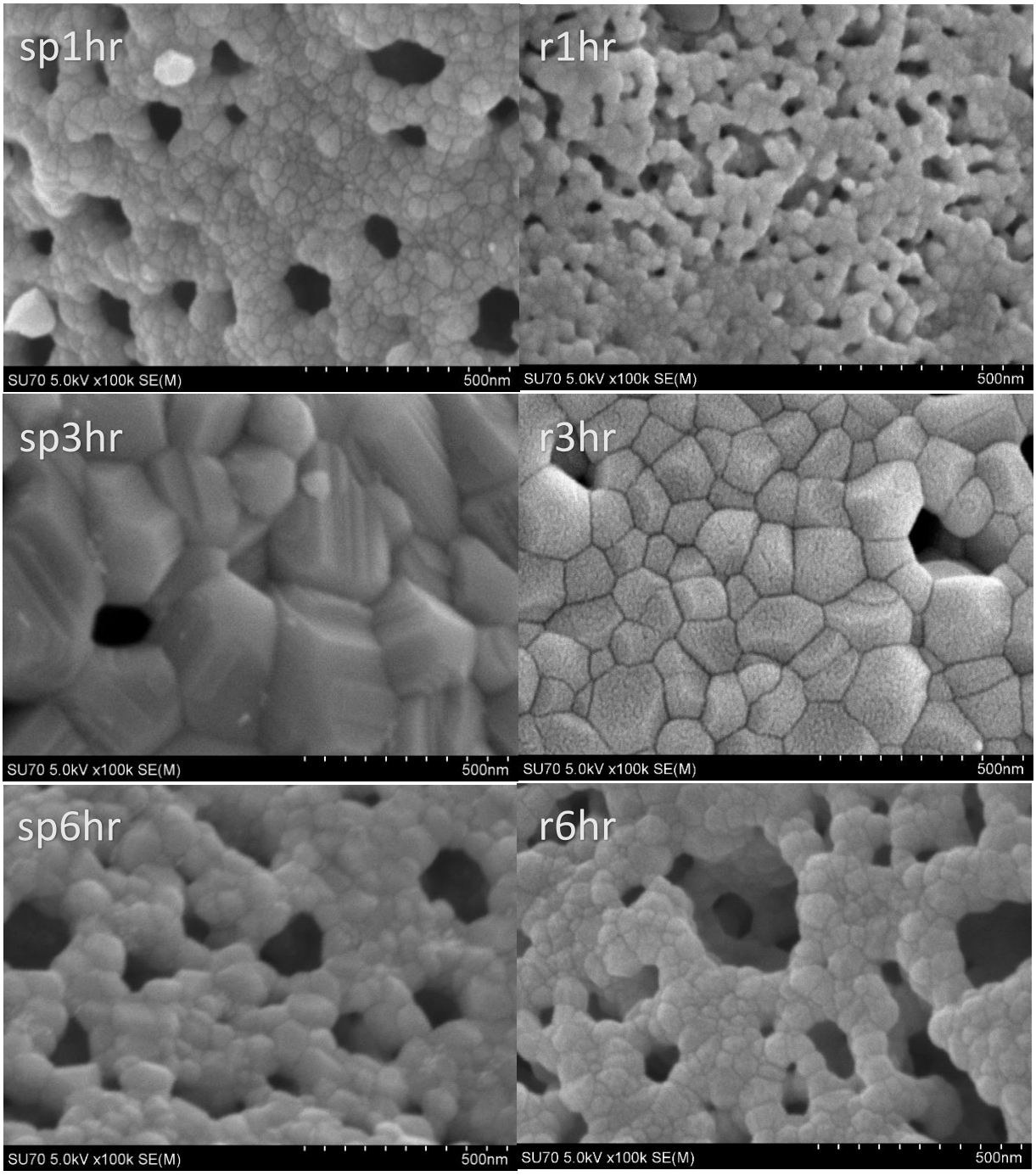

Figure 4.12 *SEM images for materials cooled slowly (left column) and quickly (right column) after being sintered for various periods of time. The 1000C material serves as the sp10hr sample.*

4.3.4 CA Starting Concentration

All starting concentrations of citric acid (CA) produced crystalline, phase-pure nanoparticles (**Figure 4.13**), with the exception of a starting concentration of 0.05 M. The crystallite size fluctuates as CA concentration is increased. Crystallite sizes are 21.7 nm, 177.0 nm, 58.3 nm, and 125.8 nm for the 0.05M, 0.13M, 0.26M, and 0.39M materials, respectively. As predicted by the sintering temperature work, the 0.23M material has the highest ΔS value due to its larger crystallite size.

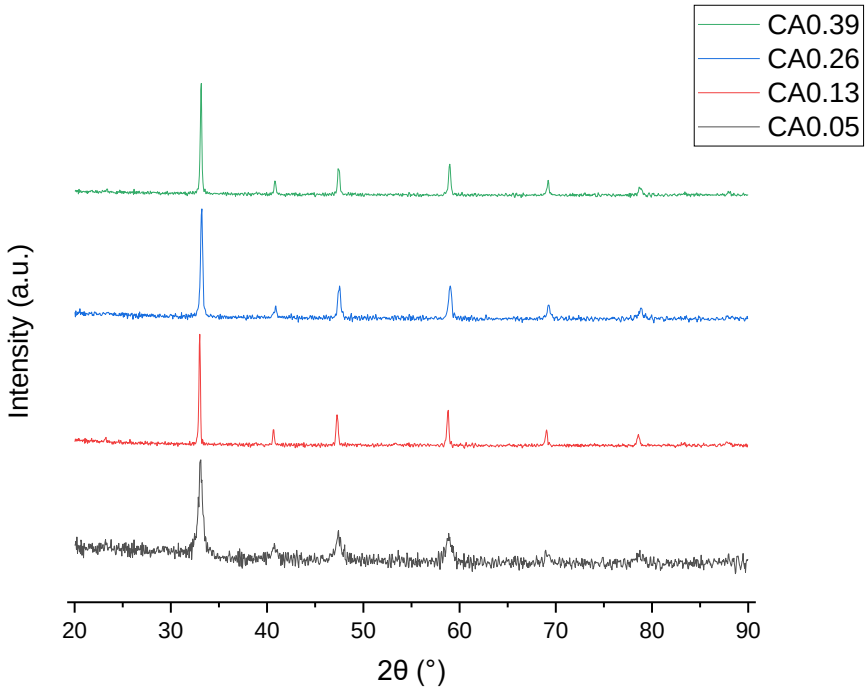

Figure 4.13 *XRD patterns for the materials created with increasing concentrations of citric acid.*

In these materials, T_c decreases along with ΔS as crystallite size decreases (**Figure 4.15**) which supports the findings of the chelating agent and sintering temperature sections above as well as findings presented in the literature.[56] The SEM images show particle sizes congruent with

crystallite sizes for all but the 0.26M material, which shows particles much larger than the crystallite sizes measured (**Figure 4.14**). That is also the only material with particles that are not particularly spherical. It can be surmised that the ideal starting concentration of citric acid is 0.13 M, which produces both the greatest value of ΔS and one of the highest values of T_c. ΔS and T_c values for each starting concentration are 0.45 J/kgK and 286 K for the 0.05M sample, 4.9 J/kgK and 288 K for the 0.13M sample, 0.99 J/kgK and 270 K for the 0.26M sample, and 2.7 J/kgK and 283 K for the 0.39M sample. The 0.26M and 0.05M materials have the most different crystallite sizes (considerably smaller than the others) as well as the most noticeably different M(T) curves. The 0.26M sample has a T_c difference which is congruent with the findings relating T_c and crystallite size discussed above. While the T_c for the 0.05 M sample is higher than expected given its much lower crystallite size, the shape of the curve and value of dM/dT suggest that an additional factor is at work, perhaps related to the homogeneity of the material created as such a low concentration of the chelating agent could have prevented the metal ions from being well-dispersed in the gel, leading to a less phase pure and less crystalline product.

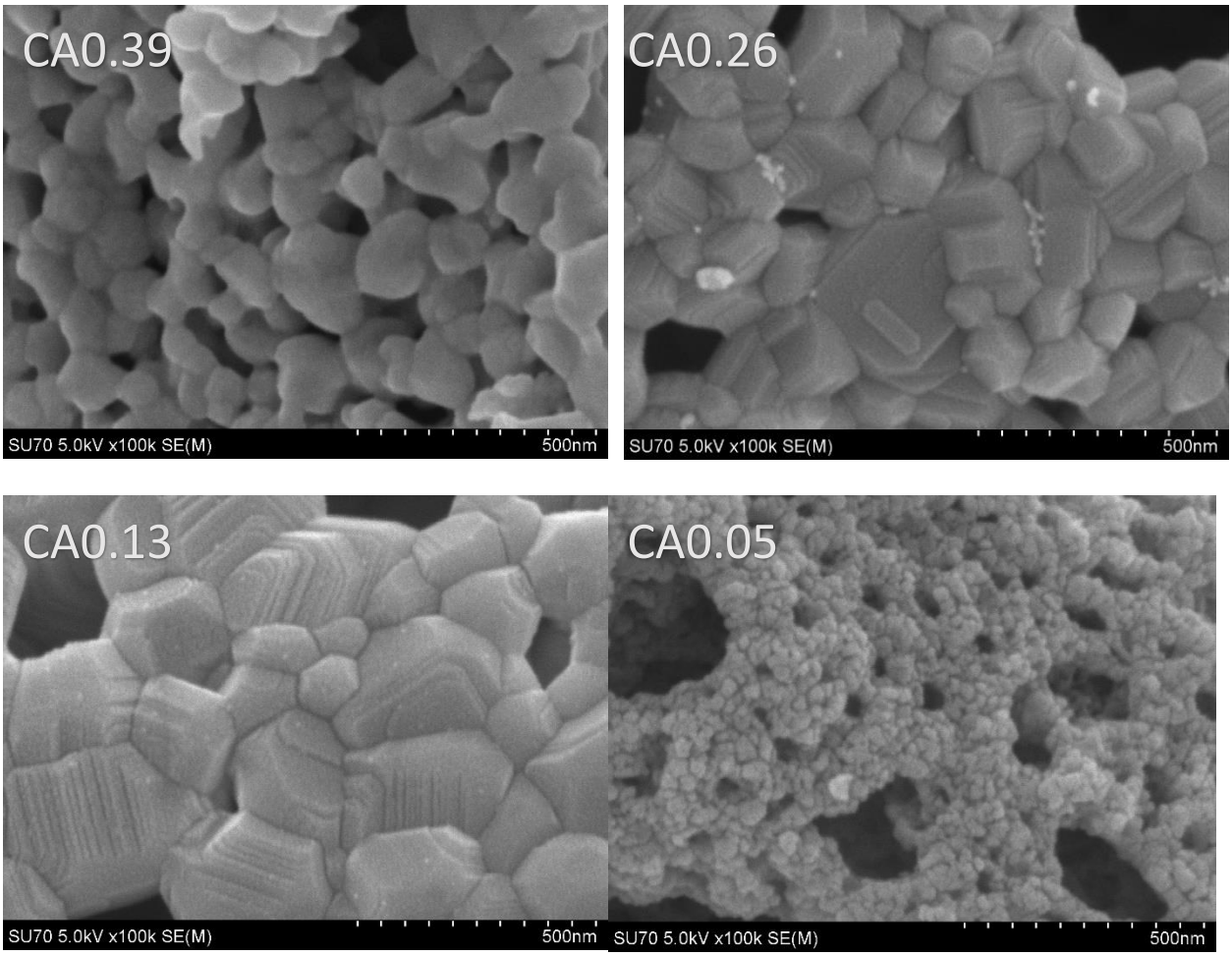

Figure 4.14 *SEM images for materials created to examine the effect of altering the starting concentration of citric acid.*

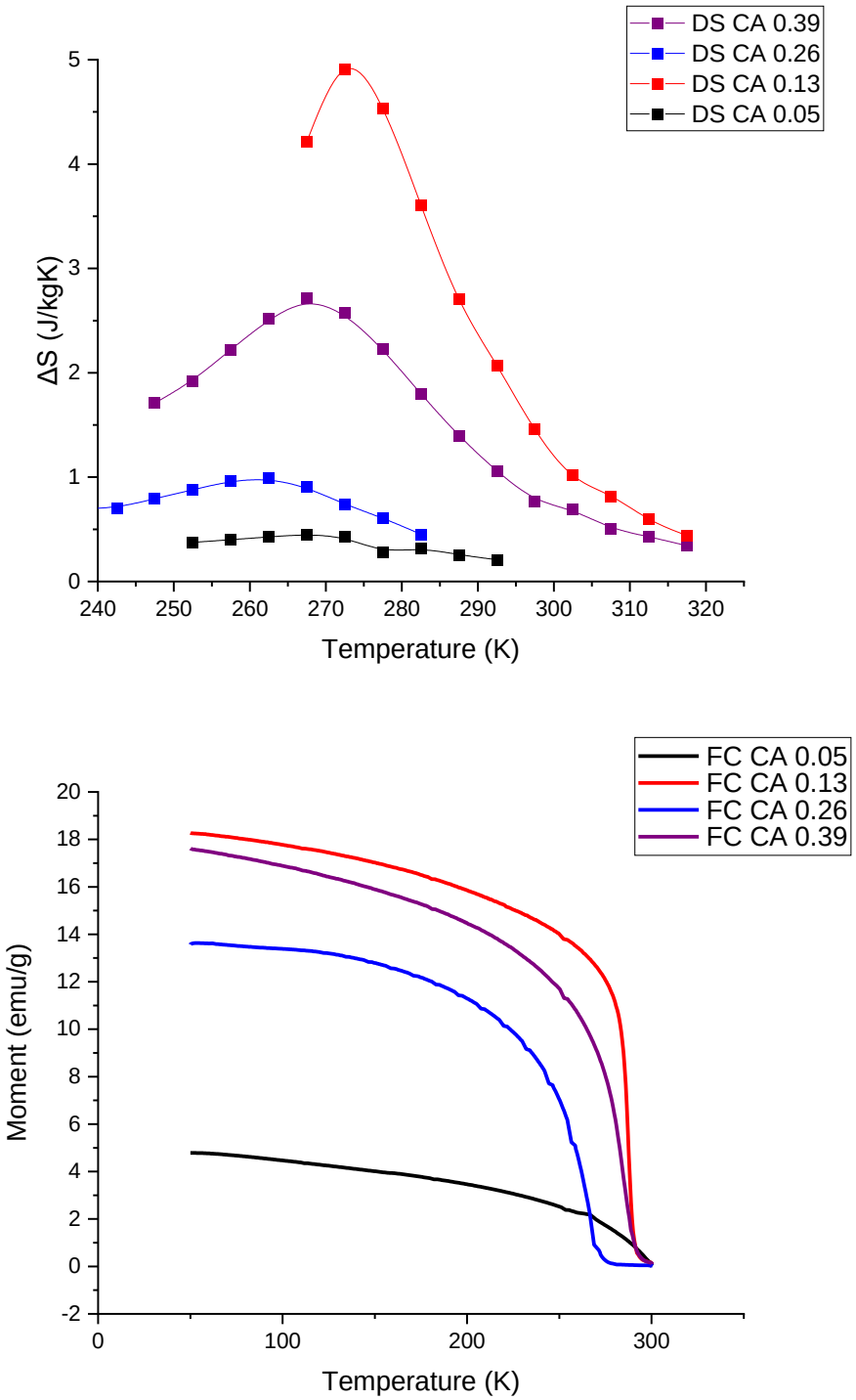

Figure 4.15 *MCE (a) and MT curves for the materials created with varying citric acid concentrations.*

4.3.5 PEG Starting Concentration

Regardless of the PEG starting concentration, phase-pure, crystalline nanoparticles were created (**Figure 4.16**). Crystallite sizes calculated were 87.6 nm, 53.8 nm, and 29.0 nm, for the 0.04, 0.08, and 0.16 samples, respectively, showing a decrease in crystallite size with increasing PEG concentration. Maximum ΔS values are 2.6 J/kgK, 0.99 J/kgK, and 1.1 J/kgK for the 0.04M, 0.08M, and 0.16M samples, respectively, which is roughly congruent with the correlation seen above between crystallite size and maximum ΔS. Similar to the pattern shown in literature and in the citric acid concentration work done above, decreasing crystallite size, induced by increasing starting PEG concentration, leads to decreasing T_c with a significant drop requiring a significant drop in crystallite size. The 0.04M material has a T_c of 265 K, the 0.08M material has a T_c of 263 K, and the 0.16M materials has a T_c value of 260 K. The 0.16M material also has a much less dramatic phase transition compared to the other two samples (**Figure 4.17**). Although these are all a little below room temperature, the best starting PEG concentration is 0.04M.

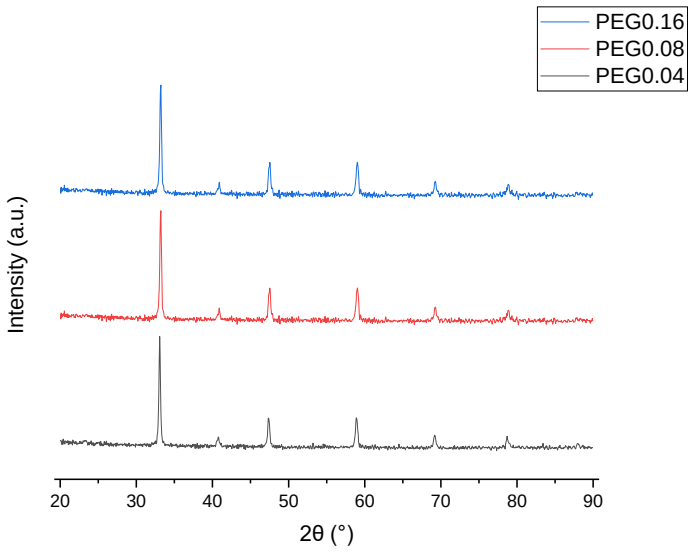

Figure 4.16 *XRD patterns for materials synthesized with a starting PEG concentration of 0.04 M, 0.08 M, and 0.16 M.*

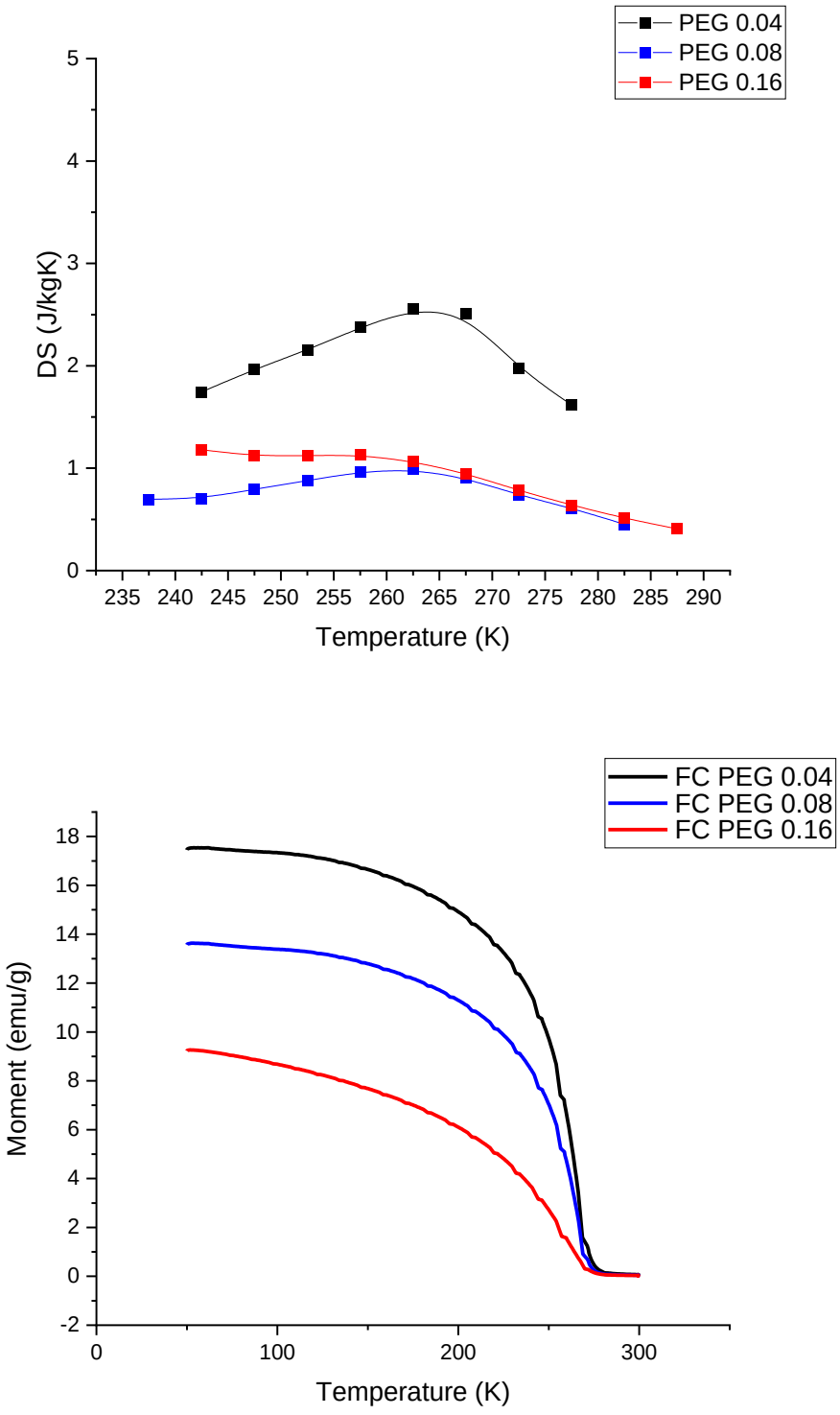

Figure 4.17 *MCE and MT curves for the PEG concentration materials showing a decrease in ΔS and T_c as PEG concentration was increased.*

4.3.6 Nitric Acid Volume and Gelation Time

Assuming there is enough nitric acid to fully dissolve all precursors (not everything dissolved in 5 mL of 4M nitric acid), all nitric acid volumes produce phase-pure, crystalline material (**Figure 4.18**). The 5 mL material contains ~10% La_2O_3 according to the RIR-based phase quantification feature in X'Pert HighScore. The crystallite sizes calculated using the Scherrer calculator were 29.0 nm for 5 mL, 58.3 nm for 10 mL (same sample as the 1000C, sp10hr, CA 0.26 material referenced in the above sections), 45.9 nm for 15 mL, and 20.7 nm for 20 mL. With the exception of the contaminated 5 mL material, these crystallite sizes decrease with increasing nitric acid volume. Unlike what was observed for other synthesis parameter changes, the location of the $2\theta \approx 33°$ peak does not shift at all between the 5-, 10-, and 15-mL materials and only a very minor shift is seen in the 20 mL pattern. This may be because of the increased gelation time induced by having more liquid present to evaporate. XRD patterns obtained for materials created with multiple gelation times in the standard 10 mL of nitric acid are congruent with this possibility. The longer the gel is heated on the hot plate the smaller the resultant crystallites (**Figure 4.19**). Beginning the sintering stage after 5 minutes of gelation creates crystallites that are 79.6 nm, 30 minutes creates 32.3 nm crystallites, and 60 minutes creates 21.8 nm crystallites. The standard removal time used for all other samples mentioned above was ~20 minutes. The 58.3 nm crystallite size of the 1000C/sp10hr/CA0.26/PEG0.08/10mL material fits into the observed trend (**Figure 4.20**).

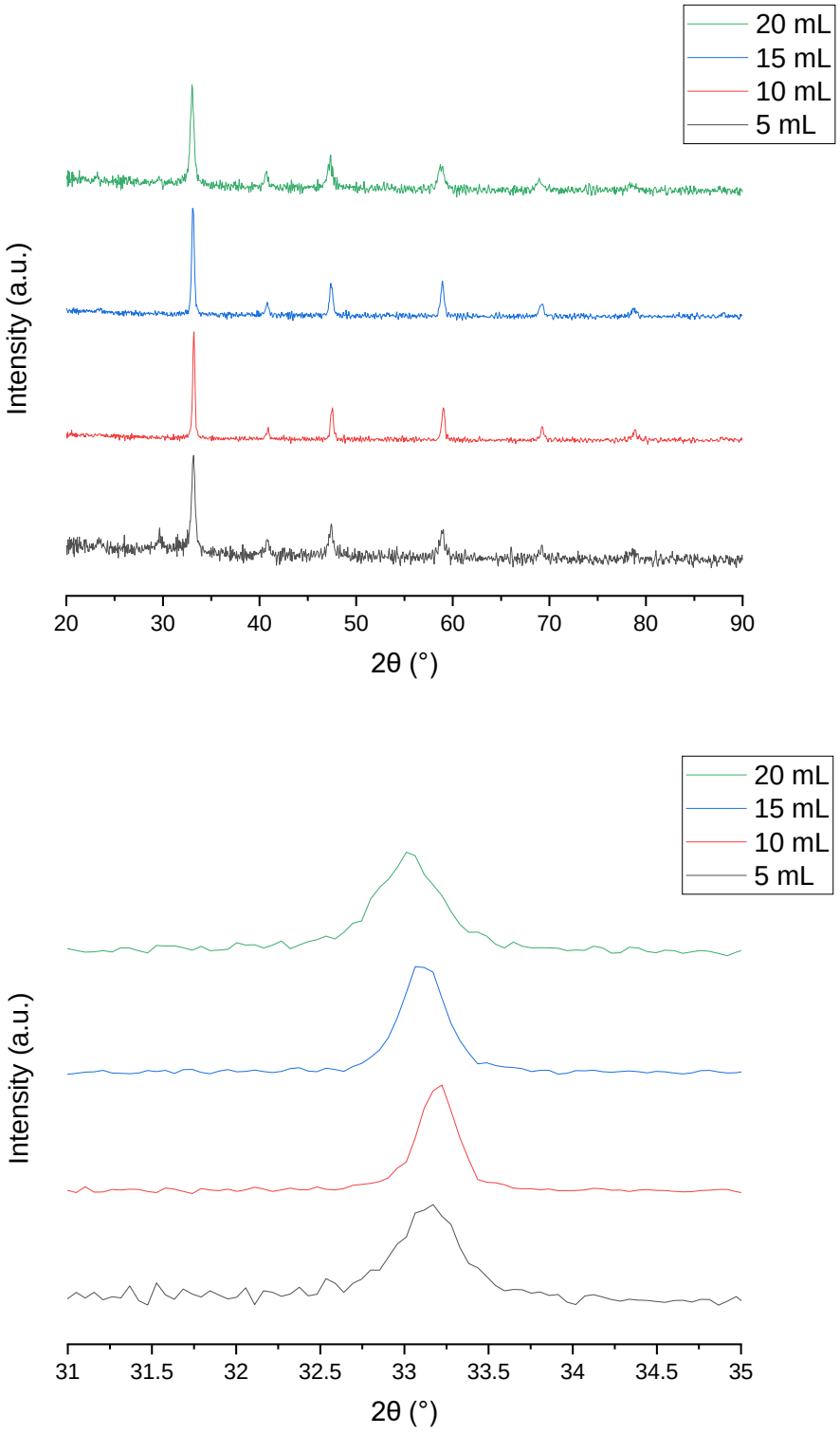

Figure 4.18 *XRD patterns for materials synthesized in different starting volumes of nitric acid. At the extremes - 5 mL and 20 mL - there is noticeably more noise in the pattern. The 5mL material also shows the presence of contamination from additional phases.*

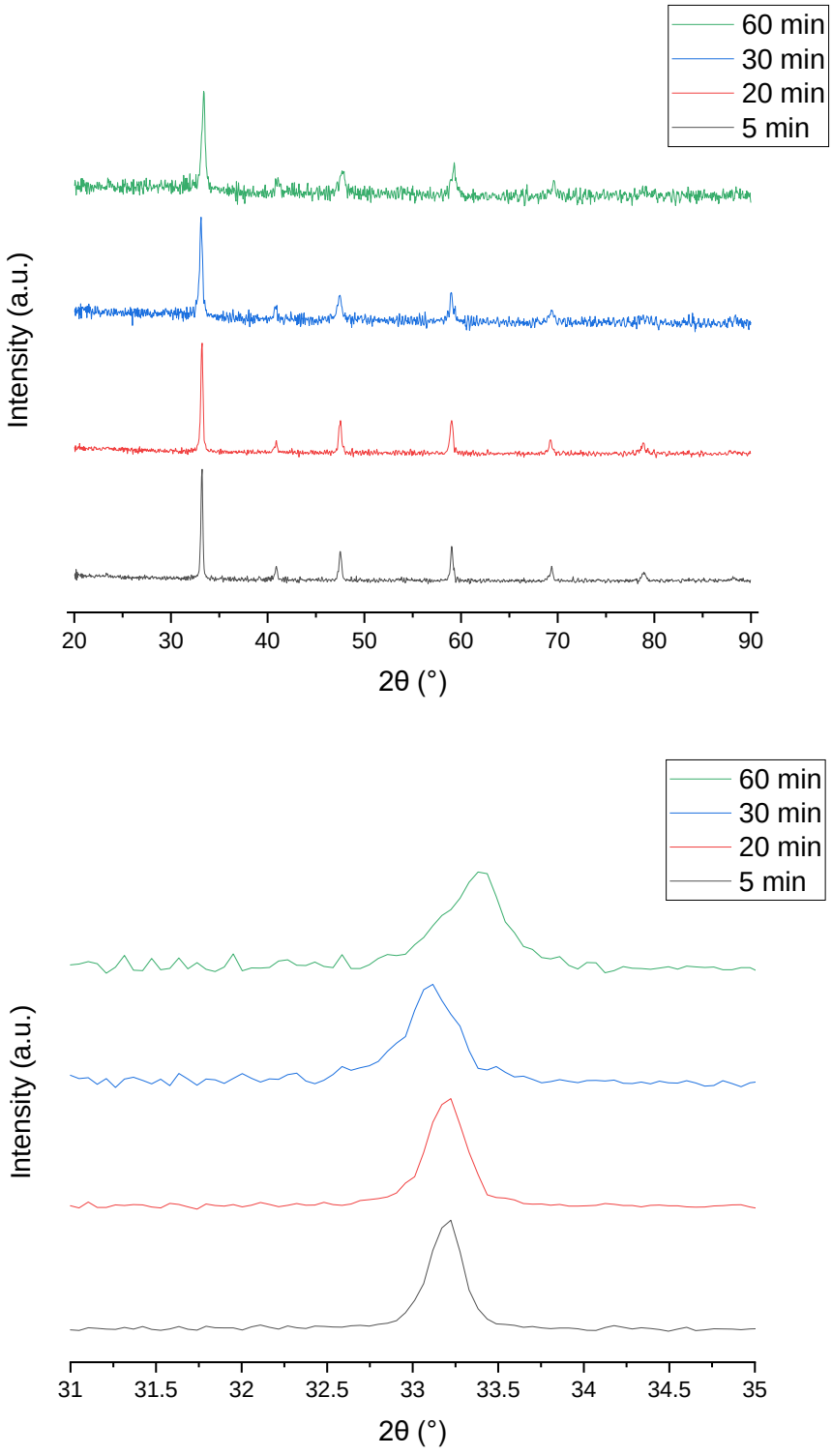

Figure 4.19 *XRD patterns for materials created with varying gelation times.*

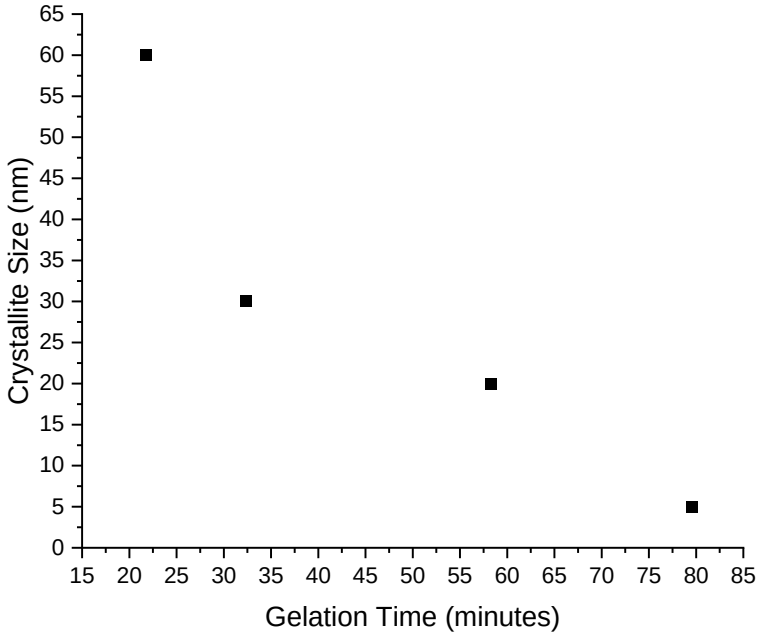

Figure 4.20 *Plot showing the relationship between crystallite size and gelation time. As gelation time increases crystallite size decreases.*

Similar to the trends seen in the materials above, with a decrease in crystallite size (increasing starting nitric acid volume) comes a decrease in the maximum ΔS value. Additionally, the contaminated 5 mL material and the 20 mL material have higher T_c values than the other two (**Figure 4.21**). The 10 mL and 15 mL materials have a T_c of ~265 K. The 5 mL material has a T_c of ~275 K. The 20 mL material has a T_c of ~300 K, though the peak in the MCE curve appears at ~266K along with the 10 mL and 15 mL material. This mismatch may be partially due to the wide working temperature range evident in the M(T) curve. The 1/X vs. Temperature plot similarly does not look as may be expected; whereas all three of the other materials have a clear T_G and paramagnetic region, the 20 mL sample's plot has no clear T_G, nor does it have a region which clearly obeys the Curie-Weiss law. This may be due to the small crystallite size for this material. Similar to how the LSMO parent compound discussed in the second section of this work exhibited

multiple transition points in the 1/X vs. Temperature plot, the 20 mL material may also have multiple phases going from ferromagnetic to paramagnetic at different temperatures, obfuscating the T_c and T_G values and widening the working temperature range. Because it led to a clearer phase transition, making relevant properties simpler to see and understand, 10 mL was chosen as the optimal starting volume.

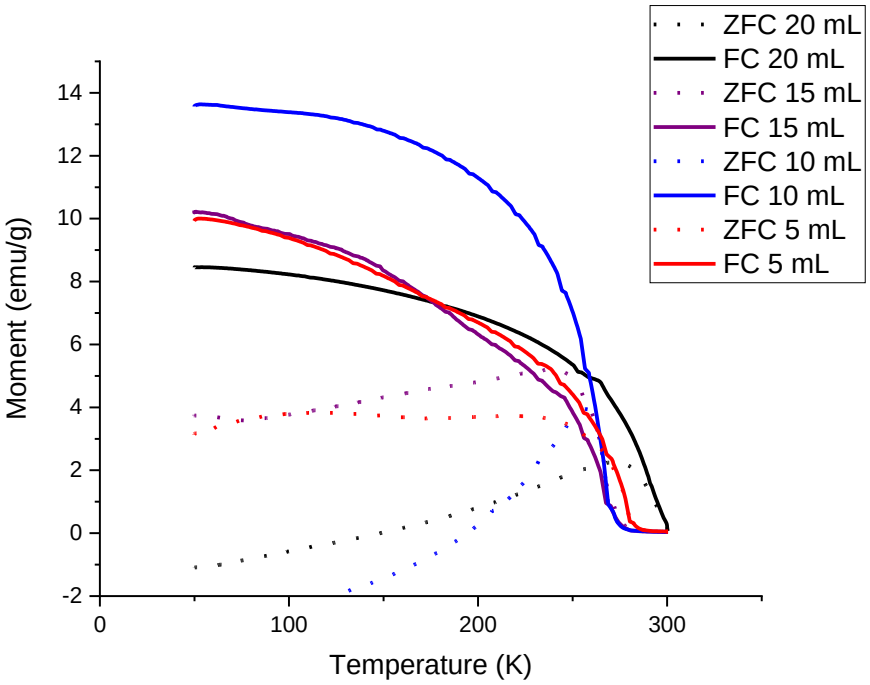
ZFC 20 mL
FC 20 mL
ZFC 15 mL
FC 15 mL
ZFC 10 mL
FC 10 mL
ZFC 5 mL
FC 5 mL
Moment (emu/g)
Temperature (K)
14
12
10
8
6
4
2
0
-2
0
100
200
300

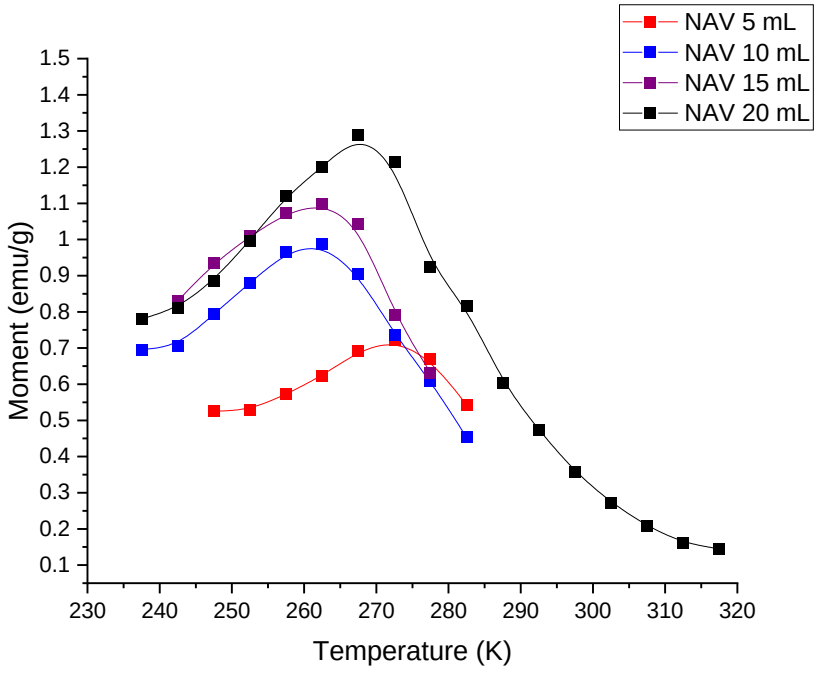
NAV 5 mL
NAV 10 mL
NAV 15 mL
NAV 20 mL
Moment (emu/g)
Temperature (K)
1.5
1.4
1.3
1.2
1.1
1
0.9
0.8
0.7
0.6
0.5
0.4
0.3
0.2
0.1
230
240
250
260
270
280
290
300
310
320

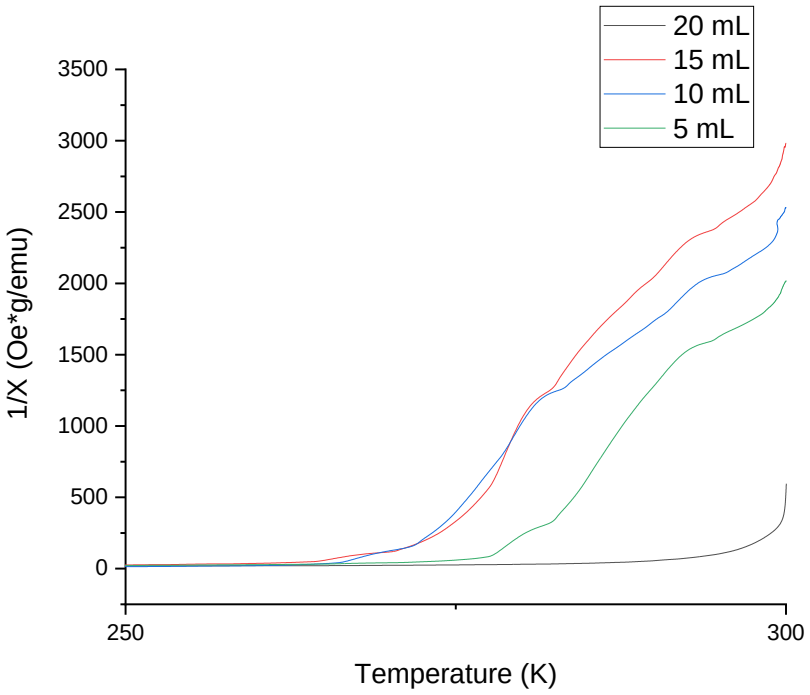

Figure 4.21 *MT, MCE, and 1/X figures for materials created with increasing starting volumes of nitric acid.*

4.3.7 Optimized Parameters

The optimal parameters determined were a CA concentration of 0.13M, PEG concentration of 0.04M, citric acid, 10 mL of nitric acid, sintered at 900 °C for 3 hours and cooled slowly. These parameters lead to a phase-pure and highly crystalline material with a crystallite size of 149.5 nm (**Figure 4.22**). Barring any unexpected break from the patterns established in this section showing an increase in ΔS and T_c with an increase in crystallite size, this material should have a high ΔS value and a T_c of ~280K.

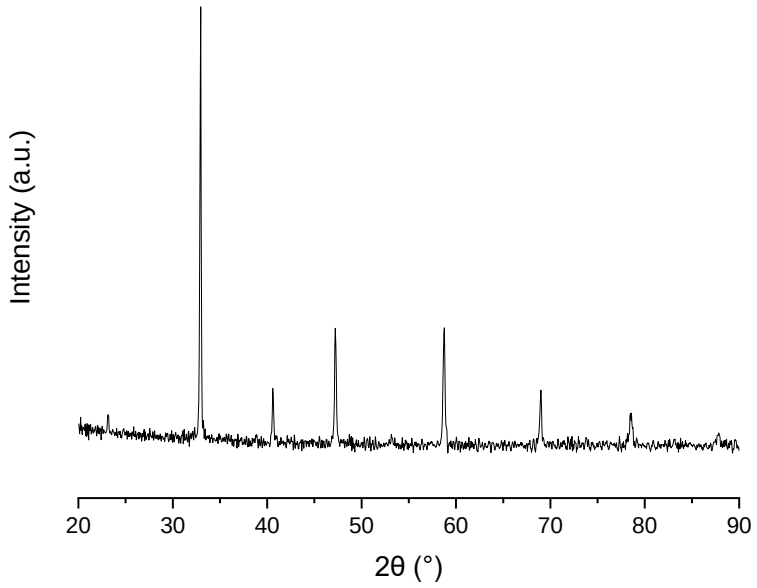

Figure 4.22 *XRD pattern for material created with the determined optimal parameters.*

4.4 Synthesis Changes Conclusions

Nearly all chelating agents, starting concentrations and volumes, sintering times, and sintering temperatures analyzed produced phase pure material with only a few exception (nitric acid starting volume of 5 mL and CA starting concentration of 0.05 M). As the sintering parameters change the crystallite size also changes. With a decrease in nitric acid volume, a decrease in starting PEG concentration, or an increase in sintering temperature, crystallite sizes increase. Crystallite size is also maximized after six hours of sintering if cooled quickly or after three hours of sintering if cooled slowly and with citric acid with a starting concentration of 0.13 M as the chelating agent. As the crystallite size increases, ΔS increases (**Figure 4.23**).

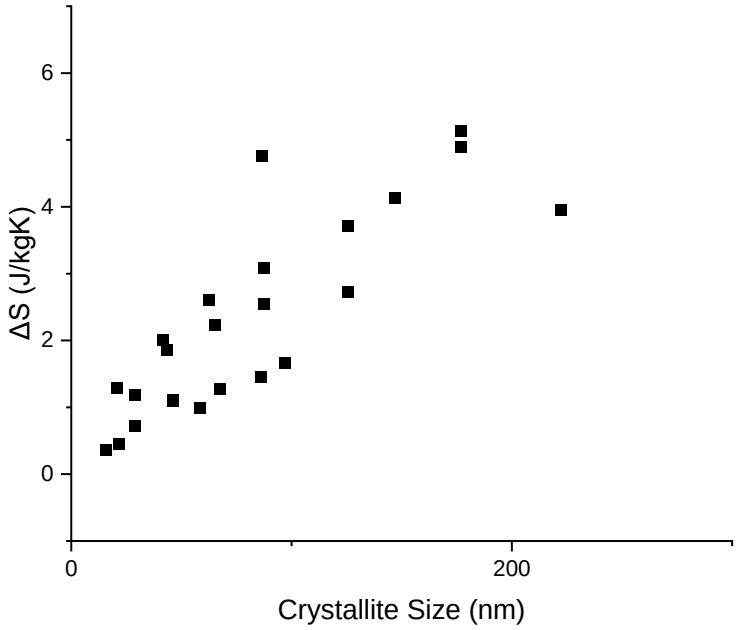

Figure 4.23 *ΔS increases with increasing crystallite size but there is no clear correlation between crystallite size and T_c.*

There is no correlation between the lattice parameters and T_c or ΔS (**Figure 4.24**). The correlation between ΔS and crystallite size is far more definitive, which supports the conclusion that the various sintering parameters studied here control ΔS (indirectly by altering the electronic interactions) and T_c through crystallite size and presence of a Griffith's phase as opposed to induced changes in the crystal structure itself. In order to definitively confirm this, however, it would be beneficial to obtain further crystal and magnetic structure information using neutron scattering. This would allow for the quantification of the a-site and b-site defects, interactions across magnetic domains, and magnetic behavior within the Griffith's phase.

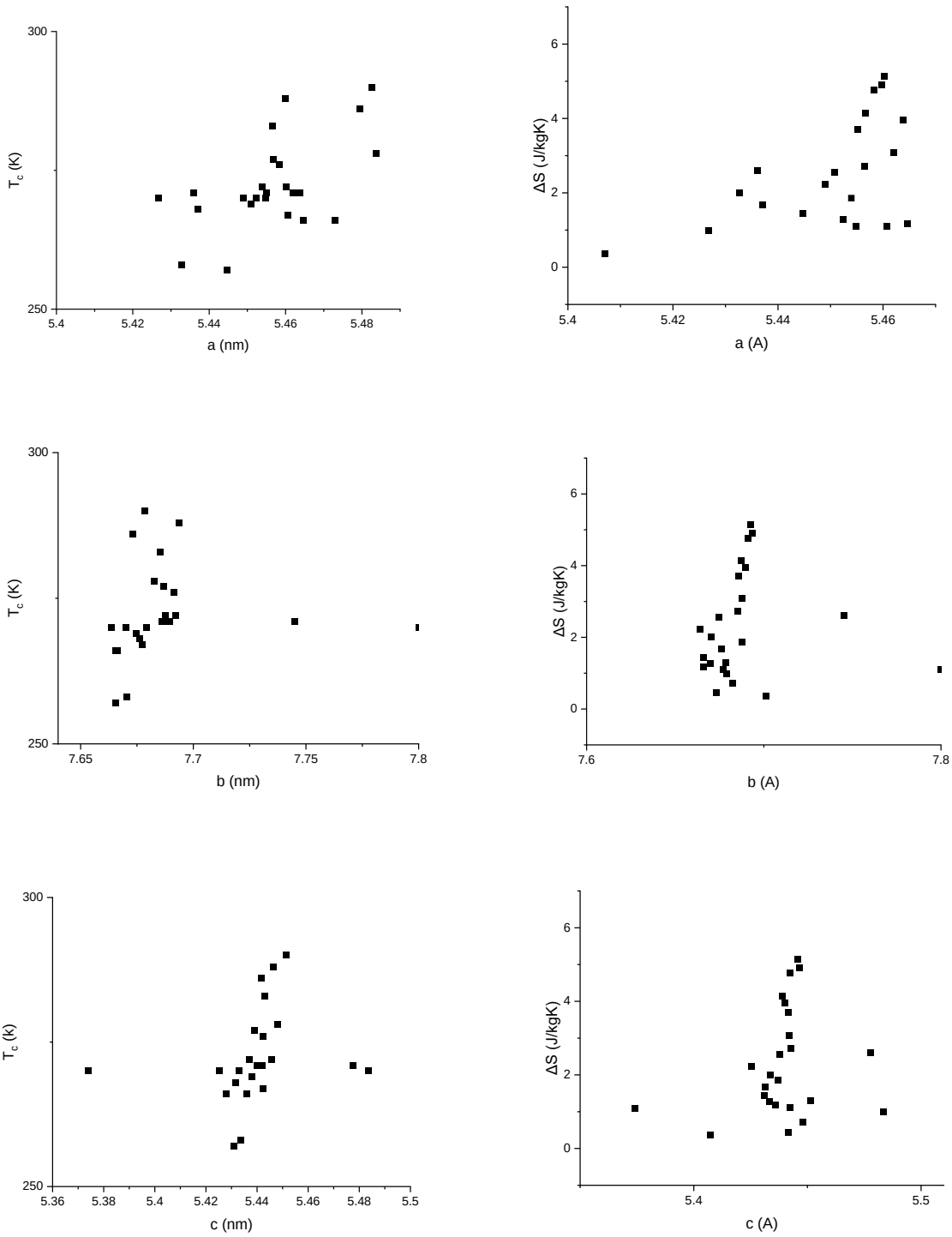

Figure 4.24 *Lattice parameters plotted with ΔS and T_c.*

Although a large enough increase in crystallite size appears to have a measurable increase in T_c no distinct jump in size or minimum threshold size clearly increases T_c. There is also very little change in T_c overall, varying only from ~260K to ~280K. This is significantly less change than what was seen in the sodium substitution study where the T_c value varied from 265K to 333K. T_c, then, still appears to be controllable primarily through changing the oxidation states of the Mn ions and not appreciably altered through distortion of the crystal lattice or small changes in crystallite size.

The ideal parameters are 10 mL of nitric acid, 0.04 M PEG, 0.13 M citric acid, sintered at 900C for 3 hours and cooled slowly, which leads to 150 nm crystals. Future work should look into the kinetics and mechanisms of each synthesis stage in order to tease out additional details as to their effects. Although the kinetics have been determined for a solid-state synthesis of $LaMnO_3$ materials, the kinetics of the sintering stage or the gelation process have not been studied for LCMO materials created via the sol-gel technique. A study of the kinetics of either and/or both stages may provide insights into both the synthesis method itself as well as why and how the observed structural and morphological effects are produced and perhaps explain the observed changes in T_c.[149] In order to measure this, as well as obtain a more complete picture of the crystallite size and structure control through synthesis parameters, in-situ XRD as well as neutron diffraction would be beneficial.

5 Application to $La_{0.75}Ca_{0.25}MnO_3$

5.1 Overview

Table 5.1 shows a selection of lanthanum manganite materials and their figures of merit. Although they demonstrate very high values of ΔS, $La_{0.75}Ca_{0.25}MnO_3$ materials previously synthesized with an additional 200 °C decomposition stage prior to sintering at high temperatures show T_c values too low for magnetic refrigeration applications. This project aimed to increase the T_c values through omitting the decomposition stage and altering the sintering parameters following the observation $La_{0.60}Ca_{0.40}MnO_3$ materials discussed above where increasing sintering temperature positively impacted the magnetic properties.[3,13,54,57,150,151]

Table 5.1 *Figures of merit for a selection of magnetocaloric materials prepared with and without a 200C decomposition stage before sintering.*

Material	Decomp	Sinter Temp (°C)	Tc (K)	ΔS(J/kgK)	μH (T)	Crystallite Size (nm)	Ref.
$La_{0.75}Ca_{0.25}MnO_3$	Yes	1400	224	4.7	1.5	300	[55]
$La_{0.75}Ca_{0.25}MnO_3$	Yes	1000	177	2	1.5	120	[55]
$La_{0.75}Ca_{0.25}MnO_3$	Yes	1000	200	1.15	3	112.0	This work
$La_{0.75}Ca_{0.25}MnO_3$	No	1000	270	6.04	3	192.6	This work
$La_{0.60}Ca_{0.40}MnO_3$	No	1000	270	1.75	3	63.8	Chapter 4
$La_{0.60}Ca_{0.40}MnO_3$	No	1100	277	4.14	3	147.0	Chapter 4
$La_{0.60}Ca_{0.40}MnO_3$	No	1200	272	5.14	3	176.9	Chapter 4

5.2 Experimental Details

$La_{0.75}Ca_{0.25}MnO_3$ nanoparticles were synthesized via a sol-gel synthesis as discussed above with stoichiometric starting amounts of the metal precursors and concentrations of citric acid, nitric acid, and PEG unchanged from the default synthesis recipe described in section 1. After formation of the gel a comparison material (CM) was created by decomposing the gel first at 200 °C overnight, then sintering at 1000 °C for 10 hours, as described by Guo et al.[54,55,57] Materials were also created without the decomposition stage with sintering temperatures of 600 °C, 1000 °C, and 1100 °C.

Samples were characterized using LA-ICP-MS, XRD, DSC, and TGA-IR as described above. Magnetic measurements for determining T_c (from M(T) curves) and ΔS (from M(H) curves) were carried out as outlined in the Characterization section. M(T) curves were collected from 50 K to 300 K at 100 Oe; MH curves were collected from 220 K to 320 K for the 600C, 1000C, and 1100C materials, and from 100 K to 320 K for the CM sample across 3T at 5K intervals.

5.3 Results and Discussion

The sintering temperature did not produce any appreciable change in T_c or ΔS values. T_c for all three varying sintering temperature samples was ~270K (**Figure 5.1a**). This is far higher than both the values reported by Guo et al., ~198K, and the value seen in the CM sample, ~1K (**Figure 5.1b**) and is much closer to room temperature. The transition observed also becomes much sharper after sintering and when the decomposition stage is skipped, leading to higher ΔS peaks in the MCE curves (**Figure 5.2**). Maximum ΔS values are 6.1 J/kgK, 6.0 J/kgK, and 6.4 J/kgK

for the 600C, 1000C, and 1100C samples, respectively, and 1.2 J/kgK, 0.75 J/kgK, 0.59 J/kgK, and 0.36 J/kgK for the CM, D1hr, D5hr, and D3hr samples, respectively.

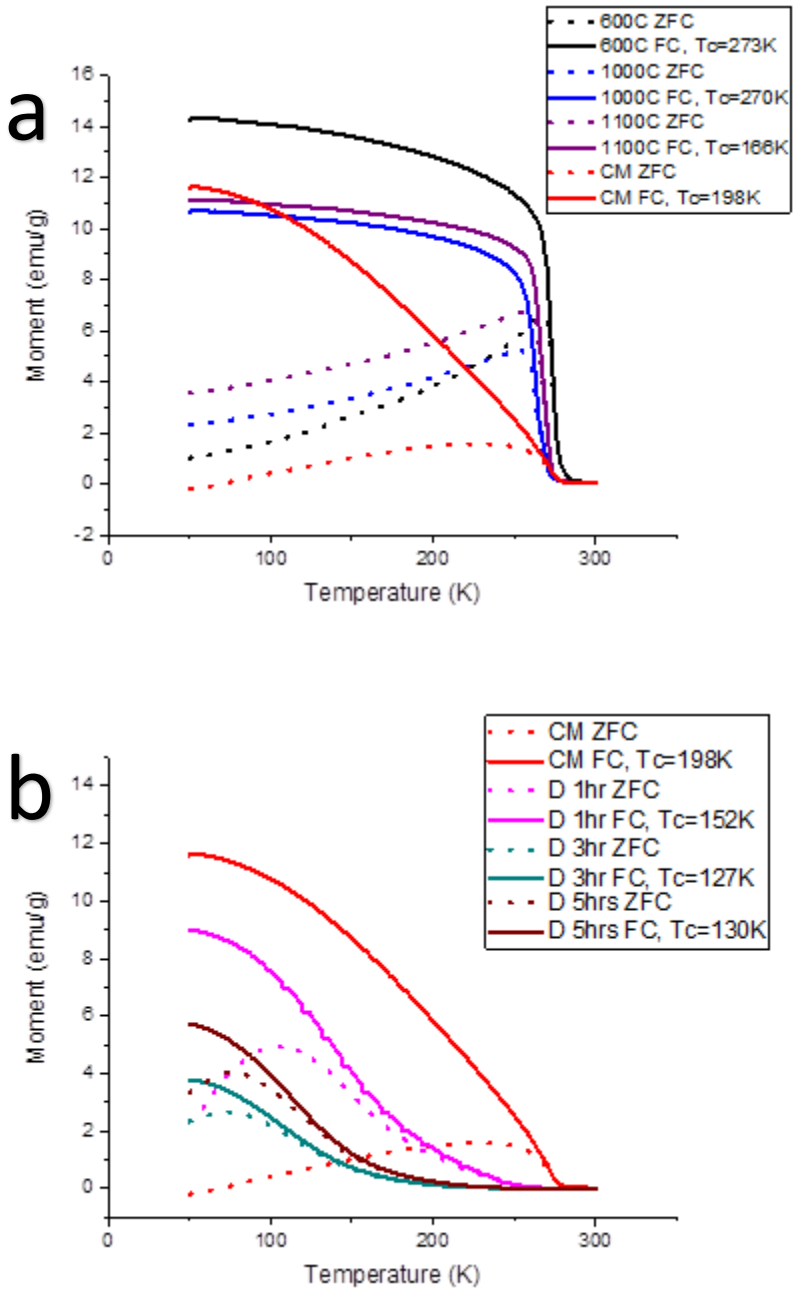

Figure 5.1. *MT curves for all $La_{0.75}Ca_{0.25}MnO_3$ materials. A sharper transition and higher T_c is observed in materials created without a preliminary 200 °C decomposition step. (a) shows MT curves for materials created at varying sintering temperatures and the CM sample. (b) shows MT curves for materials at various stages of the decomposition step before sintering and the CM sample.*

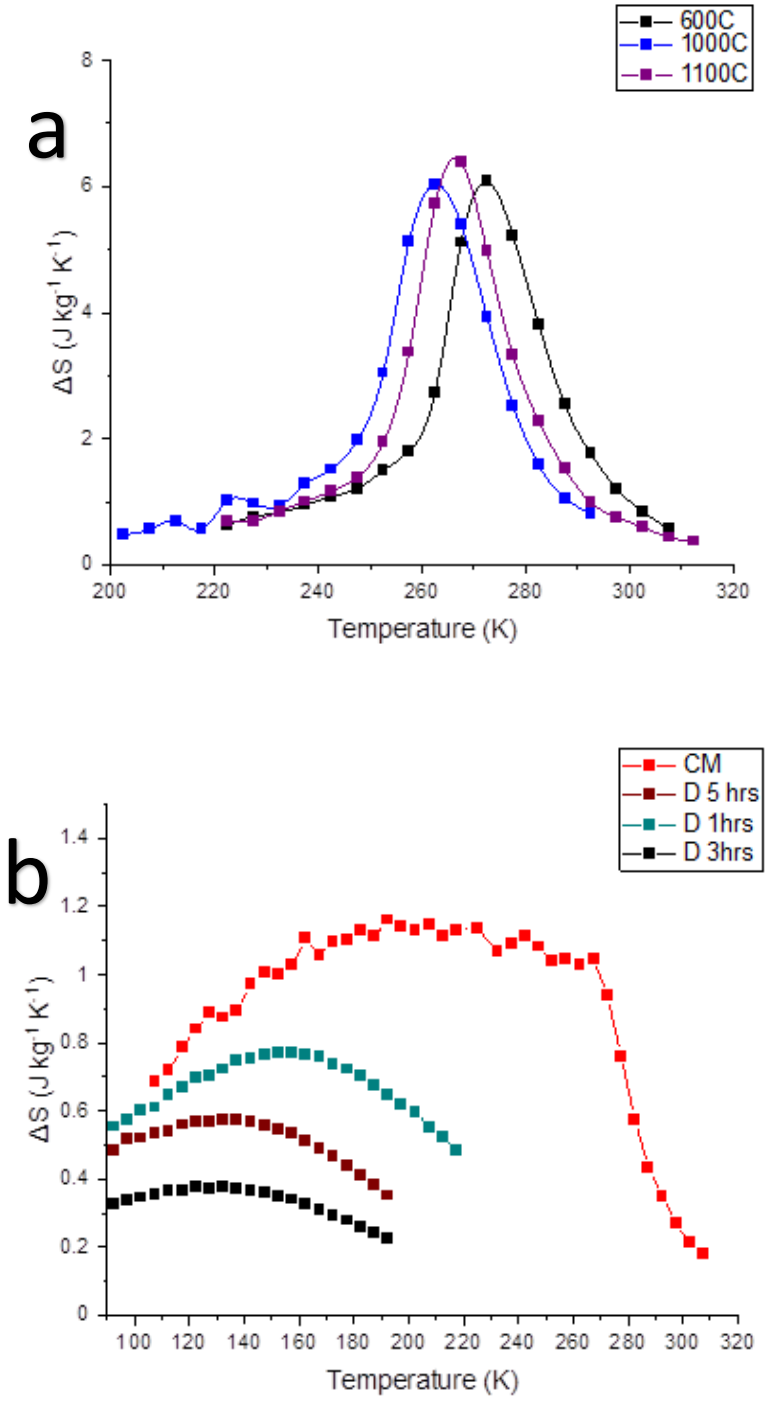

***Figure 5.2**. MCE curves for all $La_{0.75}Ca_{0.25}MnO_3$ materials. (a) shows MCE curves for materials synthesized without a preliminary decomposition stage and sintered at three different temperatures. (b) shows MCE*

curves for materials at various stages of the 200 °C decomposition stage and after sintering a decomposed sample (CM).

XRD characterization shows excellent phase purity and crystallinity for all sintered samples (**Figure 5.3a**). Because of the significantly smaller crystallites in the decomposed samples and decreased crystallinity those XRD patterns exhibit greater noise but still demonstrate the presence of a single phase (**Figure 5.3b**). The CM sample has an average crystallite size of 112.0 nm as calculated using the Scherrer calculator in X'Pert HighScore. Without a decomposition stage the crystallite size increases to 172.5 nm for the 1100C sample, 192.6 nm for the 1000C sample, and 197.3 nm for the 600C sample. The samples taken during the decomposition step all have crystallite sizes around ~18 nm. The crystallite sizes of ~100 nm for the CM sample and ~200 nm for the 1000C sample are congruent with particle sizes seen in SEM images (**Figure 5.4**). As stated previously, an increase in crystallite size has been demonstrated in the literature to correlate to an increase in ΔS, and in one instance T_c as well, in $La_{0.60}Cs_{0.40}MnO_3$ materials,[56] a decrease in T_c for $La_{0.70}Ca_{0.30}MnO_3$ materials,[78,82] and an increase in Tc, ΔS, and the narrowing of the MCE curve for $La_{0.80}ca_{0.20}MnO_3$ materials.[146] In the studies presented in this work an increase in crystallite size has been confirmed to lead to an increase in ΔS and a large jump in crystallite size can positively impact the T_c value. The data presented here implies the minimal crystallite change amongst the materials created without a decomposition stage is not sufficient to induce an appreciable change in T_c, ΔS, or the width of the MCE curves. Only the omission of the decomposition stage, which leads to a significant increase in crystallite size, has a clear positive effect on T_c and ΔS.

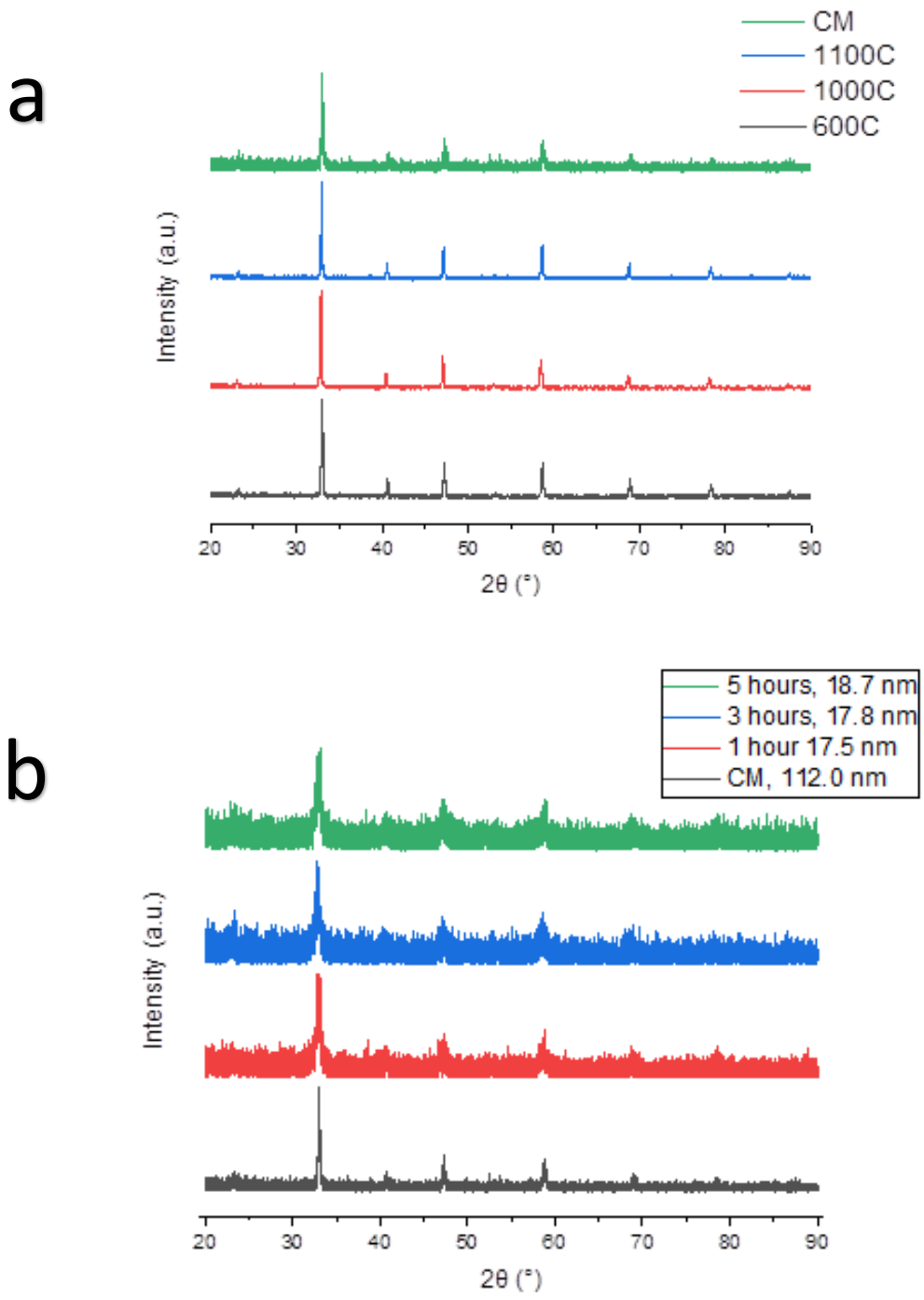

Figure 5.3. *XRD patterns for all $La_{0.75}Ca_{0.25}MnO_3$ materials synthesized with and without a decomposition stage (a) and at various time points during the decomposition step (b).*

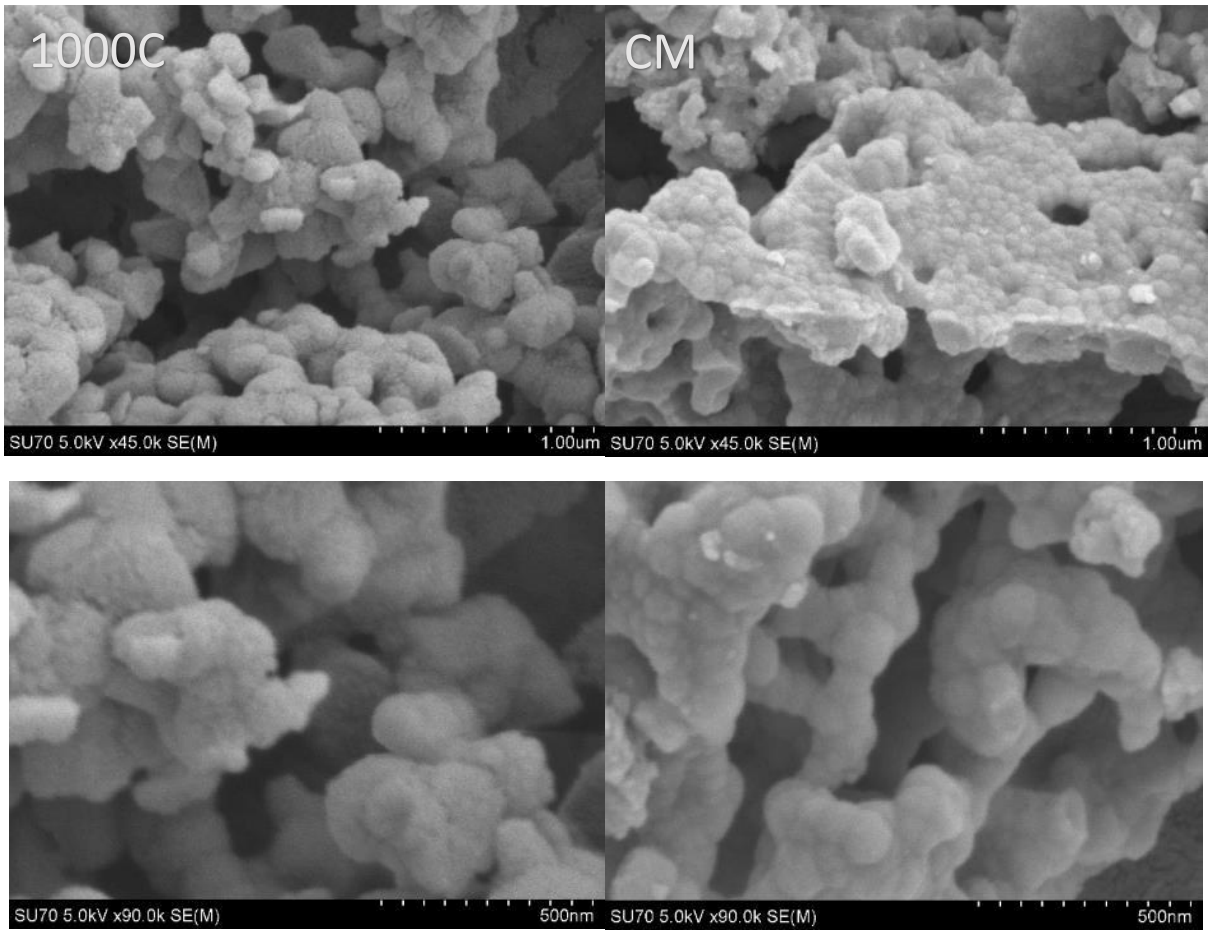

Figure 5.4. *SEM images for the CM and 1000C $La_{0.75}Ca_{0.25}MnO_3$ materials showing particle sizes of ~100 nm and ~200 nm congruent with XRD crystallite size calculations.*

DSC and TGA-IR measurements taken during the decomposition stage offer insight into what occurs over the course of this step. The DSC curve shows an endothermic event beginning just above 100 °C, followed by an exothermic event. The curve stabilizes within the first 25 minutes and no further appreciable change is observed until sintering begins just shy of 600 °C. This correlates well with the TGA curve collected, which shows a mass loss starting at 100 °C, followed by stabilization of the curve. It can be surmised that, in accordance with the assumed synthesis process, the initial endothermic and exothermic events and mass loss can be attributed to the formation of a hard resin as the material is dried and initial crystallization occurs. IR spectra

collected on the gases produced during the TGA measurement confirm that during the mass water and CO_2 are produced as the material dries and organic content decomposes. Nothing further occurs until the temperature is increased to induce sintering. This is congruent with the XRD patterns shown above, which show crystalline product within the first hour of the decomposition stage and no change in crystallite size until after sintering begins. By adding the decomposition stage and forming the hard resin it is possible that the formation of the crystals follows more of a nonclassical nucleation process, leading to particles with higher surface area and a greater total contribution of the Griffith's phase.

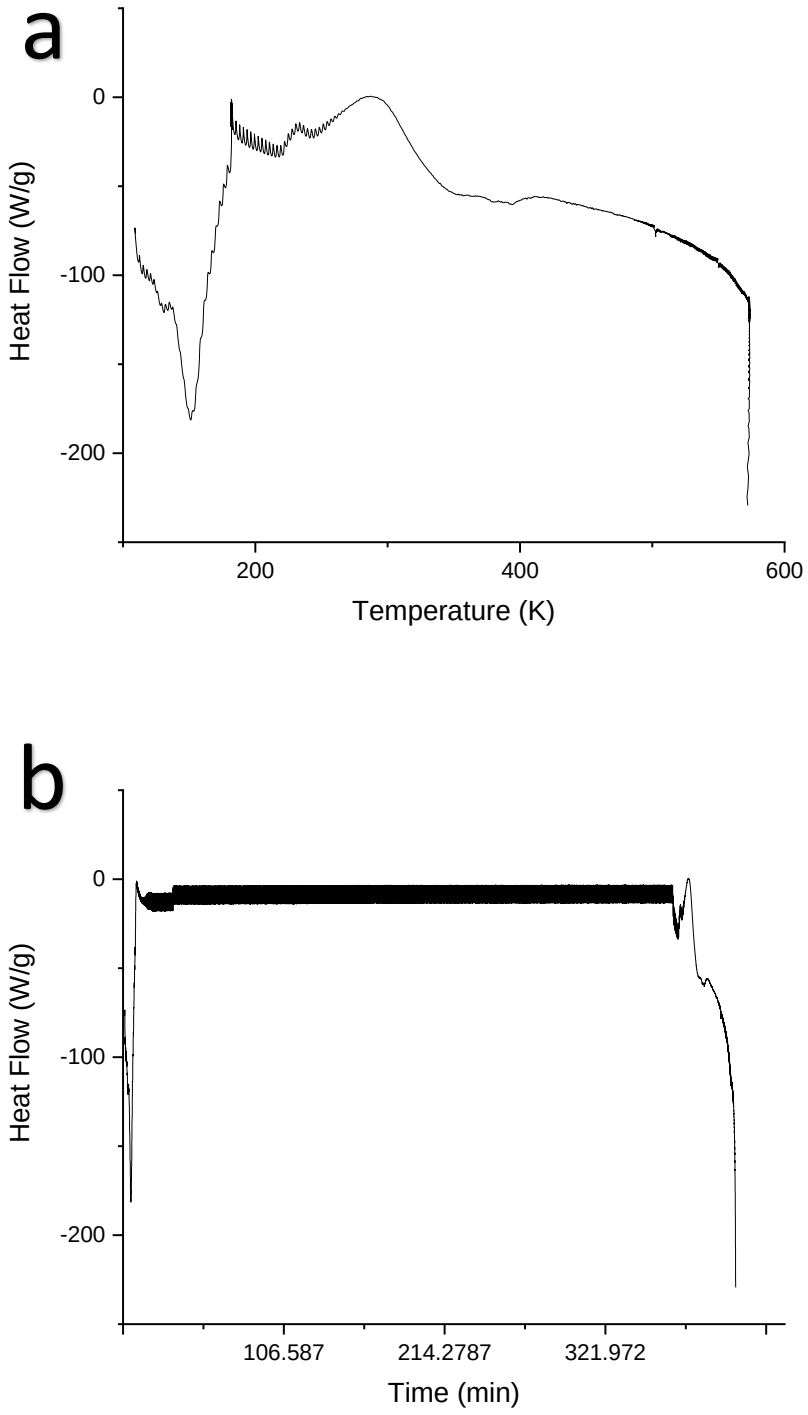

***Figure 5.5**. Heat Flow vs. Temperature (a) and Heat Flow vs. Time (b) DSC curves. After reaching ~300 °C (within the first 25 minutes of the experiment) stabilization occurs very quickly. The material remains stable until just shy of ~600 °C, where an endothermic event begins.*

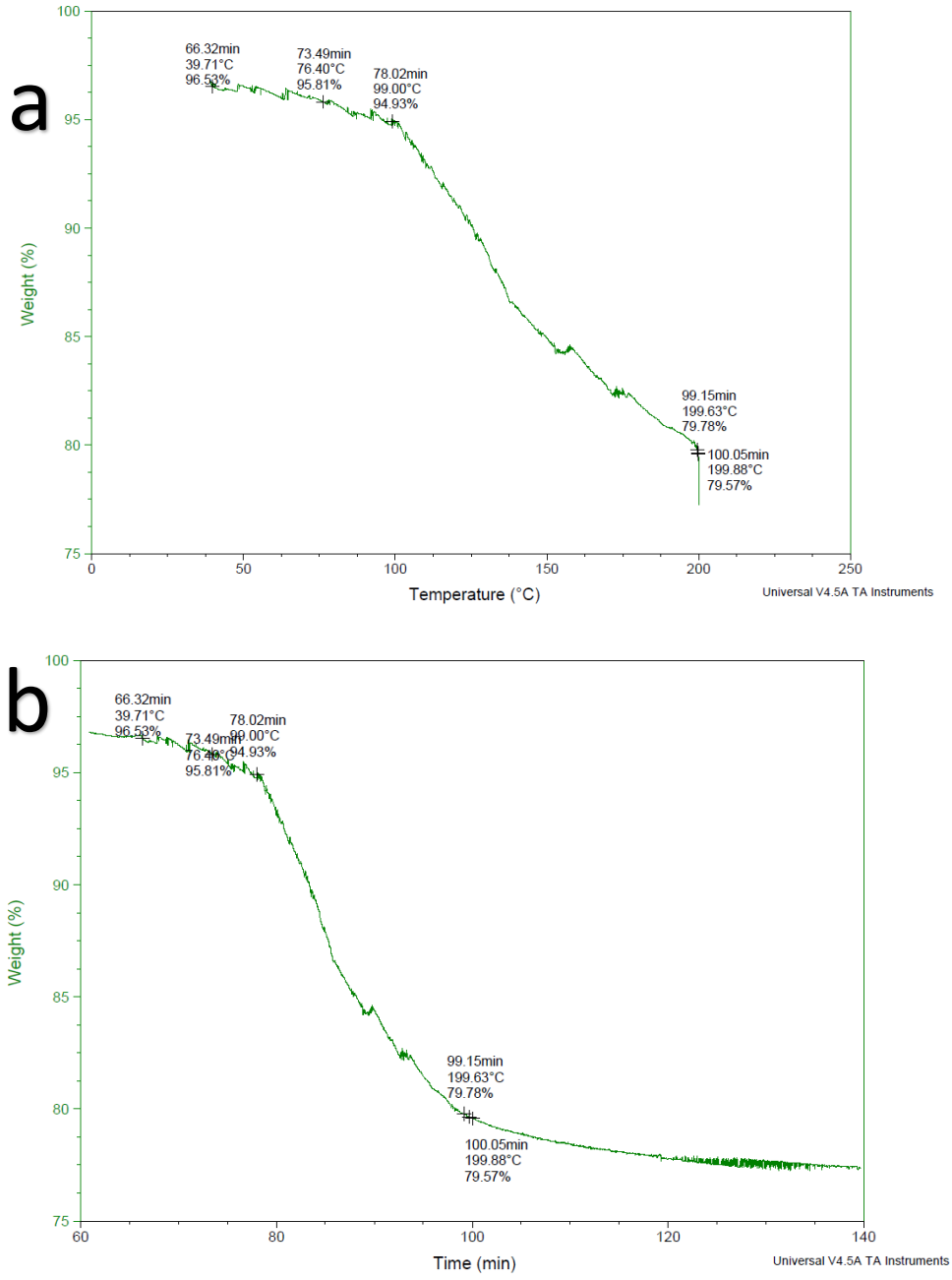

Figure 5.6. *Weight vs. Temperature (a) and Weight % vs. Time (b) TGA cures. A weight change corresponding to the removal of water and production of CO_2 is seen starting at ~90 degrees and continuing until after the sample reached 200 degrees. ~100 minutes into the decomposition the weight stabilizes.*

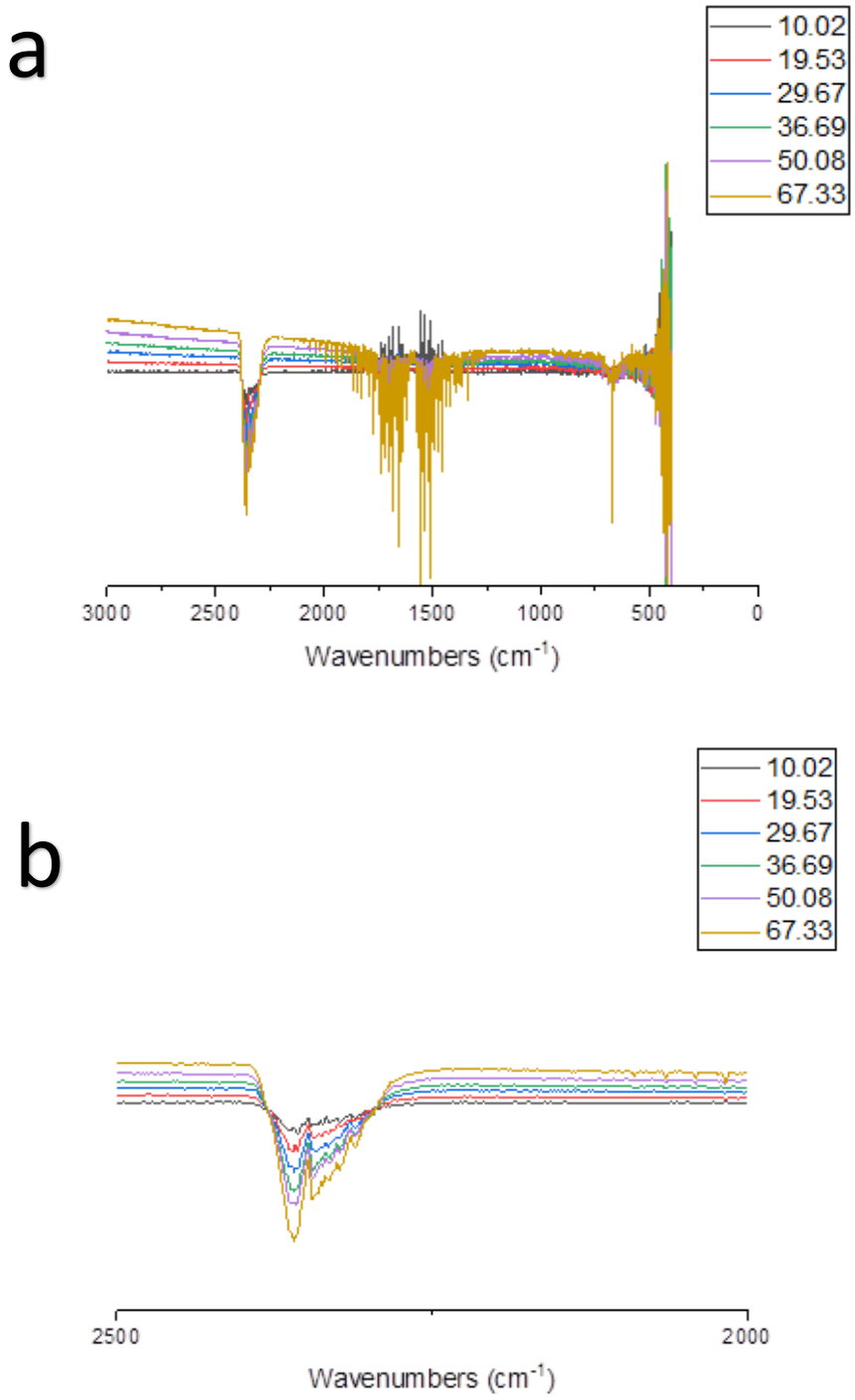

Figure 5.7. *Full (a) and CO_2 peak (b) IR spectra corresponding to the weight loss seen in the TGA curves above demonstrating the loss of CO_2 and H_2O.*

5.4 $La_{0.75}Ca_{0.25}MnO_3$ Conclusion

In contrast to the results seen in the synthesis optimization work (Chapter 4) with $La_{0.60}Ca_{0.40}MnO_3$, increasing the sintering temperature did not cleanly increase the crystallite size of the $La_{0.75}Ca_{0.25}MnO_3$ materials. As long as no decomposition stage has been carried out before sintering, crystallite size was just below 200 nm for materials synthesized at 1000 °C, 1100 °C, and 1200 °C. The incorporation of a decomposition stage limits crystallite size to just over 100 nm. Along with this decrease in crystallite size comes a decrease in both T_c and ΔS. Without the decomposition stage the T_c value reaches a more useful value for magnetic refrigeration applications – 270 K as opposed to 200 K. This may be attributed to a decrease in the contribution of the Griffiths phase to the overall magnetic properties of the material.

The DSC and TGA-IR measurements show that the gel dries, and the organic component begins to decompose during the decomposition stage. By removing the decomposition stage and sintering at temperatures of at least 1000 °C the T_c observed is close enough to room temperature to be useful for magnetic refrigeration. This is a significant improvement over literature T_c values for $La_{0.75}Ca_{0.25}MnO_3$ materials. Additionally, the maximum ΔS value observed was 6.0 J/kgK, which is even higher than the maximum ΔS value for the $La_{0.60}Ca_{0.40}MnO_3$ materials studied in this work. Additional synthesis optimization and perhaps the incorporation of a small amount of Na^+ in place of Ca^{2+} has the potential to further increase the maximum ΔS value and/or T_c value and further optimize the material for magnetic refrigeration.

It would also be beneficial to pursue further in-situ characterization of the decomposition stage as well as perform similar characterization of the sintering stage. Insights such as those

achieved regarding the sintering stage would be even more beneficial over the course of the sintering stage in order to track the changes in crystal structure and crystallite size across both pieces.

6 Summary

The primary goal of this work was to pursue a lanthanum manganite nanomaterial idealized for use as the solid refrigerant in a magnetic refrigeration system. This material needs to have a high maximum ΔS value and a T_c near room temperature, ideally comparable to existing materials, and be easier and more inexpensive to synthesize than the current best refrigerant materials. Lanthanum manganite materials synthesized via a modified Pechini sol-gel synthesis have the advantage of the more expensive Gd- or Rh-containing materials, are less expensive and simpler to synthesize reliably than materials created through arc-melting or other solid-state reaction techniques, and have properties proven to be tunable through Mn-O-Mn bond distances and angles, Mn-ion oxidation states, particle and crystallite size, and surface texture. Pursuing an ideal material was approached through three avenues: altering the Mn-O-Mn bond distances and angles to change orbital overlap, modifying the ratio of Mn^{3+} to Mn^{4+} to change Zener Double Exchange interactions, and using synthesis parameters to optimize crystallite size. Key findings are summarized below.

1) Introducing Sr^{2+} in place of Ca^{2+} in $La_{0.60}Ca_{0.40}MnO_3$ nanomaterials alters primarily the Mn-O-Mn bond distances and angles, as well as crystallite size, without any appreciable effects being seen in the Mn oxidation states. As Sr^{2+} concentration increased, leading to a decrease in crystallite size, the maximum ΔS value decreased but T_c remained mostly constant. This implies that changing the Mn-O-Mn bond distances and angles mostly affects the value of ΔS and rapidly decreasing the crystallite sizes can offset any small changes to T_c that may also be induced.

2) Changing the manganese ion oxidation state ratios with little effect on the Mn-O-Mn bond distances and angles through substituting in Na^{+} in place of Ca^{2+} in the $La_{0.60}Ca_{0.40}MnO_3$ crystal lattice leads to a significant increase in T_c, taking the value not to room temperature and beyond as sodium concentration increases. This is achieved with a significantly less dramatic effect on ΔS compared to the strontium substitution work. The implication is that the manganese oxidation states have the larger effect on T_c, while Mn-O-Mn bond distances and angles have the larger effect on T_c.
3) Attempts to optimize synthesis parameters further reinforced that crystallite size has an appreciable effect on ΔS, but only significant alterations in crystallite size have any effect on T_c. Even with comparatively larger increases in crystallite size, the positive effect on T_c is much more minimal than changing the oxidation states. Additionally, very small crystallites (created with a starting nitric acid volume of 20 mL) were seen to create multiple competing phases which transition at different temperatures as was observed in the LSMO material. The optimal synthesis parameters were determined to be 10 mL of nitric acid, 0.04 M PEG, 0.13 M citric acid, and sintered at 900C for 3 hours and cooled slowly. These parameters lead to a $La_{0.60}Ca_{0.40}MnO_3$ with and average crystallite size of 150 nm and, which should have a high ΔS and T_c, making the material viable for use in magnetic refrigeration.
4) Applying these observations to the $La_{0.75}Ca_{0.25}MnO_3$, along with eliminating the decomposition stage observed in the literature as part of the synthesis method, successfully increased the T_c value to a usable temperature (right at room temperature), while also positively impacting ΔS. This demonstrates that optimizing synthesis

parameters can make materials previously disregarded for magnetic refrigeration into potential candidates for solid refrigerants.

This work successfully produced multiple materials with potential as solid refrigerants. The $La_{0.75}Ca_{0.25}MnO_3$ material sintered at 1100 °C without a decomposition stage, $La_{0.600}Ca_{0.40}MnO_3$ material synthesized with the determined optimal synthesis parameters, and the $La_{0.60}Ca_{0.28}Na_{0.12}MnO_3$ material all have promise and merit further testing – both determining magnetic heat capacity and adiabatic temperature change as well as practical testing in a prototype. The ideal parameters determined should be used for future synthesis of lanthanum manganites intended to be used as solid refrigerants. This used in combination with introducing sodium, or otherwise changing the ratio of Mn^{3+} to Mn^{4+} in order to tune the Zener Double Exchange interactions, has significant potential to lead to a material with comparable properties to the more costly materials discussed previously.

References

(1) Franco, V.; Blázquez, J. S.; Ipus, J. J.; Law, J. Y.; Moreno-Ramírez, L. M.; Conde, A. Magnetocaloric Effect: From Materials Research to Refrigeration Devices. *Progress in Materials Science* **2018**, *93*, 112–232. https://doi.org/10.1016/j.pmatsci.2017.10.005.

(2) Gschneidner, K. A.; Pecharsky, V. K. Thirty Years of near Room Temperature Magnetic Cooling: Where We Are Today and Future Prospects. *International Journal of Refrigeration* **2008**, *31* (6), 945–961. https://doi.org/10.1016/j.ijrefrig.2008.01.004.

(3) Phan, M.-H.; Yu, S.-C. Review of the Magnetocaloric Effect in Manganite Materials. *Journal of Magnetism and Magnetic Materials* **2007**, *308* (2), 325–340. https://doi.org/10.1016/j.jmmm.2006.07.025.

(4) Hunt, C. S. M.; Barua, R.; Carpenter, E. E. Influence of A-Site Cation Size-Disorder on the Magnetocaloric Response of $La_{0.6}Ca_xSr_{0.4-x}MnO_3$ Nanoparticles. *AIP Advances* **2020**, *10* (1), 015228. https://doi.org/10.1063/1.5129905.

(5) Hunt, C. S. M.; Carpenter, E. E. The Effect of Shifting Mn3+ to Mn4+ Ratio in La0.6CaxNa0.4-XMnO3 (X=0, 0.19, 0.28, 0.4) Nanomaterials. *J. Magn. Magn.* **2021**, No. In Review.

(6) Hunt, C. S. M.; Carpenter, E. E. Optimizing the Modified Sol-Gel Synthesis of La0.60Ca0.40MnO3 Nanomaterials for Magnetic Refrigeration Application. *Manuscript in preparation*.

(7) Hunt, C. S. M.; Blunt, B.; Carpenter, E. E. Effect of the Decomposition Stage on the Magnetic Properties of La0.75Ca0.25MnO3 Nanomaterials Prepared with a Modified Pechini Sol-Gel Synthesis. *J. Magn. Magn.* **2021**, No. In Review.

(8) *Transition to Sustainable Buildings: Strategies and Opportunities to 2050*; Energy Technology Perspectives; IEA Publications: Paris, France, 2013.

(9) International Energy Agency. *The Future of Cooling: Opportunities for Energy-Efficient Air Conditioning*; OECD, 2018. https://doi.org/10.1787/9789264301993-en.

(10) *Annual Energy Outlook 2017 with Projections to 2050*; U.S. Energy Information Administration, 2016; p 64.

(11) Zubair, S. M. Thermodynamics of a Vapor-Compression Refrigeration Cycle with Mechanical Subcooling. *Energy* **1994**, *19* (6), 707–715. https://doi.org/10.1016/0360-5442(94)90009-4.

(12) Aprea, C.; Greco, A.; Maiorino, A.; Masselli, C. Magnetic Refrigeration: An Eco-Friendly Technology for the Refrigeration at Room Temperature. *J. Phys.: Conf. Ser.* **2015**, *655*, 012026. https://doi.org/10.1088/1742-6596/655/1/012026.

(13) Franco, V.; Blázquez, J. S.; Ingale, B.; Conde, A. The Magnetocaloric Effect and Magnetic Refrigeration Near Room Temperature: Materials and Models. *Annu. Rev. Mater. Res.* **2012**, *42* (1), 305–342. https://doi.org/10.1146/annurev-matsci-062910-100356.

(14) Yari, M.; Sirousazar, M. Performance Analysis of the Ejector-Vapour Compression Refrigeration Cycle. *Proceedings of the Institution of Mechanical Engineers, Part A: Journal of Power and Energy* **2007**, *221* (8), 1089–1098. https://doi.org/10.1243/09576509JPE484.

(15) Zhao, B.; Hu, M.; Ao, X.; Chen, N.; Pei, G. Radiative Cooling: A Review of Fundamentals, Materials, Applications, and Prospects. *Applied Energy* **2019**, *236*, 489–513. https://doi.org/10.1016/j.apenergy.2018.12.018.

(16) Zhao, B.; Hu, M.; Ao, X.; Chen, N.; Xuan, Q.; Jiao, D.; Pei, G. Performance Analysis of a Hybrid System Combining Photovoltaic and Nighttime Radiative Cooling. *Applied Energy* **2019**, *252*, 113432. https://doi.org/10.1016/j.apenergy.2019.113432.

(17) *The Future of Cooling*; International Energy Agency, 2018.

(18) The Montreal Protocol on Substances That Deplete the Ozone Layer. *United States Department of State*.

(19) Enescu, D. Thermoelectric Refrigeration Principles. In *Bringing Thermoelectricity into Reality*; Aranguren, P., Ed.; InTech, 2018. https://doi.org/10.5772/intechopen.75439.
(20) Gschneidner, K. A.; Pecharsky, V. K. Magnetocaloric Materials. *Annual Review of Materials Research* **2000**, *30*, 387.
(21) Gutfleisch, O.; Willard, M. A.; Brück, E.; Chen, C. H.; Sankar, S. G.; Liu, J. P. Magnetic Materials and Devices for the 21st Century: Stronger, Lighter, and More Energy Efficient. *Adv. Mater.* **2011**, *23* (7), 821–842. https://doi.org/10.1002/adma.201002180.
(22) de Oliveira, N. A.; von Ranke, P. J. Theoretical Aspects of the Magnetocaloric Effect. *Physics Reports* **2010**, *489* (4–5), 89–159. https://doi.org/10.1016/j.physrep.2009.12.006.
(23) Griffith, L. D.; Mudryk, Y.; Slaughter, J.; Pecharsky, V. K. Material-Based Figure of Merit for Caloric Materials. *Journal of Applied Physics* **2018**, *123* (3), 034902. https://doi.org/10.1063/1.5004173.
(24) She, X.; Cong, L.; Nie, B.; Leng, G.; Peng, H.; Chen, Y.; Zhang, X.; Wen, T.; Yang, H.; Luo, Y. Energy-Efficient and -Economic Technologies for Air Conditioning with Vapor Compression Refrigeration: A Comprehensive Review. *Applied Energy* **2018**, *232*, 157–186. https://doi.org/10.1016/j.apenergy.2018.09.067.
(25) Kitanovski, A.; Egolf, P. W. Innovative Ideas for Future Research on Magnetocaloric Technologies. *International Journal of Refrigeration* **2010**, *33* (3), 449–464. https://doi.org/10.1016/j.ijrefrig.2009.11.005.
(26) Yu, B. F.; Gao, Q.; Zhang, B.; Meng, X. Z.; Chen, Z. Review on Research of Room Temperature Magnetic Refrigeration. *International Journal of Refrigeration* **2003**, *26* (6), 622–636. https://doi.org/10.1016/S0140-7007(03)00048-3.
(27) Ram, N. R.; Prakash, M.; Naresh, U.; Kumar, N. S.; Sarmash, T. S.; Subbarao, T.; Kumar, R. J.; Kumar, G. R.; Naidu, K. C. B. Review on Magnetocaloric Effect and Materials. *J Supercond Nov Magn* **2018**, *31* (7), 1971–1979. https://doi.org/10.1007/s10948-018-4666-z.
(28) Salamon, M. B.; Lin, P.; Chun, S. H. Colossal Magnetoresistance Is a Griffiths Singularity. *Phys. Rev. Lett.* **2002**, *88* (19), 197203. https://doi.org/10.1103/PhysRevLett.88.197203.
(29) Aharoni, A. *Introduction to the Theory of Ferromagnetism*; Oxford : Clarendon Press ; New York : Oxford University Press, 1996.
(30) Magnetic Anisotropy. In *Introduction to Magnetic Materials*; John Wiley & Sons, Ltd, 2008; pp 197–239. https://doi.org/10.1002/9780470386323.ch7.
(31) Skomski, R. Nanomagnetics. *J. Phys.: Condens. Matter* **2003**, *15*, R841.
(32) Gottschall, T.; Skokov, K. P.; Fries, M.; Taubel, A.; Radulov, I.; Scheibel, F.; Benke, D.; Riegg, S.; Gutfleisch, O. Making a Cool Choice: The Materials Library of Magnetic Refrigeration. *Advanced Energy Materials* **2019**, *9* (34), 1901322. https://doi.org/10.1002/aenm.201901322.
(33) Ambler, E.; Hudson, R. P. Magnetic Cooling. *Reports on Progress in Physics* **1955**, *18*, 251.
(34) Brück, E. Developments in Magnetocaloric Refrigeration. *J. Phys. D: Appl. Phys.* **2005**, *38* (23), R381–R391. https://doi.org/10.1088/0022-3727/38/23/R01.
(35) Andreenko, A. S.; Belov, K. P.; Nikitin, S. A.; Tishin, A. M. Magnetocaloric Effects in Rare-Earth Magnetic Materials. **1989**, 17.
(36) Zarkevich, N. A.; Zverev, V. I. Viable Materials with a Giant Magnetocaloric Effect. *Crystals* **2020**, *10* (9), 815. https://doi.org/10.3390/cryst10090815.
(37) Cao, Y.; Yuan, Y.; Shang, Y.; Zverev, V. I.; Gimaev, R. R.; Barua, R.; Hadimani, R. L.; Mei, L.; Guo, G.; Fu, H. Phase Transition and Magnetocaloric Effect in Particulate Fe-Rh Alloys. *J Mater Sci* **2020**, *55* (27), 13363–13371. https://doi.org/10.1007/s10853-020-04921-y.
(38) Algarabel, P. A.; Ibarra, M. R.; Marquina, C.; del Moral, A.; Galibert, J.; Iqbal, M.; Askenazy, S. Giant Room-temperature Magnetoresistance in the FeRh Alloy. *Appl. Phys. Lett.* **1995**, *66* (22), 3061–3063. https://doi.org/10.1063/1.114278.

(39) Fujita, A.; Koiwai, S.; Fujieda, S.; Fukamichi, K.; Kobayashi, T.; Tsuji, H.; Kaji, S.; Saito, A. T. Magnetocaloric Effect in Spherical La(FexSi1−x)13 and Their Hydrides for Active Magnetic Regenerator-Type Refrigerator. *Journal of Applied Physics* **2009**, *105* (7), 07A936. https://doi.org/10.1063/1.3070658.
(40) Ahmim, S.; Almanza, M.; Loyau, V.; Pasko, A.; Mazaleyrat, F.; LoBue, M. A Thermal Energy Harvester Using LaFeSi Magnetocaloric Materials. *IEEE Trans. Magn.* **2020**, 1–1. https://doi.org/10.1109/TMAG.2020.3008753.
(41) Katter, M.; Zellmann, V.; Reppel, G. W.; Uestuener, K. Magnetocaloric Properties of ${\hbox{La}}({\hbox{Fe}},{\hbox{Co}},{\hbox{Si}})_{13}$ Bulk Material Prepared by Powder Metallurgy. *IEEE Trans. Magn.* **2008**, *44* (11), 3044–3047. https://doi.org/10.1109/TMAG.2008.2002523.
(42) GschneidnerJr, K. A.; Pecharsky, V. K.; Tsokol, A. O. Recent Developments in Magnetocaloric Materials. *Rep. Prog. Phys.* **2005**, *68* (6), 1479–1539. https://doi.org/10.1088/0034-4885/68/6/R04.
(43) Dan'kov, S. Yu.; Tishin, A. M.; Pecharsky, V. K.; Gschneidner, K. A. Magnetic Phase Transitions and the Magnetothermal Properties of Gadolinium. *Phys. Rev. B* **1998**, *57* (6), 3478–3490. https://doi.org/10.1103/PhysRevB.57.3478.
(44) Zhong, W. MAGNETOCALORIC PROPERTIES OF Na-SUBSTITUTED PEROVSKITE-TYPE MANGANESE OXIDES. *106* (1), 4.
(45) de Gennes, P.-G. Effects of Double Exchange in Magnetic Crystals. *Phys. Rev.* **1960**, *118* (1), 141–154. https://doi.org/10.1103/PhysRev.118.141.
(46) Chen, W.; Zhong, W.; Hou, D.; Ding, W.; Du, Y.; Yan, Q. Structure and Magnetocaloric Properties in Perovskitelike $La_{1-x}Na_xMnO_z$ Powders. *Chinese Phys. Lett.* **1998**, *15* (2), 134–136. https://doi.org/10.1088/0256-307X/15/2/021.
(47) Zhang, X. X.; Tejada, J.; Xin, Y.; Sun, G. F.; Wong, K. W.; Bohigas, X. Magnetocaloric Effect in $La_{0.67}Ca_{0.33}MnO_{\delta}$ and $La_{0.60}Y_{0.07}Ca_{0.33}MnO_{\delta}$ Bulk Materials. *Appl. Phys. Lett.* **1996**, *69* (23), 3596–3598. https://doi.org/10.1063/1.117218.
(48) Bohigas, X.; Tejada, J.; del Barco, E.; Zhang, X. X.; Sales, M. Tunable Magnetocaloric Effect in Ceramic Perovskites. *Appl. Phys. Lett.* **1998**, *73* (3), 390–392. https://doi.org/10.1063/1.121844.
(49) Schiffer, P.; Ramirez, A. P.; Bao, W.; Cheong, S.-W. Low Temperature Magnetoresistance and the Magnetic Phase Diagram of La 1 − x Ca x MnO 3. *Phys. Rev. Lett.* **1995**, *75* (18), 3336–3339. https://doi.org/10.1103/PhysRevLett.75.3336.
(50) Zener, C. Interaction between the d -Shells in the Transition Metals. II. Ferromagnetic Compounds of Manganese with Perovskite Structure. *Phys. Rev.* **1951**, *82* (3), 403–405. https://doi.org/10.1103/PhysRev.82.403.
(51) Wei, Z.; Chak-Tong, A.; You-Wei, D. Review of Magnetocaloric Effect in Perovskite-Type Oxides. *Chin. Phys. B* **2013**, *22* (5), 057501.
(52) Anderson, P. W.; Hasegawa, H. Considerations on Double Exchange. *Phys. Rev.* **1955**, *100* (2), 675–681. https://doi.org/10.1103/PhysRev.100.675.
(53) Azhar, M.; Mostovoy, M. Incommensurate Spiral Order from Double-Exchange Interactions. *PHYSICAL REVIEW LETTERS* **2017**, 5.
(54) Guo, Z. B.; Du, Y. W.; Zhu, J. S.; Huang, H.; Ding, W. P.; Feng, D. Large Magnetic Entropy Change in Perovskite-Type Manganese Oxides. *Phys. Rev. Lett.* **1997**, *78* (6), 1142–1145. https://doi.org/10.1103/PhysRevLett.78.1142.
(55) Guo, Z. B.; Zhang, J. R.; Huang, H.; Ding, W. P.; Du, Y. W. Large Magnetic Entropy Change in La0.75Ca0.25MnO3. *Appl. Phys. Lett.* **1997**, *70* (7), 904–905. https://doi.org/10.1063/1.118309.
(56) Andrade, V. M.; Vivas, R. J. C.; Pedro, S. S.; Tedesco, J. C. G.; Rossi, A. L.; Coelho, A. A.; Rocco, D. L.; Reis, M. S. Magnetic and Magnetocaloric Properties of La 0.6 Ca 0.4 MnO 3 Tunable by Particle

Size and Dimensionality. *Acta Materialia* **2016**, *102*, 49–55. https://doi.org/10.1016/j.actamat.2015.08.080.
(57) Guo, Z. B.; Shen, Y. T.; Du, Y. W. Magnetic Entropy Change in La0.75Ca0.25-XSrxMnO3 Perovskites. *Solid State Commun.* **1998**, *105* (2), 89–92. https://doi.org/10.1016/S0038-1098(97)10064-3.
(58) Morelli, D. T.; Mance, A. M.; Mantese, J. V.; Micheli, A. L. Magnetocaloric Properties of Doped Lanthanum Manganite Films. *Journal of Applied Physics* **1996**, *79* (1), 373–375. https://doi.org/10.1063/1.360840.
(59) Zhong, W.; Chen, W.; Ding, W.; Zhang, N.; Du, Y.; Yan, Q. Magnetocaloric Properties of Na-Substituted Perovskite-Type Manganese Oxides. *Solid State Communications* **1998**, *106* (1), 55–58. https://doi.org/10.1016/S0038-1098(97)10239-3.
(60) Phan, M. H.; Tian, S. B.; Hoang, D. Q.; Yu, S. C.; Nguyen, C.; Ulyanov, A. N. Large Magnetic-Entropy Change above 300K in CMR Materials. *Journal of Magnetism and Magnetic Materials* **2003**, *258–259*, 309–311. https://doi.org/10.1016/S0304-8853(02)01151-4.
(61) Alzahrani, B.; Hsini, M.; Hcini, S.; Boudard, M.; Dhahri, A.; Bouazizi, M. L. Study of the Magnetocaloric Effect by Means of Theoretical Models in La0.6Ca0.2Na0.2MnO3 Manganite Compound. *J Low Temp Phys* **2020**. https://doi.org/10.1007/s10909-020-02455-w.
(62) Rout, G. C.; Panda, S.; Behera, S. N. The Effect of Band Jahn–Teller Distortion on the Magnetoresistivity of Manganites: A Model Study. *J. Phys.: Condens. Matter* **2011**, *23* (39), 396001. https://doi.org/10.1088/0953-8984/23/39/396001.
(63) Rościszewski, K.; Oleś, A. M. Jahn–Teller Distortions and the Magnetic Order in the Perovskite Manganites. *J. Phys.: Condens. Matter* **2010**, *22* (42), 425601. https://doi.org/10.1088/0953-8984/22/42/425601.
(64) Maezono, R.; Nagaosa, N. Jahn-Teller Effect and Electron Correlation in Manganites. *Phys. Rev. B* **2003**, *67* (6), 064413. https://doi.org/10.1103/PhysRevB.67.064413.
(65) Chu, Y. Y.; Wu, H. H.; Liu, S. C.; Lin, H.-H.; Matsuno, J.; Takagi, H.; Huang, J. H.; van den Brink, J.; Chen, C. T.; Huang, D. J. Enhancement of the Jahn-Teller Distortion by Magnetization in Manganites. *Appl. Phys. Lett.* **2012**, *100* (11), 112406. https://doi.org/10.1063/1.3691946.
(66) Yi, D.; Lu, N.; Chen, X.; Shen, S.; Yu, P. Engineering Magnetism at Functional Oxides Interfaces: Manganites and Beyond. *J. Phys.: Condens. Matter* **2017**, *29* (44), 443004. https://doi.org/10.1088/1361-648X/aa824d.
(67) Koçak, A. B.; Varignon, J.; Lemal, S.; Ghosez, P.; Lepetit, M.-B. Control of the Orbital Ordering in Manganite Superlattices and Impact on Properties. *Phys. Rev. B* **2017**, *96* (12), 125155. https://doi.org/10.1103/PhysRevB.96.125155.
(68) Faaland, S.; Knudsen, K. D.; Einarsrud, M.-A.; Rørmark, L.; Høier, R.; Grande, T. Structure, Stoichiometry, and Phase Purity of Calcium Substituted Lanthanum Manganite Powders. *Journal of Solid State Chemistry* **1998**, *140* (2), 320–330. https://doi.org/10.1006/jssc.1998.7894.
(69) Lipham, N. D.; Tsoi, G. M.; Wenger, L. E. Synthesis and Characterization of Sr-Doped Lanthanum Manganite Nanoparticles. *IEEE Trans. Magn.* **2007**, *43* (6), 3088–3090. https://doi.org/10.1109/TMAG.2007.893850.
(70) Sethulakshmi, N.; Al Omari, I. A.; Anantharaman, M. R. Influence of Higher Sodium Substitutions on Magnetic Entropy Change and Transition Temperature in Lanthanum Manganites. *Bull Mater Sci* **2015**, *38* (6), 1545–1552. https://doi.org/10.1007/s12034-015-0983-z.
(71) Song, H.; Kim, W.; Kwon, S.-J.; Kang, J. Magnetic and Electronic Properties of Transition-Metal-Substituted Perovskite Manganites—La0.7Ca0.3Mn0.95X0.05O3 „XÄFe,Co,Ni…. *J. Appl. Phys.* **2001**, *89* (6), 6.
(72) Choura-Maatar, S.; Nofal, M. M.; M'nassri, R.; Cheikhrouhou-Koubaa, W.; Chniba-Boudjada, N.; Cheikhrouhou, A. Enhancement of the Magnetic and Magnetocaloric Properties by Na

Substitution for Ca of La0.8Ca0.2MnO3 Manganite Prepared via the Pechini-Type Sol–Gel Process. *J Mater Sci: Mater Electron* **2020**, *31* (2), 1634–1645. https://doi.org/10.1007/s10854-019-02680-4.

(73) Phan, M.-H.; Tian, S.-B.; Yu, S.-C.; Ulyanov, A. N. Magnetic and Magnetocaloric Properties of La0.7Ca0.3-XBaxMnO3 Compounds. *Journal of Magnetism and Magnetic Materials* **2003**, 5.

(74) Chen, L.; Zhang, C.; Chen, Y.; Chen, Y.; Niu, W.; Wang, P.; Du, J.; Xu, Y.; Zhang, R.; Wang, X. Strain-Driven Lattice Distortion and the Resultant Magnetic Properties of $La_{0.7}Sr_{0.3}MnO_3$/$BaTiO_3$ Superlattices. *Appl. Phys. Lett.* **2019**, *115* (20), 201604. https://doi.org/10.1063/1.5119736.

(75) Das, S.; Amaral, J. S.; De, K.; Willinger, M.; Gonçalves, J. N.; Roy, A.; Dhak, P.; Giri, S.; Majumder, S.; Silva, C. J. R.; Gomes, M. J. M.; Mahapatra, P. K.; Amaral, V. S. Strain Induced Enhanced Ferromagnetic Behavior in Inhomogeneous Low Doped $La_{0.95}Sr_{0.05}MnO_{3+\delta}$. *Appl. Phys. Lett.* **2013**, *102* (11), 112408. https://doi.org/10.1063/1.4793657.

(76) Kim, Y.; Ryu, S.; Jeen, H. Strain-Effected Physical Properties of Ferromagnetic Insulating $La_{0.88}Sr_{0.12}MnO_3$ Thin Films. *RSC Adv.* **2019**, *9* (5), 2645–2649. https://doi.org/10.1039/C8RA09851D.

(77) Ji, T.; Fang, J.; Golob, V.; Tang, J.; O'Connor, C. J. Preparation and Magnetic Properties of La0.9Ca0.1MnO3 Nanoparticles at 300 °C. *Journal of Applied Physics* **2002**, *92* (11), 6833–6836. https://doi.org/10.1063/1.1513880.

(78) Manh, D. H.; Phong, P. T.; Thanh, T. D.; Nam, D. N. H.; Hong, L. V.; Phuc, N. X. Size Effects and Interactions in La0.7Ca0.3MnO3 Nanoparticles. *Journal of Alloys and Compounds* **2011**, *509* (5), 1373–1377. https://doi.org/10.1016/j.jallcom.2010.10.104.

(79) Hueso, L. E.; Sande, P.; Miguens, D. R.; Rivas, J. Tuning of the Magnetocaloric Effect in LCMO Perovskites. *J. Appl. Phys.* **2002**, *91* (12), 9943–9947. https://doi.org/10.1063/1.1476972.

(80) Zhou, S.; Guo, Y.; Zhao, J.; He, L.; Shi, L. Size-Induced Griffiths Phase and Second-Order Ferromagnetic Transition in $Sm_{0.5}Sr_{0.5}MnO_3$ Nanoparticles. *J. Phys. Chem. C* **2011**, *115* (5), 1535–1540. https://doi.org/10.1021/jp108553r.

(81) Phong, P. T.; Ngan, L. T. T.; Dang, N. V.; Nguyen, L. H.; Nam, P. H.; Thuy, D. M.; Tuan, N. D.; Bau, L. V.; Lee, I. J. Griffiths-like Phase, Critical Behavior near the Paramagnetic-Ferromagnetic Phase Transition and Magnetic Entropy Change of Nanocrystalline La0.75Ca0.25MnO3. *Journal of Magnetism and Magnetic Materials* **2018**, *449*, 558–566. https://doi.org/10.1016/j.jmmm.2017.10.103.

(82) Phong, P. T.; Manh, D. H.; Hoan, L. C.; Ngai, T. V.; Phuc, N. X.; Lee, I.-J. Particle Size Effects on La0.7Ca0.3MnO3: Griffiths Phase-like Behavior and Magnetocaloric Study. *Journal of Alloys and Compounds* **2016**, *662*, 557–565. https://doi.org/10.1016/j.jallcom.2015.12.052.

(83) Phong, P. T.; Ngan, L. T. T.; Bau, L. V.; Phuc, N. X.; Nam, P. H.; Phong, L. T. H.; Dang, N. V.; Lee, I.-J. Magnetic Field Dependence of Griffith Phase and Critical Behavior in La0.8Ca0.2MnO3 Nanoparticles. *Journal of Magnetism and Magnetic Materials* **2019**, *475*, 374–381. https://doi.org/10.1016/j.jmmm.2018.11.122.

(84) Krishna Murthy, J.; Devi Chandrasekhar, K.; Venimadhav, A. Observation of Griffiths-like Phase and Its Tunability in La2Ni1−xCoxMnO6 (0≤x≤1) Nanoparticles. *Journal of Magnetism and Magnetic Materials* **2016**, *418*, 2–8. https://doi.org/10.1016/j.jmmm.2016.02.074.

(85) Griffiths, R. B. Nonanalytic Behavior Above the Critical Point in a Random Ising Ferromagnet. *Phys. Rev. Lett.* **1969**, *23* (1), 17–19. https://doi.org/10.1103/PhysRevLett.23.17.

(86) Guedri, A.; Mnefgui, S.; Hcini, S.; Hlil, E. K.; Dhahri, A. B-Site Substitution Impact on Structural and Magnetocaloric Behavior of La0.55Pr0.1Sr0.35Mn1-XTixO3 Manganites. *Journal of Solid State Chemistry* **2021**, *297*, 122046. https://doi.org/10.1016/j.jssc.2021.122046.

(87) Kumar, A.; Kumari, K.; Koo, B. H. Investigating the Effects of B-Site Cr Doping on the Structural, Magnetic and Magnetocaloric Properties of La1.4Ca1.6Mn2-XCrxO7 ($0 \le x \le 0.4$) Bilayer Manganites. *Functional Composites and Structures* **2021**, *in press*.

(88) Zaidi, N.; Elabassi, M.; Selmi, M.; Hlil, E. K. Structural Characterization and Magnetic Interactions of La0.7Sr0.25Na0.05Mn1 - XAlxO3. *J Supercond Nov Magn* **2020**. https://doi.org/10.1007/s10948-020-05521-2.
(89) Pechini, M. US3330697. 304434, July 11, 1967.
(90) Sunde, T. O. L.; Grande, T.; Einarsrud, M.-A. Modified Pechini Synthesis of Oxide Powders and Thin Films. In *Handbook of Sol-Gel Science and Technology*; Klein, L., Aparicio, M., Jitianu, A., Eds.; Springer International Publishing: Cham, 2016; pp 1–30. https://doi.org/10.1007/978-3-319-19454-7_130-1.
(91) Lin, J.; Yu, M.; Lin, C.; Liu, X. Multiform Oxide Optical Materials via the Versatile Pechini-Type Sol−Gel Process: Synthesis and Characteristics. *J. Phys. Chem. C* **2007**, *111* (16), 5835–5845. https://doi.org/10.1021/jp070062c.
(92) Kakihana, M.; Domen, K. The Synthesis of Photocatalysts Using the Polymerizable-Complex Method. *MRS Bull.* **2000**, *25* (9), 27–31. https://doi.org/10.1557/mrs2000.176.
(93) Kakihana, M.; Yoshimura, M. Synthesis and Characteristics of Complex Multicomponent Oxides Prepared by Polymer Complex Method. *BCSJ* **1999**, *72* (7), 1427–1443. https://doi.org/10.1246/bcsj.72.1427.
(94) Dimesso, L. Pechini Processes: An Alternate Approach of the Sol–Gel Method, Preparation, Properties, and Applications. In *Handbook of Sol-Gel Science and Technology*; Klein, L., Aparicio, M., Jitianu, A., Eds.; Springer International Publishing: Cham, 2016; pp 1–22. https://doi.org/10.1007/978-3-319-19454-7_123-1.
(95) Katelnikovas, A.; Barkauskas, J.; Ivanauskas, F.; Beganskiene, A.; Kareiva, A. Aqueous Sol-Gel Synthesis Route for the Preparation of YAG: Evaluation of Sol-Gel Process by Mathematical Regression Model. *J Sol-Gel Sci Technol* **2007**, *41* (3), 193–201. https://doi.org/10.1007/s10971-006-9002-6.
(96) Kessler, V. G. The Chemistry behind the Sol–Gel Synthesis of Complex Oxide Nanoparticles for Bio-Imaging Applications. *J Sol-Gel Sci Technol* **2009**, *51* (3), 264–271. https://doi.org/10.1007/s10971-009-1946-x.
(97) Tsui, M. H. M.; Dryer, D. T.; El-Gendy, A. A.; Carpenter, E. E. Enhanced near Room Temperature Magnetocaloric Effect in La $_{0.6}$ Ca $_{0.4}$ MnO $_{3}$ for Magnetic Refrigeration Application. *RSC Adv.* **2017**, *7* (74), 46589–46593. https://doi.org/10.1039/C7RA06619H.
(98) Oumezzine, M.; Peña, O.; Guizouarn, T.; Lebullenger, R.; Oumezzine, M. Impact of the Sintering Temperature on the Structural, Magnetic and Electrical Transport Properties of Doped La0,67Ba0,33Mn0,9Cr0,1O3 Manganite. *Journal of Magnetism and Magnetic Materials* **2012**, *324* (18), 2821–2828. https://doi.org/10.1016/j.jmmm.2012.04.017.
(99) Ravi, S.; Karthikeyan, A. Effect of Calcination Temperature on La0.7Sr0.3MnO3 Nanoparticles Synthesized with Modified Sol-Gel Route. *Physics Procedia* **2014**, *54*, 45–54. https://doi.org/10.1016/j.phpro.2014.10.035.
(100) Lee, S. R.; Anwar, M. S.; Ahmed, F.; Koo, B. H. Effect of Sintering Temperature on Structure, Magnetic and Magnetocaloric Properties of La0.6Ca0.4MnO3 Manganite. *Transactions of Nonferrous Metals Society of China* **2014**, *24*, s141–s145. https://doi.org/10.1016/S1003-6326(14)63301-X.
(101) Faraji, M.; Yamini, Y.; Rezaee, M. Magnetic Nanoparticles: Synthesis, Stabilization, Functionalization, Characterization, and Applications. *JICS* **2010**, *7* (1), 1–37. https://doi.org/10.1007/BF03245856.
(102) Mourdikoudis, S.; Pallares, R. M.; Thanh, N. T. K. Characterization Techniques for Nanoparticles: Comparison and Complementarity upon Studying Nanoparticle Properties. *Nanoscale* **2018**, *10* (27), 12871–12934. https://doi.org/10.1039/C8NR02278J.

(103) Cheetham, A. K. Laboratory X-Ray Powder Diffraction. In *Structure Determination from Powder Diffraction Data*; Louer, D., Shankland, K., McCusker, L. B., Bärlocher, C., Eds.; Oxford University Press, 2006; pp 29–50.
(104) Cheetham, A. K. Structure Determination from Powder Diffraction Data: An Overview. In *Structure Determination from Powder Diffraction Data*; David, W. I. F., Shankland, K., McCusker, L. B., Bärlocher, C., Eds.; Oxford University Press, 2006; pp 13–28. https://doi.org/10.1093/acprof:oso/9780199205530.003.0002.
(105) *Surface Analysis: The Principal Techniques*, 2nd ed.; Vickerman, J. C., Gilmore, I. S., Eds.; Wiley: Chichester, U.K, 2009.
(106) Hammond, C. *The Basics of Crystallography and Diffraction: Fourth Edition*; Oxford University Press, 2015. https://doi.org/10.1093/acprof:oso/9780198738671.001.0001.
(107) Harris, K. D. M.; Tremayne, M. Crystal Structure Determination from Powder Diffraction Data. *Chem. Mater.* **1996**, *8* (11), 2554–2570. https://doi.org/10.1021/cm960218d.
(108) Nørlund Christensen, A.; Lehmann, M.; Nielsen, M. Solving Crystal Structures from Powder Diffraction Data. *Aust. J. Phys.* **1985**, *38* (3), 497. https://doi.org/10.1071/PH850497.
(109) Cheetham, A. K.; Wilkinson, A. P. Structure Determination and Refinement with Synchrotron X-Ray Powder Diffraction Data. *Journal of Physics and Chemistry of Solids* **1991**, *52* (10), 1199–1208. https://doi.org/10.1016/0022-3697(91)90194-5.
(110) Calvin, S.; Luo, S. X.; Caragianis-Broadbridge, C.; McGuinness, J. K.; Anderson, E.; Lehman, A.; Wee, K. H.; Morrison, S. A.; Kurihara, L. K. Comparison of Extended X-Ray Absorption Fine Structure and Scherrer Analysis of x-Ray Diffraction as Methods for Determining Mean Sizes of Polydisperse Nanoparticles. *Appl. Phys. Lett.* **2005**, *87* (23), 233102. https://doi.org/10.1063/1.2137872.
(111) Vorokh, A. S. Scherrer Formula: Estimation of Error in Determining Small Nanoparticle Size. *Nanosystems: Phys. Chem. Math.* **2018**, 364–369. https://doi.org/10.17586/2220-8054-2018-9-3-364-369.
(112) Rietveld, H. M. A Profile Refinement Method for Nuclear and Magnetic Structures. *J Appl Crystallogr* **1969**, *2* (2), 65–71. https://doi.org/10.1107/S0021889869006558.
(113) Schimanke, G.; Martin, M. In Situ XRD Study of the Phase Transition of Nanocrystalline Maghemite (g-Fe2O3) to Hematite (a-Fe2O3). *Solid State Ionics* **2000**, 6.
(114) Speakman, S. A. Fundamentals of Rietveld Refinement III. Refinement of a Mixture.
(115) Toby, B. H. *R* Factors in Rietveld Analysis: How Good Is Good Enough? *Powder Diffr.* **2006**, *21* (1), 67–70. https://doi.org/10.1154/1.2179804.
(116) McCusker, L. B.; Von Dreele, R. B.; Cox, D. E.; Louër, D.; Scardi, P. Rietveld Refinement Guidelines. *J Appl Crystallogr* **1999**, *32* (1), 36–50. https://doi.org/10.1107/S0021889898009856.
(117) Foner, S. Review of Magnetometry. *IEEE Trans. Magn.* **1981**, *17* (6), 3358–3363. https://doi.org/10.1109/TMAG.1981.1061748.
(118) Foner, S. The Vibrating Sample Magnetometer: Experiences of a Volunteer (Invited). *J. Appl. Phys.* **1996**, *79* (8), 4740. https://doi.org/10.1063/1.361657.
(119) Foner, S. Sensitivity of Vibrating Sample Magnetometers-and How to Increase Sensitivity If Needed. *Review of Scientific Instruments* **1974**, *45* (9), 1181–1183. https://doi.org/10.1063/1.1686846.
(120) Foner, S. Vibrating Sample Magnetometer. *Review of Scientific Instruments* **1956**, *27*, 548. https://doi.org/10.1063/1.1715636.
(121) Ho, T. A.; Thanh, T. D.; Phan, T.-L.; Oh, S. K.; Yu, S.-C. Effect of Crystallite Size on the Thickness of Nonmagnetic Shell and Magnetic Properties of La0.7Ca0.3MnO3. *J Supercond Nov Magn* **2015**, *28* (3), 891–894. https://doi.org/10.1007/s10948-014-2763-1.

(122) Zhao, Y.-P.; Gamache, R. M.; Wang, G.-C.; Lu, T.-M.; Palasantzas, G.; De Hosson, J. Th. M. Effect of Surface Roughness on Magnetic Domain Wall Thickness, Domain Size, and Coercivity. *Journal of Applied Physics* **2001**, *89* (2), 1325–1330. https://doi.org/10.1063/1.1331065.
(123) Mohammed, A.; Abdullah, A. Scanning Electron Microscopy (SEM): A Review. 10.
(124) Vernon-Parry, K. D. Scanning Electron Microscopy: An Introduction. *III-Vs Review* **2000**, *13* (4), 40–44. https://doi.org/10.1016/S0961-1290(00)80006-X.
(125) Wang, Z. L. Transmission Electron Microscopy of Shape-Controlled Nanocrystals and Their Assemblies. *J. Phys. Chem. B* **2000**, *104* (6), 1153–1175. https://doi.org/10.1021/jp993593c.
(126) Durrant, S. F. Laser Ablation Inductively Coupled Plasma Mass Spectrometry: Achievements, Problems, Prospects. *J. Anal. At. Spectrom.* **1999**, *14* (9), 1385–1403. https://doi.org/10.1039/a901765h.
(127) Günther, D.; Hattendorf, B. Solid Sample Analysis Using Laser Ablation Inductively Coupled Plasma Mass Spectrometry. *TrAC Trends in Analytical Chemistry* **2005**, *24* (3), 255–265. https://doi.org/10.1016/j.trac.2004.11.017.
(128) Tognoni, E.; Hidalgo, M.; Canals, A.; Cristoforetti, G.; Legnaioli, S.; Palleschi, V. Towards a Calibration-Less ICP-AES Method for the Determination of Trace Elements in Aqueous Solutions: Double Ratio Plasma Diagnostics Combined with an Internal Standard. *J. Anal. At. Spectrom.* **2009**, *24* (5), 655. https://doi.org/10.1039/b822740c.
(129) Biesinger, M. C.; Payne, B. P.; Grosvenor, A. P.; Lau, L. W. M.; Gerson, A. R.; Smart, R. St. C. Resolving Surface Chemical States in XPS Analysis of First Row Transition Metals, Oxides and Hydroxides: Cr, Mn, Fe, Co and Ni. *Applied Surface Science* **2011**, *257* (7), 2717–2730. https://doi.org/10.1016/j.apsusc.2010.10.051.
(130) Gutiérrez, M. P.; Olivares, J. H.; Betancourt, I.; Morales, F. Structural and Magnetic Properties of $La_{0.72}(Ca_{1-x}Sr_{x})_{0.28}MnO_{3}$ (x = 0 to 1) Manganites. *J. Mater. Res.* **2009**, *24* (4), 1585–1589. https://doi.org/10.1557/jmr.2009.0182.
(131) Henchiri, C.; Hamdi, R.; Mnasri, T.; Valente, M. A.; Prezas, P. R.; Dhahri, E. Structural and Magnetic Properties of La1-X□xMnO3 (x = 0.1; 0.2 and 0.3) Manganites. *Appl. Phys. A* **2019**, *125* (10), 725. https://doi.org/10.1007/s00339-019-2980-3.
(132) Millini, R.; Gagliardi, M. F.; Piro, G. Structure, Stoichiometry and Phase Purity of Strontium-Doped Lanthanum Manganite Powders. *JOURNAL OF MATERIALS SCIENCE* **1994**, *29* (15), 4065–4069. https://doi.org/10.1007/BF00355971.
(133) Shankar, K. S.; Kar, S.; Subbanna, G. N.; Raychaudhuri, A. K. Enhanced Ferromagnetic Transition Temperature in Nanocrystalline Lanthanum Calcium Manganese Oxide (La0.67Ca0.33MnO3). *Solid State Communications* **2004**, *129* (7), 479–483. https://doi.org/10.1016/j.ssc.2003.10.029.
(134) Nasri, M.; Triki, M.; Dhahri, E.; Hlil, E. K. Critical Behavior in Sr-Doped Manganites La0.6Ca0.4−xSrxMnO3. *Journal of Alloys and Compounds* **2013**, *546*, 84–91. https://doi.org/10.1016/j.jallcom.2012.08.018.
(135) Zhang, Y.; Xu, X. Relative Cooling Power Modeling of Lanthanum Manganites Using Gaussian Process Regression. *RSC Adv.* **2020**, *10* (35), 20646–20653. https://doi.org/10.1039/D0RA03031G.
(136) Hwang, H. Y.; Cheong, S.-W.; Radaelli, P. G.; Marezio, M.; Batlogg, B. Lattice Effects on the Magnetoresistance in Doped LaMn O 3. *Phys. Rev. Lett.* **1995**, *75* (5), 914–917. https://doi.org/10.1103/PhysRevLett.75.914.
(137) Elghoul, N.; Wali, M.; Kraiem, S.; Rahmouni, H.; Dhahri, E.; Khirouni, K. Sodium Deficiency Effect on the Transport Properties of La0.8Na0.2−x□xMnO3 Manganites. *Physica B: Condensed Matter* **2015**, *478*, 108–112. https://doi.org/10.1016/j.physb.2015.09.006.
(138) Woodward, R. C.; Heeris, J.; St. Pierre, T. G.; Saunders, M.; Gilbert, E. P.; Rutnakornpituk, M.; Zhang, Q.; Riffle, J. S. A Comparison of Methods for the Measurement of the Particle-Size

Distribution of Magnetic Nanoparticles. *J Appl Cryst* **2007**, *40* (s1), s495–s500. https://doi.org/10.1107/S002188980700091X.

(139) Ho, T. A.; Thanh, T. D.; Ho, T. O.; Phan, M. H.; Phan, T.-L.; Yu, S. C. Magnetic Properties and Magnetocaloric Effect in Fe-Doped La $_{0.6}$ Ca $_{0.4}$ MnO $_{3}$ with Short-Range Ferromagnetic Order. *Journal of Applied Physics* **2015**, *117* (17), 17A724. https://doi.org/10.1063/1.4915103.

(140) Nasri, A.; Zouari, S.; Ellouze, M.; Hlil, E. K.; Elhalouani, F. X-Ray Diffraction, Magnetic and Magnetocaloric Properties of La0.6Ca0.4Mn1−xFexO3 (0 ≤ x ≤ 0.3) Manganites Prepared by the Sol-Gel Method. *Eur. Phys. J. Plus* **2014**, *129* (8), 180. https://doi.org/10.1140/epjp/i2014-14180-5.

(141) Fatnassi, D.; Rehspringer, J. L.; Hlil, E. K.; Niznansky, D.; Ellouze, M.; Elhalouani, F. Structural and Magnetic Properties of Nanosized La0.8Ca0.2Mn1−xFexO3 Particles (0 ≤ x ≤ 0.2) Prepared by Sol–Gel Method. *J Supercond Nov Magn* **2015**, *28* (8), 2401–2408. https://doi.org/10.1007/s10948-015-3030-9.

(142) Motta, M.; Deimling, C. V.; Saeki, M. J.; Lisboa-Filho, P. N. Chelating Agent Effects in the Synthesis of Mesoscopic-Size Superconducting Particles. *J Sol-Gel Sci Technol* **2008**, *46* (2), 201–207. https://doi.org/10.1007/s10971-007-1673-0.

(143) Bogdanoviciene, I.; Tõnsuaadu, K.; Mikli, V.; Grigoraviciute-Puroniene, I.; Beganskiene, A.; Kareiva, A. PH Impact on the Sol-Gel Preparation of Calcium Hydroxyapatite, Ca10(PO4)6(OH)2, Using a Novel Complexing Agent, DCTA. *Open Chemistry* **2010**, *8* (6), 1323–1330. https://doi.org/10.2478/s11532-010-0113-0.

(144) Montoya, I. A.; Viveros, T.; Dom**&#65533;**nguez, J. M.; Canales, L. A.; Schifter, I. On the Effects of the Sol-Gel Synthesis Parameters on Textural and Structural Characteristics of TiO2. *Catal Lett* **1992**, *15* (1–2), 207–217. https://doi.org/10.1007/BF00770913.

(145) Macedo, D. A.; Cesário, M. R.; Cela, B.; Melo, D. M. A.; Paskocimas, C. A.; Martinelli, A. E.; Nascimento, R. M. Influence of Polymerizing Agent on Structure and Spectroscopic Properties of Nano-Crystalline La0.8Sr0.2MnO3 Powders. *Cryst. Res. Technol.* **2010**, *45* (11), 1166–1170. https://doi.org/10.1002/crat.201000224.

(146) Xi, S.; Lu, W.; Sun, Y. Magnetic Properties and Magnetocaloric Effect of La $_{0.8}$ Ca $_{0.2}$ MnO $_{3}$ Nanoparticles Tuned by Particle Size. *Journal of Applied Physics* **2012**, *111* (6), 063922. https://doi.org/10.1063/1.3699037.

(147) Dimesso, L. Pechini Processes: An Alternate Approach of the Sol–Gel Method, Preparation, Properties, and Applications. In *Handbook of Sol-Gel Science and Technology*; Klein, L., Aparicio, M., Jitianu, A., Eds.; Springer International Publishing: Cham, 2016; pp 1–22. https://doi.org/10.1007/978-3-319-19454-7_123-1.

(148) Gharsallah, H.; Bejar, M.; Dhahri, E.; Hlil, E. K. Critical Behavior in the La 0.6 Ca 0.4−x Sr x MnO 3 Nano-Particle Compounds for x = 0, 0.05 and 0.4. *Journal of Physics and Chemistry of Solids* **2017**, *109*, 50–63. https://doi.org/10.1016/j.jpcs.2017.05.010.

(149) Wenwei, W.; Jinchao, C.; Xuehang, W.; Sen, L.; Kaituo, W.; Lin, T. Nanocrystalline LaMnO3 Preparation and Kinetics of Crystallization Process. *Advanced Powder Technology* **2013**, *24* (1), 154–159. https://doi.org/10.1016/j.apt.2012.04.004.

(150) Pękała, M.; Drozd, V.; Mucha, J. Magnetic Field Dependence of Electrical Resistivity in Fine Grain La0.75Ca0.25MnO3. *Journal of Magnetism and Magnetic Materials* **2005**, *290–291*, 928–932. https://doi.org/10.1016/j.jmmm.2004.11.292.

(151) Lampen, P.; Bingham, N. S.; Phan, M. H.; Kim, H.; Osofsky, M.; Piqué, A.; Phan, T. L.; Yu, S. C.; Srikanth, H. Impact of Reduced Dimensionality on the Magnetic and Magnetocaloric Response of La $_{0.7}$ Ca $_{0.3}$ MnO $_{3}$. *Appl. Phys. Lett.* **2013**, *102* (6), 062414. https://doi.org/10.1063/1.4792239.

Vita

Caitlin Sierra Marie Hunt was bord on November 22, 1996 in Coeur d'Alene, Idaho. She graduated from Idaho Distance Education Academy and with her Associates Degree in General Studies from North Idaho College in 2014. She received her Bachelor of Science in Chemistry from Boise State University, Boise, Idaho in 2017. Caitlin worked as a Laboratory Assistant in the Waites Lab at University of Idaho in 2014 and as an undergraduate researcher in the McDougal Group at Boise State University in 2017. She joined the VCU Chemistry Graduate Program in Spring 2018 where she joined the Carpenter Group and began working as a Graduate Teaching Assistant.